Interaction of angular momentum carrying optical beams with a single nanowire

A thesis

submitted in partial fulfilment of the requirements
for the degree of Doctor of Philosophy

by

Deepak Kumar Sharma
(Reg ID: 20142020)

INDIAN INSTITUTE OF SCIENCE EDUCATION AND RESEARCH,
PUNE

CERTIFICATE

Certified that the work incorporated in the thesis entitled ("Interaction of angular momentum carrying optical beams with a single nanowire") submitted by **Deepak K Sharma** was carried out by the candidate, under my supervision. The work presented here or any part of it has not been included in any other thesis submitted previously for the award of any degree or diploma from any other University or institution.

Date: 4^{th} Nov 2019

(G V Pavan Kumar)
Supervisor

Declaration

I declare that this written submission represents my research work in my own words and where others' ideas or works have been included, I have adequately cited and referenced the original sources. I also declare that I have adhered to all principles of academic honesty and integrity and have not misrepresented or fabricated or falsified any idea/data/fact/source in my submission. I understand that violation of the above will be cause for disciplinary action by the Institute and can also evoke penal action from the sources which have thus not been properly cited or from whom proper permission has not been taken when needed.

Date: 4^{th} Nov 2019

(Deepak Kumar Sharma)
Reg. No: 20142020

Abstract

Angular momentum (AM) is an inherent property of electromagnetic fields. A light beam can possess both spin angular momentum (SAM) and orbital angular momentum (OAM). SAM and OAM are results of transverse spin and orbital energy/momentum flows of the light beam respectively. Transverse spin momentum flow originates from the rotating electric field vector of a circularly polarized light beam. SAM can have two orthogonal states corresponding to left and right-handedness of circular polarization. On the other hand, transverse orbital momentum flow is a result of the azimuthal phase gradient present in optical vortex beams. Systematic control of the spatial phase of a vortex beam can result in an infinite number of orthogonal states of OAM. AM carrying beams can be easily generated in the laboratory by engineering polarization and spatial phase of the Gaussian output of a LASER source. One of the commonly used and easy to prepare OAM carrying beams is Laguerre-Gaussian (LG) beam. AM of the light beam has been utilized as an extra degree of freedom to enhance optical information transfer. Interaction of AM carrying light beams with matter not only provides a fundamental understanding of light-matter interaction but has been harnessed in applications such as quantum memory gadgets, optical trapping, directional coupling and more. The effects of optical AM interaction with matter are small at large scale and can be neglected. But it is important to consider them at scales comparable to the wavelength of the light beam and has been utilized in nanophotonics based applications.

Herein, we have studied the interaction of AM carrying beams with a single plasmonic nanowire (NW). Our study aims at how transverse spin and orbital momentum flows control the scattering of AM carrying beams from an individual NW and generation of plasmons in the NW. We show the optical Spin-Hall effect in the scattering of a light beam from NW caused by spin flow, the detection of OAM states using a single NW at the subwavelength scale and OAM controlled surface plasmon polaritons generation in a plasmonic NW. In order to experimentally probe the above concepts, we have utilized a home-built dual-channel Fourier plane microscopy setup and corroborated the measurement with finite element based numerical simulations. Structured light beams such as Hermite-Gaussian and Laguerr-Gaussian beams are generated using spatial light modulator working in off-axis hologram configuration for experimental observations. Using the developed experimental methods, we have also explored

nonlinear optical effects such as second-harmonic generation and two-photon excited fluorescence from organic mesowire using conventional optical Gaussian beams.

List of Publications

Included in thesis:

- **Deepak K. Sharma**, Vijay Kumar, Adarsh B. Vasista, Shailendra K. Chaubey, G V Pavan Kumar, Spin-Hall effect in the scattering of structured light from plasmonic nanowire, *Opt. Lett.*, 43, 2474-2477 (2018)

- **Deepak K. Sharma**, Vijay Kumar, Adarsh B. Vasista, Diptabrata Paul, Shailendra K. Chaubey, G V Pavan Kumar, Optical orbital angular momentum readout using a self-assembled plasmonic nanowire, *ACS Photonics*, 6(1), 148-153 (2019).

- **Deepak K. Sharma**, Diptabrata Paul, Alexandre Bouhelier, G V Pavan Kumar, Transverse orbital momentum flow controlled surface plasmon polaritons generation in a plasmonic nanowire, *manuscript under preparation* (2019).

- **Deepak K. Sharma**, Shailendra K. Chaubey, Adarsh B. Vasista, Jesil Jose, Ravi P N Tripathi, Alexandre Bouhelier, G V Pavan Kumar, Directional second harmonic generation controlled by sub-wavelength facets of an organic mesowire, *Appl. Opt.*, 57, 5914-5922 (2018).

Not included in thesis:

- Adrian Agreda*, **Deepak K. Sharma***, Sviatlana Viarbitskaya, Romain Hernandez, Benoît Cluzel, Olivier Demichel, Jean-Claude Weeber, Gérard Colas des Francs, G V Pavan Kumar, Alexandre Bouhelier, Spatial Distribution of the Nonlinear Photoluminescence in Au Nanowires, *ACS Photonics*, 6(5), 1240-1247 (2019). (***Contributed equally to this work)***

- Adarsh B.Vasista, **Deepak K.Sharma**, G V Pavan Kumar, Fourier plane optical microscopy and spectroscopy, *Encyclopedia of applied physics*, 1-14 (2018).

- Adarsh B. Vasista, Sunny Tiwari, **Deepak K. Sharma**, G V Pavan Kumar, Vectorial fluorescence emission from metallo-dielectric photonic molecule, *Adv. Opt. Mater.*, 1801025 (2018).

- Adarsh B. Vasista, Harshvardhan Jog, Tal Heilpern, M.E. Sykes, Sunny Tiwari, **Deepak K. Sharma**, Shailendra K. Chaubey, G.P. Wiederrecht, S.K. Gray, G.V.Pavan Kumar, Differential wavevector distribution of surface-enhanced Raman scattering and fluorescence in a film-coupled plasmonic nanowire cavity, *Nano Lett.*, 18, 650-655 (2018).

- Shaili Sett, Ankita Ghatak, **Deepak Sharma**, G V Pavan Kumar, A. K. Raychaudhuri, Broad Band Single Germanium Nanowire Photodetectors with Surface Oxide-Controlled High Optical Gain, *J. Phys. Chem. C*, 122(15), 8564-8572, (2018).

- Danveer Singh, **Deepak Kumar Sharma**, Shailendra K. Chaubey, G.V. Pavan Kumar, Angular emission from 1D and 2D meso- and nano-structures: Probed by dual-channel Fourier-plane microscopy, *Opt. Commun.*, 398, 112-121 (2017)

Acknowledgments

It is my great pleasure to acknowledge the efforts of people who constantly supported me throughout my Ph.D. I am very fortunate to have a motivating and healthy company of my colleagues, friends, and family who never let me feel down during the tough times in the last five and a half years. Optics experiments have always fascinated me during my undergraduate studies and that led me to join Pavan's lab. First, I would like to thank my Ph.D. supervisor Prof. G V Pavan Kumar, for providing me an opportunity to work in his lab and guiding me throughout my Ph.D. I always cherish the freedom he has given me to explore different research ideas in the lab. I am very much inspired by his presentation and writing skills. I thank him for being there for nonacademic issues during my stay at IISER Pune.

I want to thank Dr. Adarsh B Vasista. I don't know whether to thank him as a senior I wished to have or as a friend with whom friendship cannot be put in words. He has been a strong support and encouragement for me to do work in the lab. I have always enjoyed the discussion and healthy criticism from him. I thank him for the numerical simulation support for my experiments and teaching me the same. I have many unforgettable moments with him outside the lab including bike rides, chai, going to restaurants to avoid mess food, and many more.

I thank Dr. Vijay Kumar for sharing the knowledge on angular momentum beams. I have learned a lot from him on structured light, whether it being experimental work or conceptual understanding of the topic. His constant support has been very helpful for me during my Ph.D.

I want to thank my collaborators Prof. Alexandre Bouhelier and Mr. Adrian Agreda. It was a joyful and learning experience working with them. Especially, I credit my understanding of nonlinear photoluminescence and fabrication techniques to them. I thank them for the amazing hospitality they provided during my visits to UoB, Dijon, France.

I want to thank my friends Shalini Pandey, Mayur Shende, Yashaswi Singh, Deepak Chaudhary, Kumar Saurabh, and Nandini Bhardwaj. These are the people who are my backbone and they stood strongly beside me to enjoy my success, bear my pain during the tough times, and to encourage me to achieve my goals. I am very lucky to have all of them in the form of different characters.

I thank my lab-mates Diptabrata Paul, Chetna Taneja, Shailendra Chaubey, Vandana Sharma, and Sunny Tiwari for providing a wonderful and friendly environment in and outside the lab. I thank Diptabrata for supporting me in experiments. I have enjoyed working with him especially, discussions with him are always learning experiences. I thank Chetna for supporting me in optical experiments and Shailendra for providing me with samples for nonlinear optics measurements. I thank Sunny and Vandana for quick and important feedback on my research work. I want to thank my past lab members Dr. Preeti Gupta, Jesil Jose, Dr. Danveer Singh, Aswathy V.G., Dr. Arindam Das Gupta, Dr. Partha Pratim Patra, Dr. Ravi Tripathi, Rajat Sawant, Harshvardhan Jog, Dr. Rohit Chikkaraddy, and Dr. Debrina Jana. I am lucky to work with these amazing people and had a great time with them. I thank Jesil for supporting me in experiments and Dr. Danveer Singh for teaching me the instrumentation in the initial phase of my Ph.D. A healthy criticism and discussion culture in the lab has helped me in improving the quality of my research work and my understanding. I enjoyed our gossips on Chai in MDP. I thank MDP people for providing us an amazing service.

Basket-ball court has been the place for me to release the work stress and get freshen-up again. I thank my friends from athletics group (Sharada, Rashmi, Prashant, Ravi, Manish, Sudhir) and Basket-ball team (Kunjan, Salam, Anant, Anupam, Santhosh, Yamini, Digvijay, Yuvraj, Peddiraju, Paras, Abhishek, Shaunak) for the company they have provided. I will never forget late night gossips, birthday celebrations, and of course long runs and basketball games.

I thank my batch-mates Nilam, Kriti, Shubham, Mohit, Dipti, Soham, Shikha, Tejal, Sayali, Yashwant, Ankita, Deepak, Vikhyat. Puneeta, Prashant, Rajesh. My journey with them has been joyful and entertaining.

I extend my heartfelt thanks to my research assessment committee members Prof. T S Mahesh and Prof. Rejish Nath, for the critical assessment and important feedback during the meetings. It helped me improve my skills and research work quality.

I want to thank IISER Pune for providing me with a friendly environment and all the needed facilities. I thank Mr. Prabhakar, Ms. Dhanashree, Mr. Tushar, and Mr. Prabhas, for helping me with document work.

In the end, I thank my whole family for their endless love and support. Especially my parents, who work hard in the fields day and night to bear our expenses. They are the real heroes for me and have been the source of my enthusiasm and courage.

Dedicated to my parents

Contents

Chapter 1

Introduction : Angular momentum of light and its interaction with matter

A light beam is defined by its intensity profile, phase distribution and polarization degree of freedom it carries. It is well understood that a light beam carries energy as well as linear momentum. With respect to a coordinate origin, the light beam traveling at distance'R' with linear momentum $\vec{P}$ also possesses orbital angular momentum (OAM) given by, $\vec{L}_{ext} = \vec{R} \times \vec{P}$.

$\vec{L}_{ext}$ is extrinsic OAM and is transverse to the direction of propagation. But with engineering of polarization and spatial phase of the beam, one can provide angular momentum (AM) to the light beam which is intrinsic to it and aligned along the direction of propagation. Angular momenta of an optical beam associated with polarization and spatial phase profile are spin angular momentum (SAM) and intrinsic OAM. Rotating electric field vector in circularly polarized light beam results in SAM. SAM can have two orthogonal states with $\pm\hbar$ AM per photon corresponding to right and left hand circular polarization respectively. On the other hand, vortex beams which have helical phase front possess intrinsic OAM. Most common example of vortex beams is Laguerre-Gaussian (LG) beams. LG beams have azimuthally varying phase term, i.e., *exp(-ilϕ)* which results in OAM in the direction of beam propagation. Here, ϕ is azimuthal coordinate and *l* is an integer value, known as topological charge or OAM mode number which defines a particular state of OAM beam. OAM can have infinite number of orthogonal states depending on spatial phase structure with magnitude equals to $\pm l\hbar$ per photon for topological charge *l*. Figure 1.1 [1] shows schematics representing three different types of AM in paraxial light beams. The figure indicates extrinsic OAM is transverse to the direction of propagation of beam while intrinsic AMs are in the direction of propagation. During the course of this thesis, I will be discussing SAM and intrinsic OAM only, and for convenience, intrinsic OAM is mentioned as OAM. In what follows, I will briefly discuss about history and origin of intrinsic AMs and their interaction with matter within the scope of this thesis.

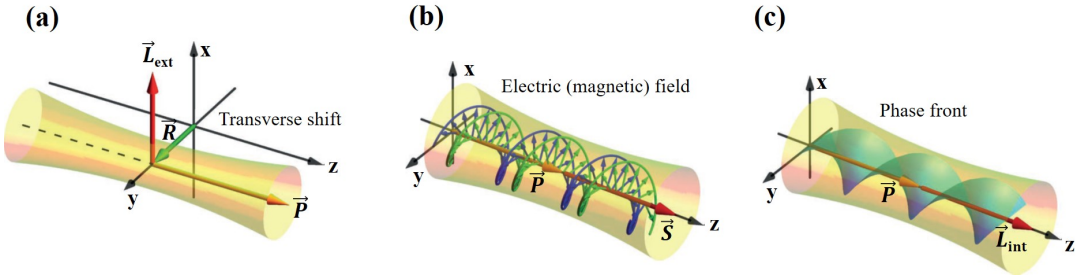

FIGURE 1.1: Schematic showing angular momentum of paraxial beams: (a) extrinsic orbital angular momentum, (b) spin angular momentum and (c) intrinsic orbital angular momentum. Reprinted by permission from Springer Nature: Nature Photonics [1], Copyright (2015).

1.1 A brief history of angular momentum

History of study of angular momentum of light dates back to 1909 when J. H. Poynting [2] proposed a uniformly revolving shaft as a mechanical model for circularly polarized light. He suggested that change in polarization from circular to linear or vice versa by an optical element (quarter wave plate) should exert a torque on the optical component. He believed this exerted torque by the light beam on the optical element is too small to be observed practically. But in 1936 [3], Beth experimentally observed SAM of light. He used a quartz wave plate hanging on a filament and observed experimentally a torque exerted by the light beam on the plate as it changes its polarization upon passing through the plate.

On the other hand, Allen in 1992 [4] showed that LG beams which carry helical phase front, i.e., $exp(-il\phi)$ possess orbital angular momentum equal to $\pm l\hbar$ per photon. As OAM is a result of azimuthally varying spatial phase, he used astigmatic optical components to observe it mechanically. He experimentally demonstrated that a torque is exerted on a fiber with which two cylindrical lenses were suspended as LG beam passes through lenses. The mechanical torque on fiber was a result of the change in sign of OAM by optical components. At the moment, AM carrying beams are not only used for fundamental understanding but have wide range of application also. I suggest [5–10] for further reading on advances in the field of AM of light.

1.2 Origin of intrinsic angular momentum of light: Transverse energy flows

From AM relation, it is clear that linear momentum in direction of propagation can not generate intrinsic AM as both are in the same direction. Generation of intrinsic AM

is possible only if there is a component of Poynting vector (linear momentum) of the beam in the transverse plane aligned along azimuthal coordinate. Hence, ideal plane wave which has total linear momentum (Poyting vector) in the direction of beam propagation, cannot possess intrinsic AM. But in reality, the finite extent of light beam or limited dimension of the detecting system, inhomogeneous distribution of intensity and spatially varying phase with respect to transverse coordinates can result in a Poynting vector component tranverse to propagation direction of the beam. These components of Poynting vector are called transverse momentum (or energy) flows [11]. Henceforth, I will use energy flow and momentum flow interchangeably. In this section, I will briefly discuss about the origin of transverse energy flows for paraxial beams and their experimental visualization.

Total energy flow density can be represented by time averaged Poynting vector ($\vec{S}$),

$$\vec{S} \propto Re[\vec{E} \times \vec{H}^*] \tag{1.1}$$

Where $\vec{E}$ and $\vec{H}$ are time averaged electric and magnetic field vectors.

In 2006 [12], Bekshaev and Soskin showed that for paraxial beams, total energy flow can be decomposed in spin and orbital energy flows. Where spin energy flow is transverse in nature but orbital energy flow has both transverse and longitudinal components. Transverse spin and orbital energy flows result in spin and orbital AM to a beam respectively in the direction of propagation. Later in 2009 [13], Berry gave a generalized description for energy flows in case of nonparaxial field.

1.2.1 Spin energy flow

Spin energy flow density ($\vec{S_c}$) part of equation 1.1 for paraxial beam propagating in z direction can be written as [12]

$$\vec{S_c} \propto -\vec{e_z} \times \vec{\bigtriangledown}_\perp S_3 \propto curl(e_z S_3) \tag{1.2}$$

where, $\vec{e_z}$ is a unit vector in the direction of beam propagation, $\bigtriangledown_\perp$ is transverse gradient and S_3 is forth Stokes parameter which gives the difference of intensity between right and left hand circular polarizations, i.e., $S_3 = I_{RCP} - I_{LCP}$.

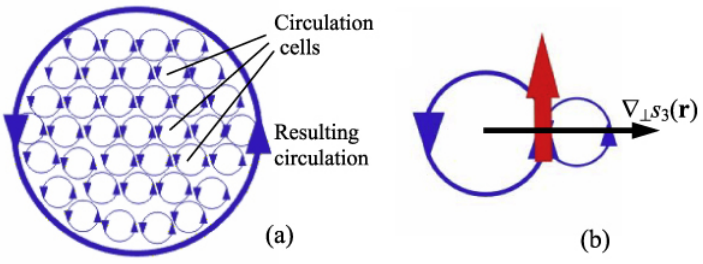

FIGURE 1.2: Origin of spin flow: (a) Due to finite boundary of a beam, (b) Inhomogeneous distribution of intensity in a circularly polarized beam. From ref [11]. Reproduced by permission of IOP Publishing.

We can draw following inferences from equation 1.2. First, spin energy flow density has solenoidal behaviour and hence spin flow lines are continuous everywhere. Second, it is clear that spin flow density depends on S_3 and will be nonzero only for circularly/elliptically polarized light beams. In particular, it is dependent on gradient of S_3 and is perpendicular to both direction of propagation and gradient of S_3. There are two possibilities for the generation of spin flow in circularly polarized beam as shown in figure 1.2 [11]. One of them is the finite extension in the transverse direction (figure 1.2(a)) (This contribution is not included in equation 1.2). If the circularly polarized beam has a homogeneous distribution of the intensity, gradient of S_3 is zero but abrupt boundary of the beam results in macroscopic spin flow. Secondly, if the beam has inhomogeneous intensity distribution and hence nonzero gradient of S_3, it possesses spin energy flow perpendicular to gradient of S_3 as shown in figure 1.2 (b). For beam having inhomogeneous intensity in radial direction, spin flow will be along azimuthal coordinate which will give rise to SAM in the direction of beam propagation. Figure 1.3 shows numerically calculated spin energy flows using equation 1 for Gaussian and Hermite Gaussian beams.

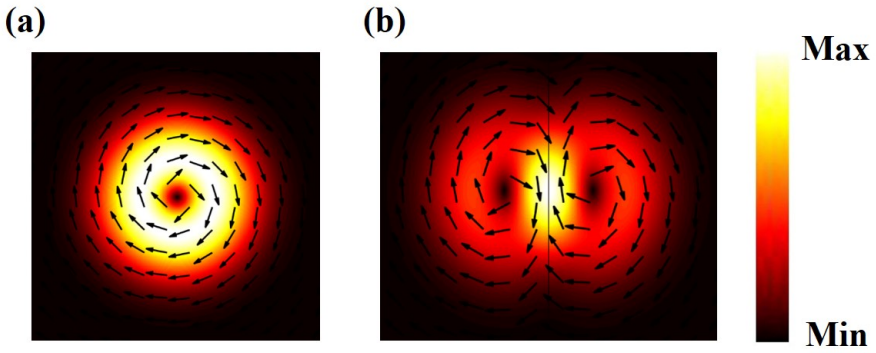

FIGURE 1.3: Spin energy flow density: Left hand circularly polarized (a) Gaussian beam and (b) Hermite Gaussian beam. Arrows show the local spin flow directions and the background is its magnitude.

Experimental measurement of macroscopic spin energy flow:

When a light beam hits an object, it transfers momentum associated with the beam to the object. Although this momentum is very small and can be neglected for large objects but it is enough to move nanometer or micrometer size particles. O. V. Angelsky et al., [14] used a non-spherical dielectric particle suspended in a water-filled cell for the experimental demonstration of spin energy flow. They showed when the particle interacts with weakly focused circularly polarized Gaussian beam, it performs rotational motion about the center of the beam with spinning along its own axis as shown in figure 1.4. Rotational motion of the particle can be attributed to spin energy flow as there are negligible possibilities for the conversion of SAM to OAM in weak focusing condition.

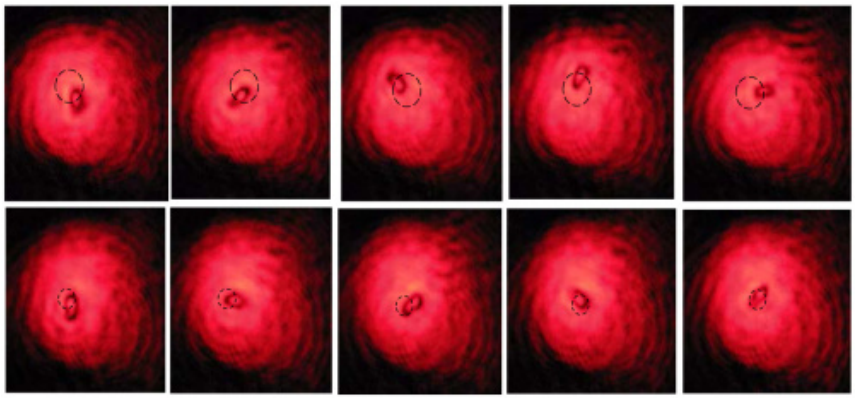

FIGURE 1.4: Orbital motion of non-spherical dielectric particle particle in weakly focused Gaussian beam with left (upper row) and right (lower row) hand circular polarizations. Figure has been adapted from [14] with permission © The Optical Society.

1.2.2 Orbital energy flow

In contrast to transverse nature of spin energy flow, orbital energy flow has both longitudinal and transverse components. Longitudinal component represents the intensity profile of the beam. On the other hand, transverse orbital energy flow results in OAM. For a paraxial beam, orbital flow depends on spatial phase distribution and has following relation [12]

$$\vec{S_O} \propto \vec{\nabla}_{\perp}\Phi \tag{1.3}$$

Where, Φ is spatial phase distribution.

Equation 1.3 depicts that the transverse orbital flow is determined by gradient of spatial phase distribution and will be zero for a beam with constant phase front. Hence ordinary laser beams which have constant phase will not result in transverse orbital energy flow. But Laguerre Gaussian (LG) beams have azimuthally varying spatial phase distribution which results in transverse orbital energy flow and hence OAM. LG beams

are widely used as a OAM carrying beams. In following, I describe energy/momentum flows of these beams.

LG beam can be represented by following complex scalar function [4]

$$u_{pl}(r,\phi,z) = \frac{C}{(1+\frac{z^2}{z_R{}^2})^{\frac{1}{2}}}\left(\frac{r\sqrt{2}}{w(z)}\right)^l L_p^l\left(\frac{2r^2}{w^2(z)}\right) exp\left(\frac{-r^2}{w^2(z)}\right) \\ \times exp\left(\frac{-ikr^2z}{2(z^2+z_R^2)}\right) exp(-il\phi) exp\left(i(2p+l+1)tan^{-1}\frac{z}{z_R}\right) \tag{1.4}$$

where z_R is the Rayleigh range, $w(z)$ is the radius of the beam and the beam waist is at z = 0 for beam propagating in z direction. r and ϕ are transverse coordinates. L_p^l is the associated Laguerre polynomial and C is a constant.

Using equation 1.1 and 1.4, we get linear momentum density components in r, ϕ and z directions [15] as follows,

$$P_r = \epsilon_0 \frac{\omega k r z}{(z_R^2+z^2)}|u|^2, \\ P_\phi = \epsilon_0\left[\frac{\omega l}{r}|u|^2\right], \\ P_z = \epsilon_0 \omega k |u|^2 \tag{1.5}$$

where ϵ_0 is permittity of free space, ω is angular frequency and k = ω/c is wave number.

Different components of linear momentum contribute to different physical properties of the beam. P_r is the reason for the divergence of propagating beam. P_z is linear momentum in the direction of propagation of the beam. P_ϕ, azimuthal component of linear momentum represents transverse orbital energy flow and results in orbital angular momentum in the direction of propagation (z) with orbital angular momentum density equal to

$$\vec{L}_{int} = \epsilon_0 \omega l |u|^2 \vec{e}_z \tag{1.6}$$

This shows that OAM is directly proportional to topological charge l and can have infinite number of states depending on different value of number l. Figure 1.5 shows transverse orbital energy flow for LG beam with topological charge l = -1. In chapter 2, I will describe generation methods for different modes of LG beams.

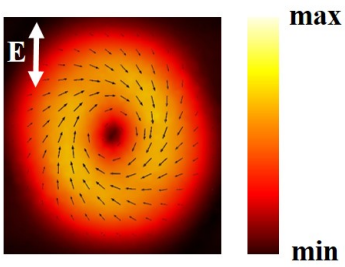

FIGURE 1.5: Orbital energy flow density: Arrows show the local transverse orbital flow directions and the background is its magnitude for l = -1.

Experimental measurement of transverse orbital energy flow:

Transverse orbital energy flow depends on spatial phase distribution in azimuthal direction and can have different magnitude depending on different phase structures, i.e., different l value in the context of LG beams. Figure 1.6 shows two experiments about the observation of transverse orbital energy flow. Figure 1.6 (a) [16] shows rotation of a silver nanowire (NW) when it interacts with LG beams. Rotation of the NW is a result of torque produced by transverse energy flow in the beam. Increment in magnitude of orbital flow with l value can be observed in increase of angular velocity of the NW rotation. Transverse orbital energy flow can also be visualized by diffracting the beam from a single slit as shown in figure 1.6 b [17].

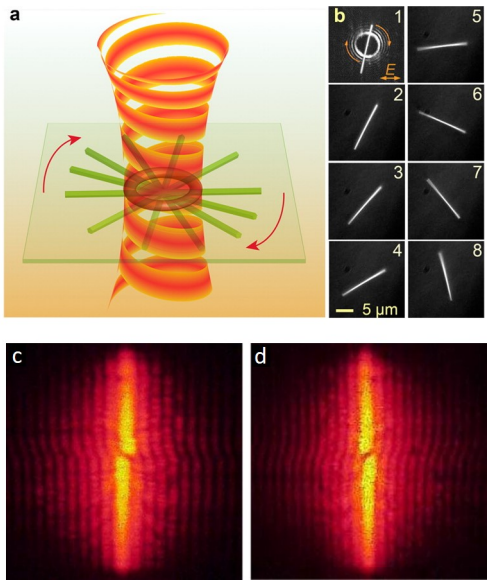

FIGURE 1.6: (a and b) Transverse orbital energy flow induced rotation of silver nanowire using LG beams. (c and d) Diffraction pattern of LG beams with topological charge -1 and +1 from single slit showing transverse orbital energy flow. Figures have been adapted (a-b) with permission from [16] © (2013) American Chemical Society and (c-d) from [17] © (2009), with permission from Elsevier.

1.3 Interaction of AM carrying beams with matter (in the scope of this thesis)

Interaction of AM of light with matter not only provides a fundamental understanding of spin-orbit and orbit-orbit coupling of light but also finds applications in optical information transfer, memory gadgets, optical tweezers, etc. Although the effects due to AM are very small in magnitude and can be neglected at large but have to be taken into account at wavelength scale. In our work, we have studied the interaction of AM carrying beams with single plasmonic nanowire (NW). Specifically, we have focused on following questions:

1. Spin-Hall effect of light
2. Detection of OAM states at subwavelength scale
3. OAM controlled generation of surface plasmon polaritons

In this section, I will discuss about different concepts used and recent advances on above topics and will outline the work of the thesis.

1.3.1 Spin-Hall effect of light

In view of condensed matter physics, Spin-Hall effect describes the deviation of up and down spin electrons in opposite directions in the transverse plane to electric current flow in a conductor [18]. Analogous to it, the spin-Hall effect of light represents SAM induced transverse shift of optical beam [19]. The optical Spin-Hall effect essentially originates from the interaction of SAM and extrinsic OAM. Spin-Hall effect has been realized in gradient-index medium [20], upon refraction or refraction at the interface of two transparent media [21–23], refraction through tilted polarizer [24], surface plasmon polaritons in metal film [25], anisotropic plasmonic chain [26] and metasurfaces [27, 28] and many more. I would suggest reviews [1, 29] for the basic understanding of the spin-Hall effect and recent advances in the field. Spin-Hall of light finds applications in metrology [30], spin-dependent plasmonic lenses [31], position sensing [32], etc.

One of the examples of Spin-Hall effect is spin-dependent transverse shift of optical beam upon reflection or refraction from an interface. Figure 1.7 shows the splitting of the linearly polarized light beam into spatially separated right and left handedly circularly polarized beams upon refraction from air-glass interface [21]. This splitting (optical spin-Hall effect) is a result of the geometrical phase [33] resulted from transversality condition between the electric field and wavevector of a plane wave. A practical optical beam consists of plane waves with slightly different wavevectors as it has some

divergence from propagation axis. Because of the transversality condition, polarization vector of plane waves with slightly different wavevectors in the beam rotates differently upon refraction, which results in a global geometrical phase.

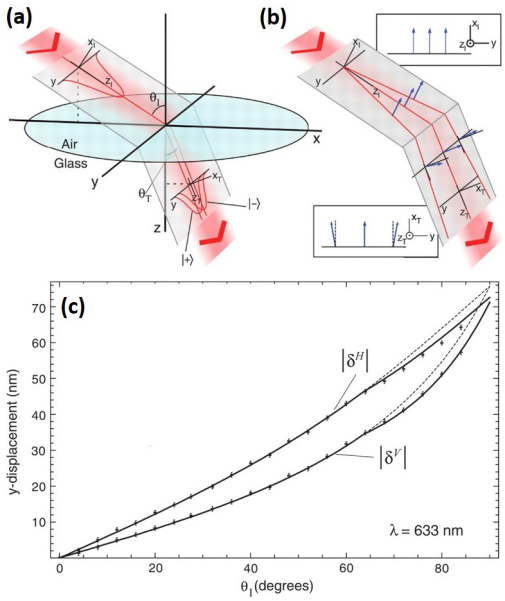

FIGURE 1.7: (a) Schematic showing spin-Hall effect of light upon refraction. (b) Different rotation for plane waves with different wavevectors. (c) Quantum weak measurements showing separation between two spin components upon refraction for incident vertical and horizontal polarization as a function of incident angle with respect to normal. "From [21]. Reprinted with permission from AAAS."

1.3.2 Detection of OAM states

As discussed above, OAM is a result of azimuthally varying phase in vortex beams which can have any value in multiples of 2π and results in an infinite number of OAM orthogonal states. These states of OAM can be achieved routinely in the laboratory using a phase mask on Gaussian beam, a typical output of the LASER (to be discussed in chapter 2). But the utility of these beams, especially in optical information transfer comes with the challenge of detection of different OAM states which carry unique information at the receiver end. The fact that beams with different topological charge comprise unique phase information, interference-based detection is widely used to detect different OAM states. In interference-based detection methods, a reference beam interferes with OAM carrying beam and results in unique patterns for different OAM states. Figure 1.9 (a) shows detection of OAM states based on interference pattern recognition at the macro scale [34]. The method can be utilized at the chip-scale also as shown in figure 1.9 (b) [35]. Here interference patterns are a result of interaction

between spherical wave generated by localized plasmon at nanohole and transmitted OAM carrying beams. Several other proposed methods based on plasmonic gratings are shown in [36–38].

These methods are either limited by the intensity of the reference beam or by complicated nanostructuring. We propose and experimentally show that elastic scattering from a single NW can be utilized for the detection of OAM modes at subwavelength scale. In this way, we get rid of reference beam and use simple nanostructure which can be integrated in plasmonic circuits.

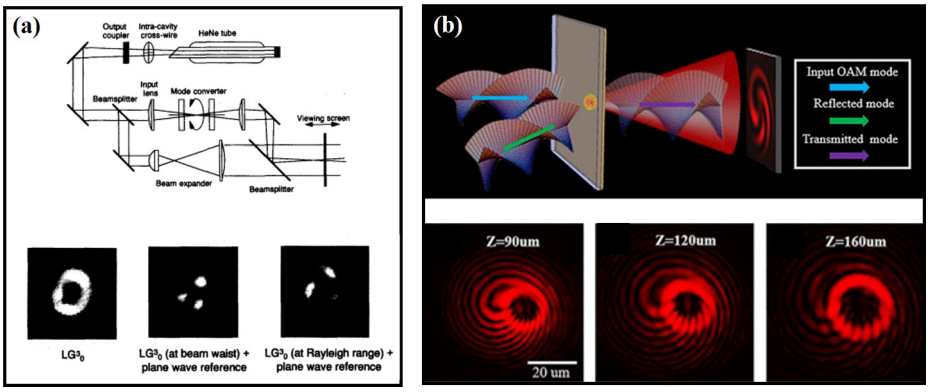

FIGURE 1.8: Interference based detection of OAM states of an LG beam. (a) Free space detection of the topological charge of the LG beam by interfering it with reference plane wave. Interference patterns are shown for $l = +3$ taken at different distances along the propagation direction. (b) Detection of topological charge at small scale by detecting interference pattern generated by interference between transmitted LG beam through thin plasmonic film and spherical wave generated by localized plasmon at nanohole. Interference patterns are shown for $l = +8$ recorded at different distances along the propagation direction. Figure (a) has been reproduced from [34], with the permission of the American Association of Physics Teachers. Figure (b) has been adapted with permission from [35]. © (2017) American Chemical Society

1.3.3 Surface plasmon polaritons (SPPs)

We have studied how OAM affects the coupling of light to plasmonic nanowire waveguide. In a nanowire, light is guided through surface plasmon polaritons (SPPs). SPPs are surface electromagnetic waves at the metal-dielectric interface [39], as shown in figure 1.10 (a). SPPs are confined to the interface and decay exponentially in both mediums (inset, figure 1.10 (a)). Large (in comparison to dielectric) and negative permittivity of metals makes the confinement of SPPs possible at the interface [39, 40].

Solving Maxwell equations with an appropriate boundary condition at metal-dielectric interface results in following dispersion relation for SPPs [40]:

$$k_{SPP} = k_0 \sqrt{\frac{\epsilon_m \epsilon_d}{\epsilon_m + \epsilon_d}} \tag{1.7}$$

Where ϵ_m and ϵ_d are permittivity of metal and dielectric mediums. $k_0 = \omega/c$ is wavevector of free space photon. Dispersion relation shows that for constant frequency, the momentum of SPP is larger than of free space photon, as shown in figure 1.10 (b). This mismatch of the momentum restricts the generation of SPPs to few methods such as prism and grating coupled excitation [41]. Topological defects at the surface can also provide extra momentum to photon for the generation of SPPs. In the case of NW waveguide (shown in figure 1.10 (c)), excitation of one of the extremity with light beam provides extra momentum for SPPs generation. Efficiency of the SPPs generation in the NW depends on many parameters of lights as well as NW. Some of them are numerical aperture of focusing lens, polarization and wavelength of excitation light, diameter and material of NW.

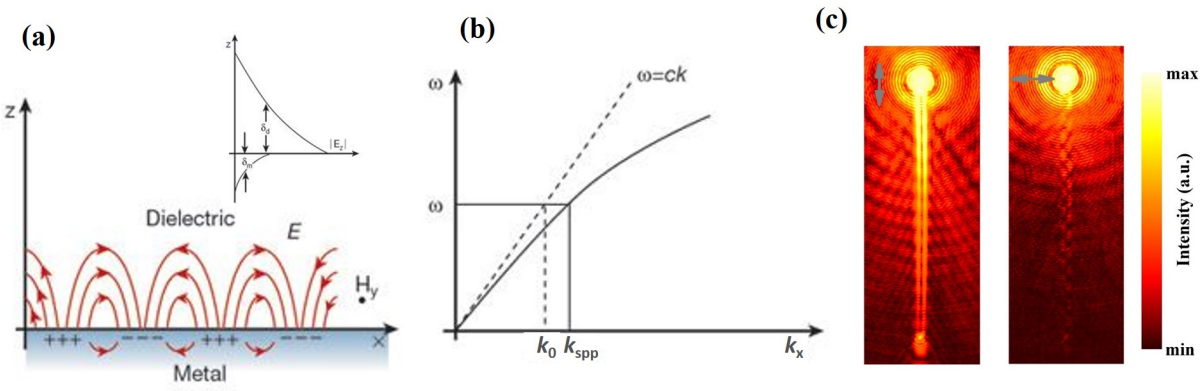

FIGURE 1.9: (a) Schematic showing SPPs on metal-dielectric interface. Inset shows exponential decay of SPPs in both mediums. (b) Dispersion diagram for SPPs. (c) Input polarization controlled excitation of SPPs in silver NW at 633 nm wavelength using a high numerical aperture focusing lens (1.49 NA, 100x). Figures (a) and (b) have been reprinted by permission from Springer Nature: Nature[39], Copyright (2003).

1.3.4 Outline of the thesis

The thesis focuses on how transverse energy/momentum flow of intrinsic AM carrying beams affects the scattering and plasmon generation in NW. Thesis is divided into six chapters. Following is the chapter wise breakup of the work included in the thesis:

Chapter 2 (Optical measurement techniques: Dual channel Fourier plane microscopy and spectroscopy setup)

We have utilized home built channel Fourier plane microscopy and spectroscopy setup to understand light-matter interaction at small scales. The chapter focuses on the following points:

- Generation of higher-order Gaussian beam (Hermite Gaussian and Laguerre Gaussian beams)
- Concept of Fourier plane imaging and its implementation in the microscopy system
- The architecture of the microscope
- Forward and backward light scattering configurations of microscope for the understanding of linear and nonlinear scattering of light

Chapter 3 (Spin momentum flow controlled far-field scattering of structured light from a plasmonic nanowire: Optical Spin-Hall effect)

The chapter discusses the effect of transverse spin energy/momentum flow on the elastic scattering of Hermite Gaussian (HG) and Gaussian beams from a silver nanowire. Experiments are done in forwards scattering configuration where low numerical aperture lens excites the NW and high numerical aperture lens captures the transmitted and scattered light in the forward direction. We image the back focal plane of the collection objective lens to get Fourier plane images and study scattered far-field patterns as a function of input polarization. We observe handedness dependent asymmetric scattering patterns in farfield for circular polarization. Experimental observations are corroborated using finite element method (FEM) based simulations.

Chapter 4 (Discrimination of orbital angular momentum states of vortex beam using silver nanowire)

In this chapter, we present far-field elastic scattering from silver nanowire as readout mechanism of magnitude and sign of topological charge of Laguerre Gaussian (LG) beams. We use the same forward scattering configuration as used in chapter 3 and capture scattered far-field using Fourier plane imaging technique. We compare scattering pattern of LG beams with HG and Gaussian beams. OAM present in LG beams results asymmetry in the scattered far-field induced by transverse orbital energy/momentum flow. Different states of OAM form unique patterns in far-field and provides information about magnitude and sign of topological charge. We mimic the experimental configuration in FEM based simulations and qualitatively corroborate the experimental measurements.

Chapter 5 (Transverse orbital momentum flow controlled surface plasmon polaritons generation in a plasmonic nanowire)

In this chapter, we discuss the effect of OAM on SPP coupling in silver nanowire. LG beam is focused using high numerical aperture lens at the extremity of the NW to generate SPP. Now NW is scanned across the beam's focus and SPP coupling is observed for different position of NW wire on beam where transverse orbital momentum flow favours or does not favour the SPP coupling in the NW. We propose and experimentally show that azimuthal component of momentum induced by the helical phase of the LG beam should be taken into account for momentum matching condition for SPPs coupling. Our experimental results are qualitatively supported with finite elelment based simulations. We also show that OAM controlled SPP generation in two arms of kink NW and NW-NP (nanoparticle) systems can behave as an optical switch.

Chapter 6 (Conclusion and future directions)

Chapter concludes the thesis and gives futures directions related to the interaction of AM carrying beams beams with NW.

Appendix (Directional second-harmonic generation controlled by sub-wavelength facets of an organic mesowire)

In this work, we have utilized selective excitation of facets of triangular cross-section mesowire to control second harmonic generation signal wavevectors. Experiments are done in forwards scattering configurations. We have achieved a change of 140 degrees angle in the direction of SHG signal as a function of excitation spot position across mesowire. We have done Finite-difference time-domain at the fundamental wavelength to understand the experimental results.

Chapter 2

Optical measurement techniques: Dual channel Fourier plane microscopy and spectroscopy setup

Light-matter interaction has not only enriched the in-depth fundamental understanding of electromagnetic-magnetic fields and matter but has also advanced today's technology with many innovative applications. The effects of light-matter interaction are much pronounced at scales where object geometry becomes comparable to the wavelength of light. Optical microscopes serve the purpose to observe the effects of light-matter interactions at these scales. To boost the light-matter interaction at the micron or smaller scales, we need to modify the parameters of light and improve the microscopy techniques. In this chapter, we focus on both of these aspects. I discuss techniques to generate complex beams that can possess angular momentum and can have complex intensity distribution. On the detection aspect of light-matter interaction, I discuss Fourier plane imaging technique, which provides resolution in momentum (wavevector) space. We have built a two-channel microscopy system which involves complex beam generation, Fourier plane imaging techniques along with capabilities of doing nonlinear microscopy and spectroscopy, and energy-momentum spectroscopy. The chapter is divided into following sections:

- Generation of higher-order Gaussian beams (Hermite Gaussian and Laguerre Gaussian beams)
- Concept of Fourier plane imaging and its implementation in the microscopy system
- The architecture of the microscope
- Forward and backward light scattering configurations of microscope for the understanding of linear and nonlinear scattering of light

2.1 Generation of higher-order Gaussian modes

Profile of a Laguerre Gaussian beam (LG_p^l) is determined by its azimuthal (l,topological charge) and radial (p) indices. Topological charge (l) determines the orbital angular momentum (OAM) and radial index (p) determines the intensity profile of the beam. In our experiments, we have focused only on the effect of the OAM and hence have put radial index to be zero. In this section, I will introduce different possible methods for the generation of LG beams and will discuss the method we have utilized.

Laguerre Gaussian (LG) beams are solutions of the paraxial wave equation in cylindrical coordinates. Hence a laser with a circular cylindrical cavity can produce these beams [42, 43]. But LG beams can also be generated using optical elements, which can provide azimuthally varying phase, i.e., $exp(il\phi)$ to the Gaussian output of conventional lasers. This extra spatially varying phase can be provided by two types of optical instruments. One of them is called the spiral phase plate [44]. Spiral phase plates have azimuthally varying thickness with total change being in integer multiple (l) of wavelength (λ) of light, as shown in figure 2.1 [5]. When the light beam passes through the plate, it travels different optical path length along azimuthal coordinate, and hence different parts of the beam acquire different phases in azimuthal direction resulting in an output beam with helical phase front. Integer l is essentially the topological charge and determines the OAM mode of the generated LG beam.

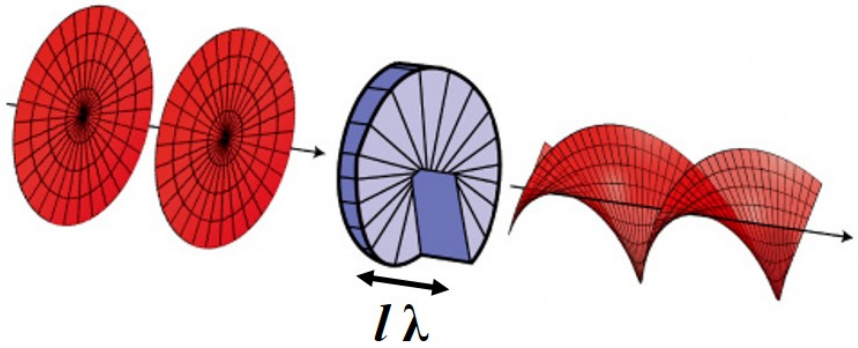

FIGURE 2.1: Schematic representation of generation of LG beams using spiral phase plate. Here λ is wavelength of the incident light beam and l is an integer which represents the topological charge of the generated LG beam. Figure has been reproduced from [5] with permission © The Optical Society.

Another generation method is based on holograms [45–48]. Holograms are recorded interference patterns between a light beam of interest and a reference beam. When the hologram is illuminated with the reference beam, it generates back the beam of interest.

For practical purposes, a plane wave or Gaussian beam can be taken as a reference beam. There can be two types of hologram configurations, i.e., off-axis and on-axis. Interference between a mode of LG beam and reference beam can be recorded on a holographic plate. In the context of interference of LG beam with the reference beam, on-axis and off-axis holograms have the form of spiral Fresnel zone plate [46] and forked diffraction grating [45] respectively as shown in figure 2.2.

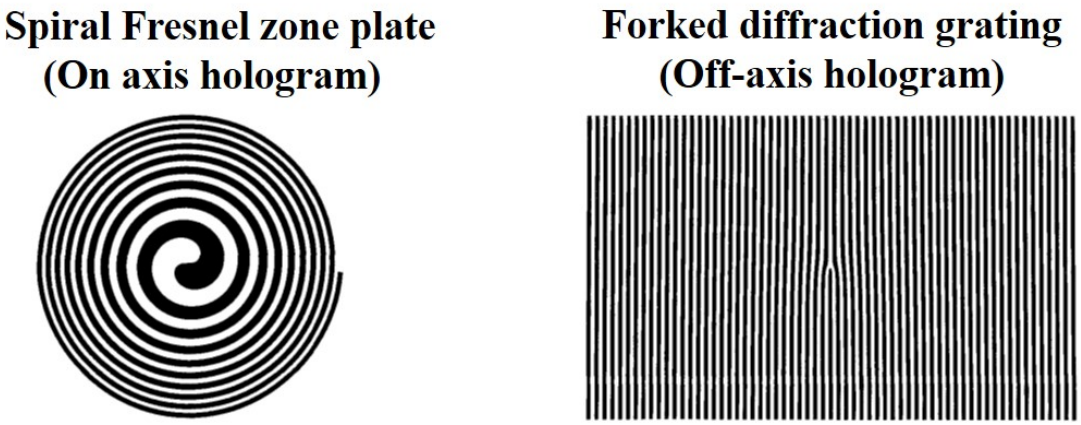

FIGURE 2.2: On-axis (Spiral Fresnel zone plate) and off-axis (Forked diffraction grating) holograms for the generation of LG beam with topological charge $l = 1$. Figures have been adapted with permission from[46] © The Optical Society and from Springer: Optical and Quantum Electronics [45], © (2015).

In our experiments, we have utilized forked diffraction grating to generate LG beams. This configuration has an advantage over on-axis holograms in terms of purity of the mode. Forked diffraction gratings can also be generated numerically. Steps to generate a forked diffraction grating are shown in figure 2.3 [5] where a phase mask having azimuthally varying phase in an integer multiple of 2π (6π for this figure) and linear phase ramp are added to generate the grating.

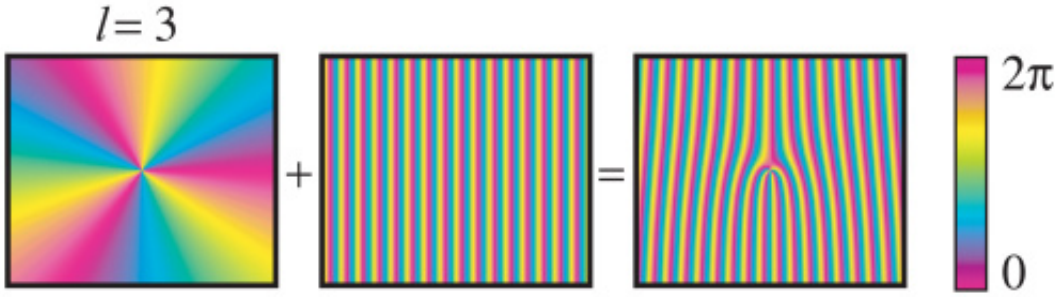

FIGURE 2.3: Schematic representation of fork diffraction grating generation with the addition of azimuthally varying phase mask and a linear phase ramp for the topological charge, $l = 3$. Figure has been adapted from [5] with permission © The Optical Society.

Complex beam generation using spatial light modulator (SLM):

We have utilized SLM in off-axis holography mode for the generation of LG beams. SLM is a computer-controlled optical device that can modulate the phase, amplitude, and polarization of an optical beam. It uses computer-controlled liquid crystal display (LCD) for the modulation of the light beam. Numerically generated diffraction patterns were projected to display of SLM for the generation of LG beams. Figure 2.4 shows schematic of an experimental setup to generate LG beams in the laboratory. SLM display (LCD) is illuminated with a Gaussian beam, an output of conventional HeNe laser (633 nm). 1^{st} diffraction order of the diffracted light beam from fork diffraction grating results in LG beam corresponding to the topological charge used in hologram on the screen. Different modes can be generated by just changing the hologram pattern on the screen. We filter the 1^{st} diffraction order and send it to the microscope. SLMs are not only used to generate LG beams but can be utilized to generate other complex beams. We have utilized the same method to generated Hermite Gaussian (HG) beams also. Figure 1.4 shows the intensity profile of the LG_0^1 and HG_{10} beam generated using this method at the 1^{st} diffraction order.

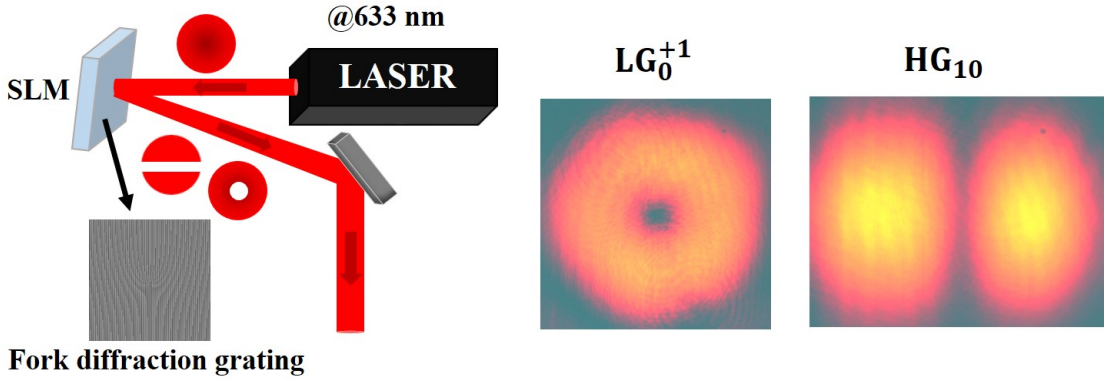

FIGURE 2.4: Schematic for the generation of complex beams using spatial light modulator in off-axis holography mode. Generated patterns for LG_0^1 and HG_{10} beams.

2.2 Concept of Fourier plane imaging and its implementation in the microscopy system

One of the important properties of a light source is the directionality of the light it emits. For example, a tungsten bulb emits in all the directions, but a light beam from a LASER is confined to very small wave vectors and hence the latter is called directional source. It is easy to differentiate light sources based on directionality at the macro scale as the human eye has a three-dimensional view. But differentiation becomes difficult at

the micro or smaller scales where one needs a microscopy system to capture the signal from these sources. It is because a microscope captures a two-dimensional image of the emitter in real space coordinates and hence loses out on wave vector information. Measurement of wave vectors of light from micro-scale emitters is possible using the Fourier plane microscopy technique, which captures information in angular coordinates (wave vector space). Fourier plane microscopy is based on Fourier transform property of a lens [49]. Essentially, if an emitter/scatterer is placed at the front focal plane of a lens, imaging the back focal plane (BFP) of lens gives information about wave vectors of the emitted/scattered light. Fourier plane microscopy is a well-understood technique [49] and was known as conoscopy[50, 51] in the early days. I suggest review[52] for recent applications in Fourier plane imaging.

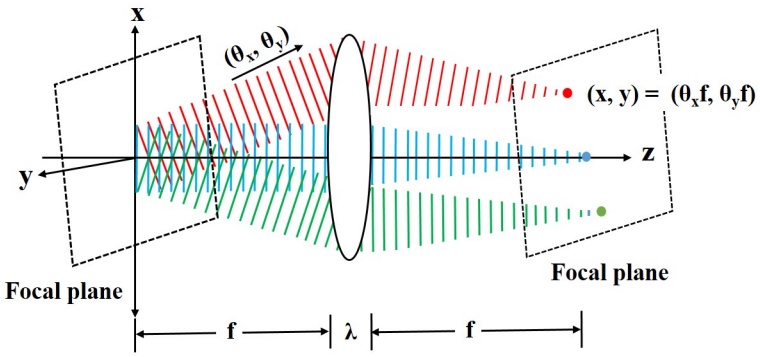

FIGURE 2.5: Schematic for the geometrical explanation of Fourier transform property of a lens. Figure has been reproduced from [49] with permission.

Fourier plane imaging technique is geometrically explained in figure 2.5 [49]. Light emission from an emitter placed at the front focal plane of the lens can be expressed as a weighted sum of the plane waves emanating at different angles (θ_x, θ_y). When these plane waves pass through the lens, they get focused on different points $(\theta_x f, \theta_y \mathrm{f})$ at the back focal plane, here f is the focal length of the lens. The figure shows three plane waves emanating at different angles (represented with three different colors) get focused at three different points. Hence in this way, each point in the back focal plane of the lens represents a particular direction of emission.

Implementation of Fourier plane imaging technique in microscopy system: It is clear from figure 2.5 that one has to record BFP of the imaging lens to perform Fourier plane imaging. But BFP of a microscopic objective lens is formed close to its back aperture and is difficult to be captured on an imaging camera experimentally. An alternate method to capture BFP is using relay lenses as shown in figure 2.6. Schematic

shows placement of tube lens and Bertrand lens in 4f configuration. In 4f configuration, the tube lens (TL), placed at f_{TL} (focal length of TL) distance from BFP of the objective lens forms a real plane image of the sample at its BFP. Now Bertrand lens (BL), placed at f_{BL} (focal length of BL) distance from BFP of TL, Fourier transforms the real plane image and creates conjugate BFP at the charge-coupled device (CCD), placed f_{BL} distance away from BL. Insets show an example of elastic scattering from a single silver nanowire. Bright-field image of NW illumination with LG beam is created by TL, which is Fourier transformed by BL to form BFP image of scattered LASER light at CCD. BFP has the resolution in angular coordinates, and the maximum angle is defined by the numerical aperture of collection objective lens.

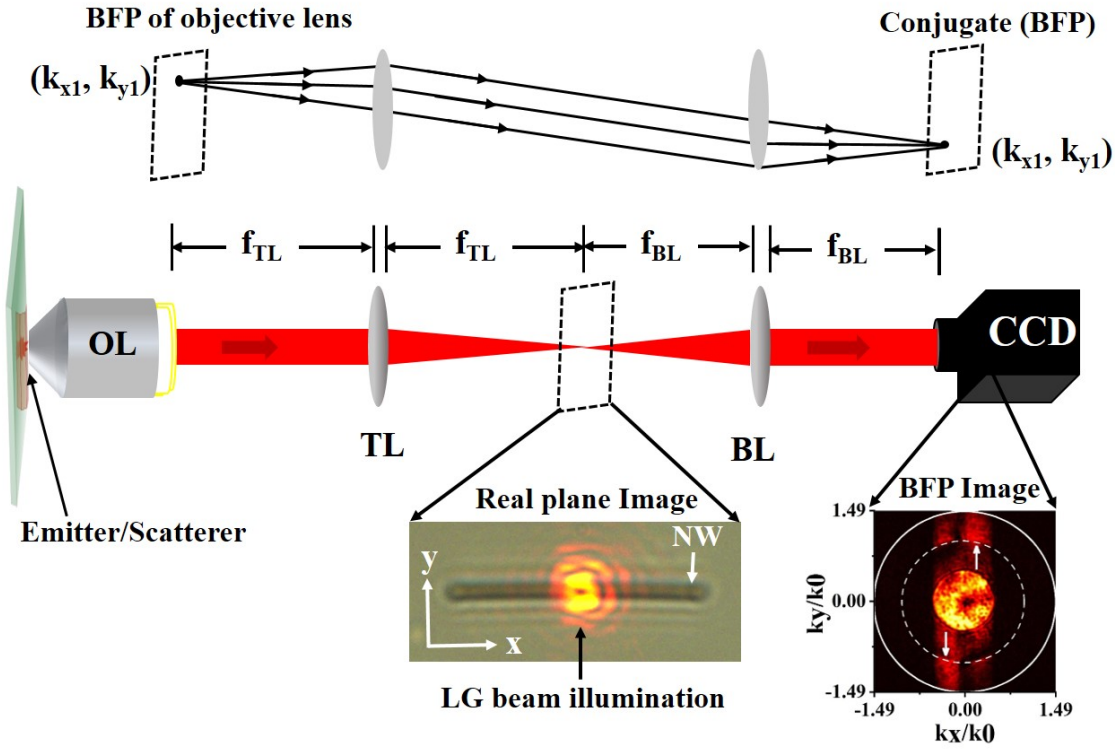

FIGURE 2.6: Schematic showing the implementation of the Fourier plane imaging technique in a microscopy system. A ray diagram shows the relaying of the back focal plane (BFP) of the objective lens (OL) using tube lens (TL) and Bertrand lens (BL) on to CCD. Insets show the scattering of LG beam from a silver nanowire at the real plane and back focal plane. Legends: k_{x1} and k_{y1} are wave vector components in the transverse plane. f_{TL} and f_{BL} are focal lengths of TL and BL respectively. CCD: charge-coupled device. NW: nanowire.

2.3 Architecture of the microscope

We have built a two-channel microscopy and spectroscopy system in the vertical configuration (a photograph of the same is shown in figure 2.7). The architecture of the system is described using a schematic shown in figure 2.8. The home built microscopy and spectroscopy systems consist of two objective lenses with different numerical apertures (NAs) to excite the sample placed on a piezo nanopositioning stage either through glass or from air-side.

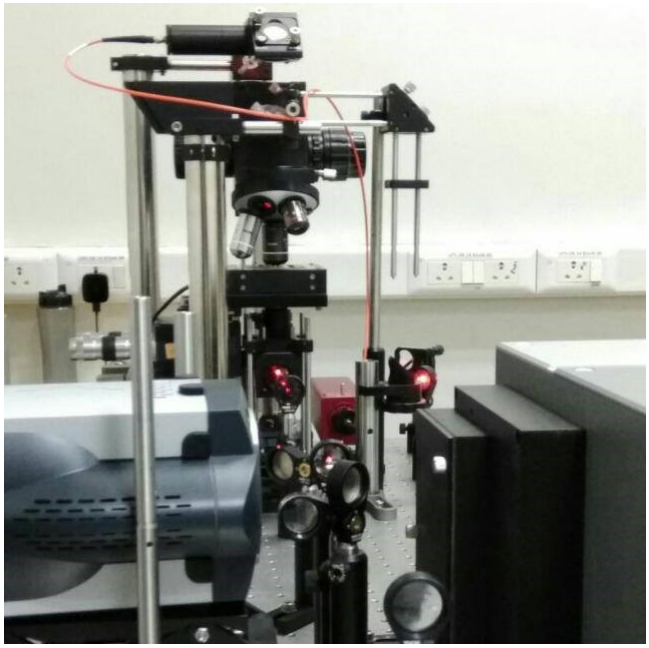

FIGURE 2.7: Photograph of home built two-channel microscopy system.

The piezo stage has a minimum step size of 1 nm and hence an individual nanostructure can be selectively excited using a high NA objective lens. The system has flexibility in terms of changing the objective lens according to the experiment under consideration. For the excitation of the nanostructure, there are continuous (532 nm and 633 nm, operational wavelength) and pulsed (140 fs pulsed width, 690 nm-1040 nm wavelength range) lasers integrated with the microscope. Scattered or secondary emission from the sample can be collected using either of the objective lenses to perform measurements in forward or backward scattering geometry. Collected emitted/scattered signal by the objective lens is now imaged at CCD or EMCCD (electron-multiplying charge-coupled device) using relay optics to perform real plane or Fourier plane imaging. The collected signal can also be sent to the spectrometer to perform conventional spectroscopy or dispersion imaging and energy-momentum spectroscopy. The signal can be spectrally and spatially filtered in the collection path using spectral filters and pinhole (placed at image plane) respectively. With the capability of excitation and collection from both

air and substrate (glass) sides, dual-channel optical microscopy system can be utilized to perform optical measurements in both backward and forward scattering geometry on structures placed on a transparent substrate. We have performed the following experiments in forward and backward scattering configurations:

- Forward scattering configurations:

  a. Scattering of angular momentum carrying beams from a single silver nanowire

  b. Wave vector switching of second-harmonic generation signal from a single DAAQ mesowire

- Backward scattering configuration: Transverse orbital momentum flow controlled surface plasmon polaritons generation in a plasmonic nanowire

In the following sections, we have explained separately the uses of forward and backward scattering geometries of the dual-channel microscope (shown in Figure 2.8).

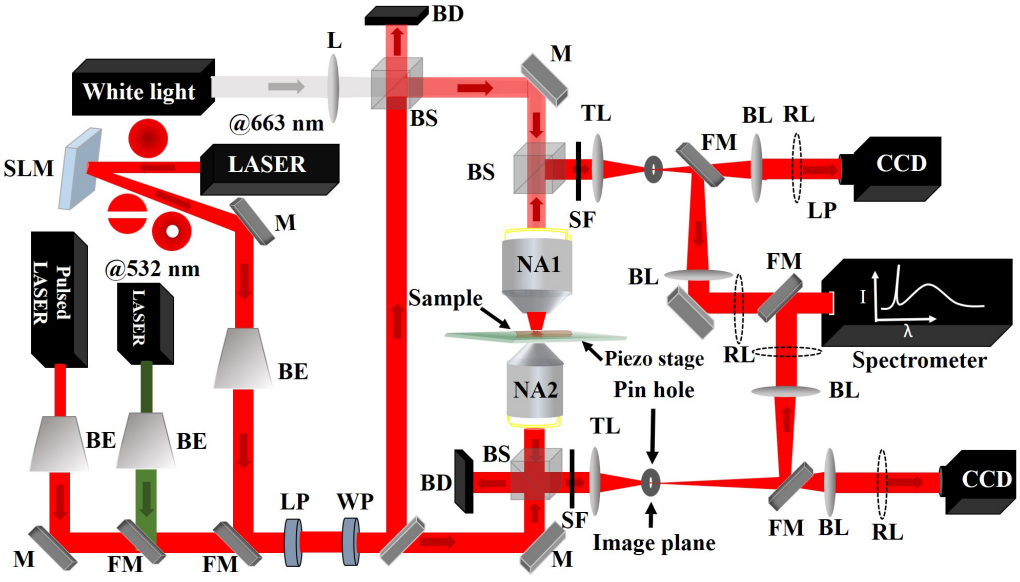

FIGURE 2.8: Schematic representing the architecture of home-built dual-channel microscopy system. Legends: NA: Numerical aperture, SLM: Spatial light modulator, BE: Beam expander, LP: Linear polarization, M: Mirror, FM: Flip mirror, WP, Wave plate (half or quarter-wave plate), L: Lens, BS: Beam splitter, BD: Beam dump, SF: Spectral filter, TL: Tube lens, BL: Bertrand lens, RL: Flip lens to form real plane image, CCD: Charge-coupled device.

2.4 Optical measurements performed

We have utilized dual-channel microscopy system in forward and backward scattering configurations for linear and nonlinear optical measurements.

2.4.1 Forward scattering configuration

Scattering of angular momentum carrying beams from a single silver nanowire: We have performed forward scattering measurements in the linear regime using forward scattering configuration of dual-channel microscopy setup, as shown in figure 2.9. An angular momentum carrying beam is focused on silver NW using a low NA objective lens (0.5 NA, 40X). Scattered light in the forward direction is collected using a high NA objective lens (1.49 NA, 100X) and is sent to CCD for real plane and Fourier plane imaging. We have asked questions related to the effects that SAM and OAM of a light beam create to the linear scattering of the light beam from the NW. In this regard, chapters 3 and 4 extensively discuss the optical Spin-Hall effect and detection of OAM states, respectively.

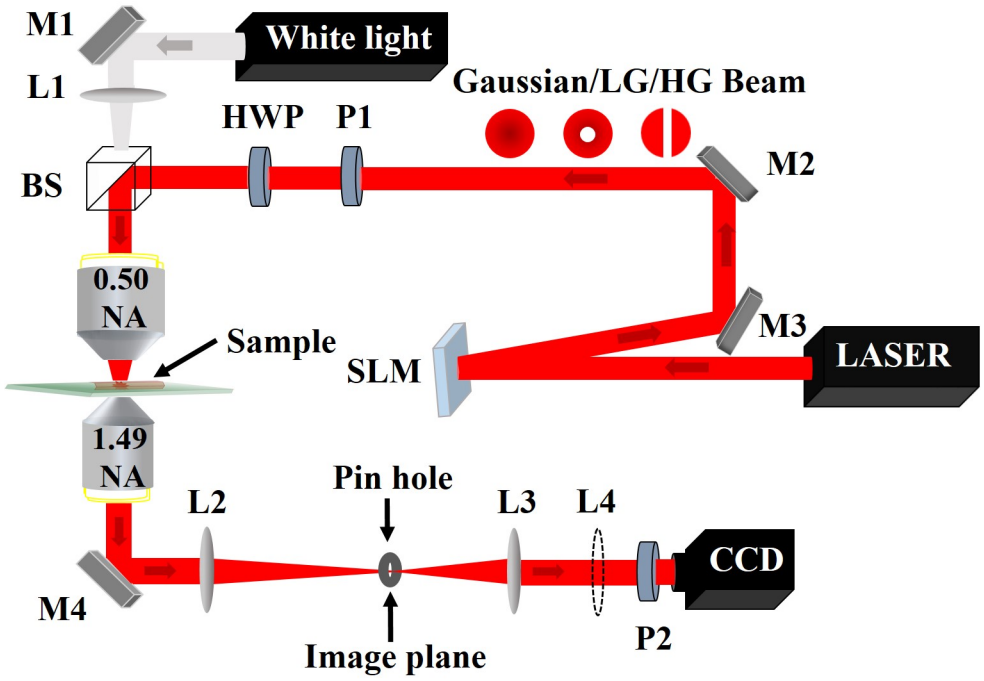

FIGURE 2.9: Forward scattering configuration for measurements of scattering of angular momentum carrying beam from a single Ag NW.

Wave vector switching of second-harmonic generation signal from a single DAAQ mesowire:

In this work, we have utilized selective excitation of different facets of a triangular cross-sectional DAAQ (1, 5 diaminoanthraquinone) mesowire to control the direction of the second-harmonic generation (SHG) signal. SHG measurements are realized using forward scattering configuration of dual-channel microscope (shown in figure 2.10). A high NA objective lens (1.49 NA, 100X) focuses light at different facets of the mesowire, and the forward scattered SHG signal is captured by a high NA objective lens (0.95 NA, 100X) and sent to CCD and spectrometer for Fourier imaging and spectroscopy respectively.

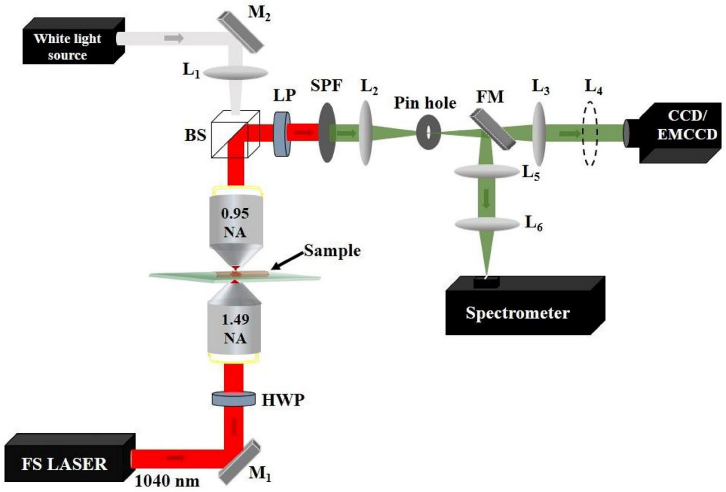

FIGURE 2.10: Forward scattering configuration for the measurement of second-harmonic generation directionality as a function of the scan of mesowire under tight focusing.

Directionality measurements are shown in figure 2.11. The mesowire is scanned across the laser focus using the piezo stage at 200 nm steps size to excite different facets of triangular cross-section mesowire. We have achieved 140-degree change in direction of SHG emission upon scan of mesowire across the laser focus. A detailed study is given in the appendix for control of SHG wave vector and its comparison with two-photon excited fluorescence.

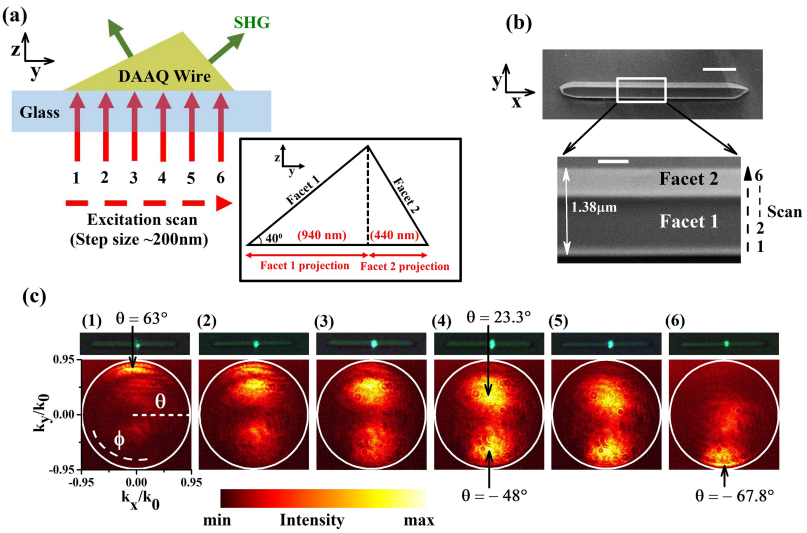

FIGURE 2.11: (a) Schematic showing positioning of laser focus along the short axis of the mesowire. (b) FESEM image showing the triangular cross-section of the mesowire. (c) Directionality measurements of SHG using Fourier plane imaging as a function of excitation scan across the mesowire.

2.4.2 Backward scattering configuration

Transverse orbital momentum flow controlled surface plasmon polaritons generation in a plasmonic nanowire:

We have studied the effect of transverse orbital momentum flow on surface plasmon polaritons (SPP) generation in a silver NW using the backward scattering configuration of dual-channel microscopy setup. In these experiments, a high NA objective lens (1.49 NA, 100X) is utilized to focus LG beam on one of the extremities of the NW to generate SPP in the NW. NW now is scanned across the vortex using the piezo stage, and SPP coupling to NW is observed by collecting backward scattered light using the same objective lens. A detailed description on OAM controlled SPP coupling to NW is given in chapter 5.

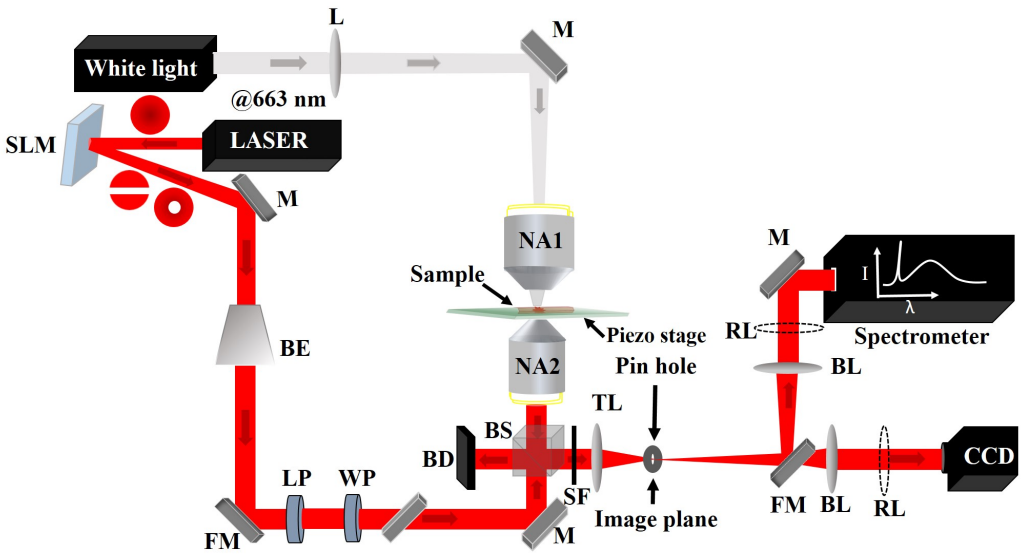

FIGURE 2.12: Backward scattering configuration for the study of OAM controlled SPPs coupling in an Ag NW.

2.5 Dispersion imaging and energy-momentum spectroscopy

Dual-channel microsocpy system can also be utilized for dispersion imaging and energy-momentum spectroscopy. Following are the examples for the same:

Dispersion imaging

For the dispersion imaging of a polychromatic signal, the real plane image is dispersed using grating in the spectrometer. Figure 2.13 [53] shows a dispersion image of nonlinear photoluminescence from a single gold NW. Dispersion image gives information about the wavelength distribution of nonlinear photoluminescence along the NW, which cannot be resolved in the real plane image.

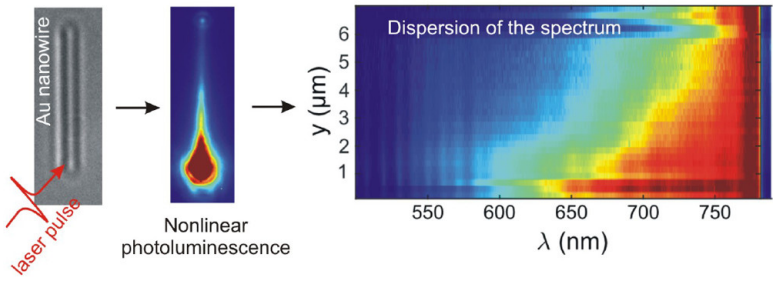

FIGURE 2.13: Figure consists of FESEM image of the NW, real plane image of nonlinear photoluminescence from NW and dispersion diagram of nonlinear photoluminescence showing missing of shorter wavelengths along the NW as a function of distance from excitation end. Figure has been adapted with permission from [53]. © (2019) American Chemical Society

Energy-momentum spectroscopy:

The back focal plane of the emitted/scattered polychromatic light can be projected to the spectrometer slit to perform energy-momentum spectroscopy. Spectrometer slit selects a narrow range of wave vectors along an axis of BFP image and the grating of the spectrometer disperses it. In this way, we have information about wavevector on one axis and wavelength information on other axis, giving an energy-momentum diagram. Figure 2.14 shows an energy-momentum diagram of molecular signals from a plasmonic NW-film cavity [54]. The energy-momentum diagram shows the difference in wavevector distribution of Raman and fluorescence signal from the cavity. Raman signal is uniform along all wave vectors, but maximum fluorescence signal is directional and comes at large wavevectors. This differentiation of wavevectors of two signals, which overlap in the spectral range is not possible using only Fourier imaging.

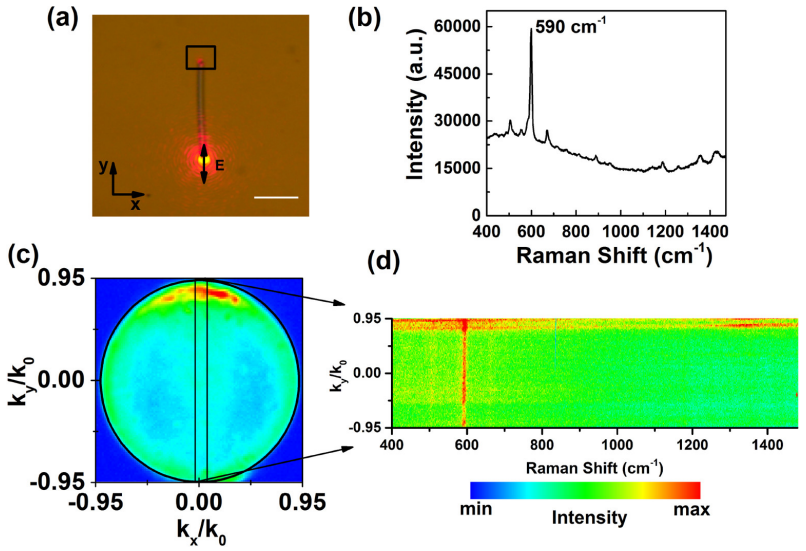

FIGURE 2.14: (a) Excitation of plasmonic NW-film cavity using 633 nm laser. (b) Spectrum showing overlapping of Raman and molecular fluorescence of Nile blue molecules from the cavity. (b) Selection of a strip along k_y/k_0 of BFP using slit of spectrometer. (d) Energy momentum diagram of the molecular signals. Figure has been adapted with permission from [54]. © (2017) American Chemical Society

Chapter 3

Spin momentum flow controlled far-field scattering of structured light from a plasmonic nanowire: Optical Spin-Hall effect

In this chapter, I discuss preferential radiation direction (preferential scattering) governed by the spin momentum flow in the forward scattering of light beams from a plasmonic nanowire as a manifestation of the Spin-Hall effect. The chapter is an adaptation of the research article "Opt. Lett., 43, 2474-2477 (2018)".

3.1 Introduction

In free space propagation, three forms of angular momentum (AM) i.e., spin angular momentum (SAM), intrinsic and extrinsic orbital angular momentum (OAM) are independent and conserved. However, because of Spin-orbit coupling, interconversion between different forms of AM is possible. Transformation of SAM to intrinsic-OAM are reported in high NA focusing, space-variant subwavelength gratings and liquid crystal devices [55–57]. Intrinsic AM (SAM or intrinsic-OAM) to extrinsic-OAM conversion is called as Hall effect (spin-Hall or orbital-Hall) and also known as optical Magnus effect [58]. This effect is observed in beam reflection or refraction [59, 60], propagation through medium [61–63] or metamaterial [64] and scattering [65–67]. Spin-orbit effects cover a wide class of electromagnetic phenomena such as focusing, reflection, scattering, light propagation and light-matter interactions. Therefore, Spin-orbit coupling can be utilized in emerging photonic applications for the generation of structured light, enhanced optical manipulation and controlling optical wave propagation [68]. In the past, manifestation of spin-orbit coupling is reported in scattering of Gaussian beam from a spherically symmetric particle [65, 69–71] except for a few reports on the use

of structured light or aspherical geometry [66, 72, 73]. These effects are weak and one of the important aspects is to enhance them in terms of Spin-Hall shift (separation of orthogonal circular polarization) and signal strength (intensity of orthogonal circular polarization analogous to Hall voltage). General consideration is on the enhancement of Spin-Hall shift [74, 75]. Plasmonic structures have been proposed as potential candidate for the enhancement of Spin-Hall signal [76, 77]. It is also reported that structured-light matter interaction enhances the optical manipulation [68]. Motivated by this, we use a combination of structured light and a plasmonic nanowire to enhance the Spin-Hall effect. We found that there is significant enhancement in the Spin-Hall signal for Hermite-Gaussian beam over Gaussian beam. The additional advantage of using Hermite-Gaussian beam is that, nodal line acts as the marker of the Spin-Hall shift, i.e. respective orthogonal circular polarization can be found on either side of nodal line.

3.2 Forward light scattering from single silver nanowire

Experimental observations of the Spin-Hall effect were realized using Fourier plane (FP) microscopy of forward scattered light as shown in the schematic (Figure 3.1). Here we have utilized upper channel of the home built two-channel Fourier microscope as an excitation path and lower channel as collection path for forward scattering of light from a single nanowire (NW) (see Figure 2.9, chapter 2 for complete experimental setup). Single crystalline Ag NWs were synthesized using standard protocol [78, 79] and were drop casted on a glass coverslip. After letting the ethanol evaporate for few minutes, we got self-assembled Ag NWs on the glass substrate with good monodispersity. Prepared NWs range from 300 nm to 400 nm in width with several microns in length. Gaussian mode (G) at wavelength 632.8 nm from He-Ne laser was projected on to the spatial light modulator (SLM) with blazed hologram to generate Hermite-Gaussian (HG) beam (figure 2.4, chapter2) [80]. Single Ag NW was illuminated with Gaussian or HG beam using low numerical aperture objective lens (0.5 NA, 50X) and forward scattered light through glass was collected using oil immersion objective lens (1.49 NA, 100X). Figure 3.1 (a) shows bright-field real plane image of excitation of a Ag NW of diameter 350 nm oriented along the x-axis with HG_{10} beam. For Fourier plane (FP) microscopy of forward scattered light, back focal plane of the collection objective was mapped at the CCD camera using relay lenses. Figure 3.1 (b) shows a FP image of forward scattered light from single Ag NW for left-hand circularly (LCP) polarized HG_{10} beam illumination.

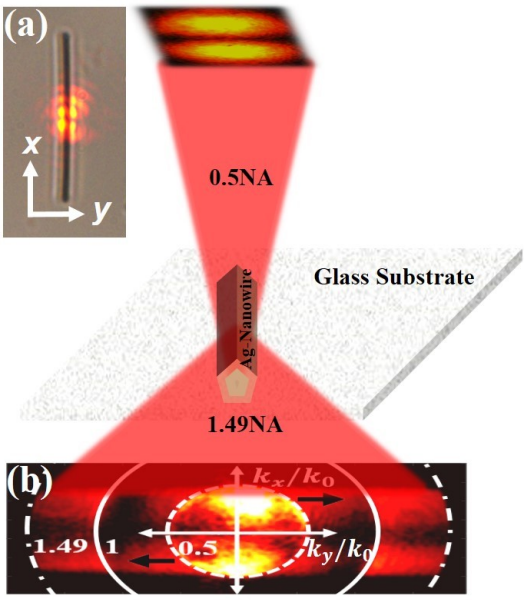

FIGURE 3.1: Schematic of the experimental configuration to observe Spin-Hall effect in the scattering from Ag-nanowire. Objective lens of 0.5 NA is used to focus structured light (HG_{10} beam) on the nanowire placed on glass substrate and forward scattered light is collected using 1.49 NA oil immersion object lens. (a) Bright-field image of focused HG_{10} beam on nanowire. (b) Experimentally observed scattered far-field of LCP HG beam. The white circles represent respective NA values and black arrows show the preferential scattering directions

3.3 Polarization-dependent scattering of Gaussian beam

Figure 3.2 (a) and (b) show experimentally observed FP images of the scattered Gaussian beam with polarization along and perpendicular to Ag NW aligned along x-axis. Scattered light spreads as a lobe along k_y/k_0 axis in the FP image with a finite width along k_x/k_0 defined by the numerical aperture of the illumination objective lens (0.5 NA). For the analysis of FP image, there are two regions of interest, subcritical or allowed (NA < 1) and supercritical or forbidden (NA > 1), depending upon the origin of the light [30]. For incident beam polarization along the Ag NW, light is mostly confined to subcritical angles (NA < 1) (Figure 3.2 (a)) but it spreads over supercritical angles (1 < NA < 1.49) for polarization perpendicular to Ag NW. This can be accounted for the accumulation of the electric field in the vicinity of the Ag NW for transverse polarization. In order to support our experimental results, we carried out finite element method based simulation using COMSOL Multiphysics 5.1 to calculate the near-field electric field and near-to-far-field transformations were computed by utilizing reciprocity arguments [81]. Ag NW with pentagonal cross-section of diameter 350 nm and 5μm in

length was used in simulations. The wire was placed on a glass substrate with refractive index 1.52 and surrounded by air (refractive index 1). Wavelength dependent refractive index of silver was obtained from [82]. Polarized Hermite-Gaussian or Gaussian beam of wavelength 633nm was focused on to the nanowire-glass interface. The simulation area was meshed with free tetrahedral mesh of minimum element size 10 nm and terminated using scattering boundary condition to avoid spurious reflections from the boundaries. Numerically calculated FP images shown in Figure 3.2 (c) and (d) for input polarization along and perpendicular to the NW show similar scattering pattern to the experimental observations.

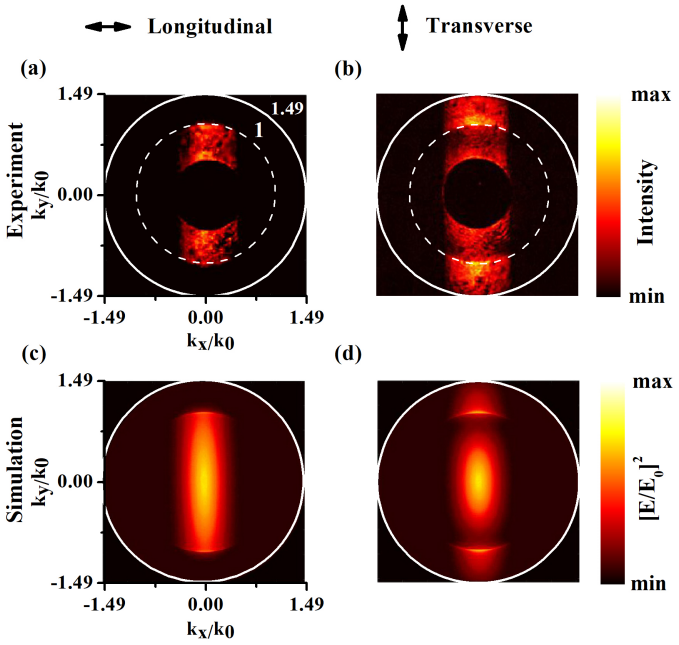

FIGURE 3.2: Scattering of Gaussian beam as a function of input polarization. (a) and (c) are experimentally measured and simulated FP images for input polarization along the long axis of NW respectively. (b) and (d) are experimentally measured and simulated FP images for input polarization transverse to the long axis of NW respectively.

3.4 Scattering of linearly polarized HG_{01} and HG_{10} beams

The intensity profile of Hermite-Gaussian (HG_{mn}) beam propagating in z-direction is determined by indices m and n along x and y-direction. Bright field real plane images in Figure 3.3 (a) and (b) show illumination of Ag NW aligned along x-axis with HG_{01} and HG_{10} beams polarized transverse to NW respectively. This makes the nodal line (no intensity line) along and perpendicular to the NW for HG_{01} and HG_{10} beam illumination respectively. Two intensity maxima separated by a nodal line in HG_{01} interact with NW

at the same point along x-axis and result in a single lobe in scattered FP image as shown in Figure 3.3 (c). But HG_{10} beams having nodal line transverse to NW interacts with NW at two points along length of NW and results in two lobes in the scattered FP image as shown in Figure 3.3 (d). Experimental observations are also corroborated with simulated FP images (Figure 3.3 (e) and (f)). Two lobe formation in the scattering of HG_{10} beam results in enhanced Spin-Hall effect for NW aligned along the x-axis in comparison to Gaussian beam and hence we consider HG_{10} beam for rest of the discussion.

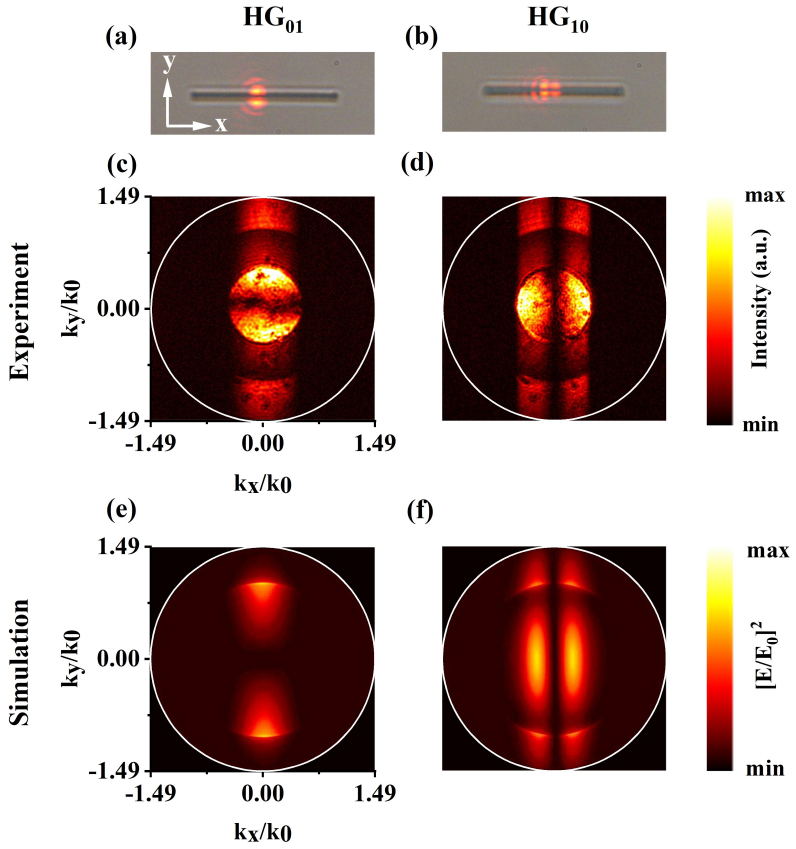

FIGURE 3.3: Scattering of HG_{01} and HG_{10} beams from Ag NW. (a) and (b) are the bright field real plane images showing illumination with HG_{01} and HG_{10} beams on Ag NW respectively. (c) and (d) are experimentally measured FP images showing the symmetric scattering of HG_{01} and HG_{10} beams respectively. Simulated FP images for HG_{01} (e) and HG_{10} (f) beams also confirm the symmetric scattering patterns in FP images.

3.5 Circular polarization induced preferential scattering

As shown in Figure 3.4 (a) and (d), linearly polarized Gaussian and HG beam results in symmetric lobes along the axis transverse to NW in scattered FP images. But these scattering patterns have handedness dependent antisymmetry along k_y/k_0 axis on either side of $k_x/k_0 = 0$ for circularly polarized beam illumination. In other words for left-hand circularly polarized (LCP) beam, we get preferential scattering along $+k_y/k_0$ ($-k_y/k_0$) direction for $k_x/k_0 < 0$ ($k_x/k_0 > 0$) as indicated by white arrows for Gaussian (figure 3.4 (b)) and HG_{10} (figure 3.4 (e)) beams.These pattern flip for right hand circularly polarized (RCP) beams as shown in figure 3.4 (c) (Gaussian beam) and (d) (HG_{10} beam). The effect of biased/preferential scattering is enhanced in the case of HG_{10} in comparison to Gaussian beam. This handedness dependent preferential scattering is a result of spin momentum flow component associated with circularly polarized beam [83, 84] and can be termed as optical Spin-Hall effect. In following sections, we analyze the preferential scattering and later using numerical simulations explain observed Spin-Hall effect and its enhancement in the scattering of circularly polarized HG_{10} beam over Gaussian beam.

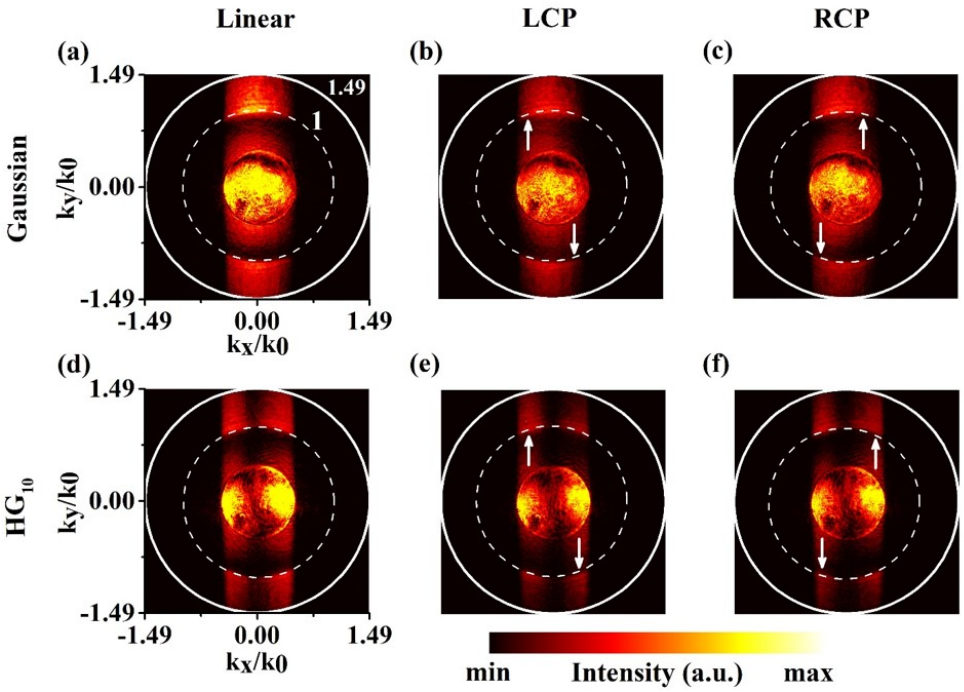

FIGURE 3.4: Circular polarization induced preferential scattering from Ag Nanowire. (a)-(c) Scattered FP images for linear (transverse to NW), left-hand circular polarized (LCP) and Right-hand circular polarized (RCP) Gaussian beam. (d)-(f) Scattered FP images for linear (transverse to NW), LCP and RCP polarized HG_{10} beam. White arrows in the FP images show preferential scattering induced by the handedness of the circular polarization.

3.6 Analysis of Spin-Hall effect in forward light scattering from Ag NW

In FP image, there are two regions of interest, subcritical or allowed (NA<1) and supercritical or forbidden (NA>1), depending upon the origin of the light [85]. The manifestation of Spin-Hall effect is prominent within the subcritical region; therefore, we have focused only in the region corresponding to 0.5-1.0 NA as shown in Figure 3.5. Region corresponding to NA < 0.5 was eliminated for containing unscattered light.

3.6.1 Experimental observations

Wire was aligned along the x- axis and centered at y=0. Far-field scattered power of left circularly polarized (LCP) HG beam in $+k_y$ and $-k_y$ directions are defined as $P_+(k_x, k_y)$ and $P_-(k_x, k_y)$ respectively, as shown in top and bottom of Figure 3.5 (a). Subscripts $\pm$ denotes power scattered along $\pm k_y$ directions. Here $k_x = k_x/k_0$ and $k_y = k_y/k_0$ are

the normalized wave vector directions and k_0 is the free space wave vector. Sum of the scattered power over all k_y is defined as $P_{\pm}(k_x) = \Sigma_{(k_y)} P_{\pm}(k_x, k_y)$ shown in Figure 3.5 (b). It should be noted that the intensity sum in far-field images is done using a Matlab program by adding the intensities at pixels of the image corresponding to different directions in the far-field image. The resolution of the plot depends on the magnification of the far-field pattern at the imaging camera. Higher is the magnification, fewer wave vectors will map to a pixel and hence higher will be the accuracy. Figure 3.5 (d) and (e) show $P(k_x)$ for right circular (RC), left circular (LC) and linearly (perpendicular to wire) polarized HG-beam and Gaussian beams respectively. From Figure 3.5 (d) and (e), it is clear that there is spin controlled preferential radiation direction in the scattered far-field. Black arrows in Figure 3.5 (c) pictorially show preferential scattering direction for LCP HG beam. To further quantify the amount of preferential scattering, difference of powers ($P_+(k_x)$ - $P_-(k_x)$) was plotted (Figure 3.6). It clearly shows that for LCP HG and Gaussian beams, preferential scattering is in $+k_y$ ($-k_y$) direction for $k_x<0(>0)$ forming an antisymmetric scattering pattern, which is reversed on changing the handedness of polarization. It also shows that the amount of preferential scattered power is significantly greater for HG-beam then for the Gaussian beam. It should be noted that powers of HG-beam and Gaussian beam were equal and these beams do not carry any orbital angular momentum. Hence, we have experimentally demonstrated: (1) Spin-Hall shift is on either side of the nodal line at the center of HG-beam, (2) the enhancement of Spin-Hall signal by utilizing structured light and plasmonic nanowire. These aspects of Spin-Hall effect are the result of spin momentum flow component of Poynting vector associated with circular polarization, as explained below using simulation results.

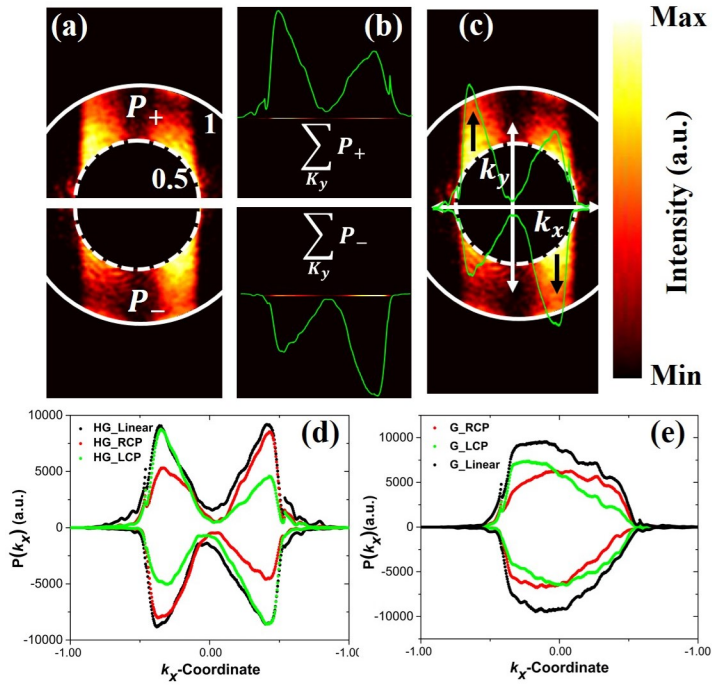

FIGURE 3.5: Analysis of Scattered far-field (Fourier plane image) from Ag-nanowire. (a) Fourier plane image showing region of interest (0.5 < NA <1.0) for observation of Spin Hall effect. (b) Definition of scattered powers along $\pm k_y$ wave vectors i.e. $P_{\pm}(k_x) = \Sigma_{(k_y)} P_{\pm}(k_x, k_y)$. (c) $P(k_x)$ superimposed on $P(k_x, k_y)$. (d) and (e) Distribution of $P(k_x)$ for LCP (green), RCP (red) and linear (black) Hermite-Gaussian and Gaussian beams respectively.

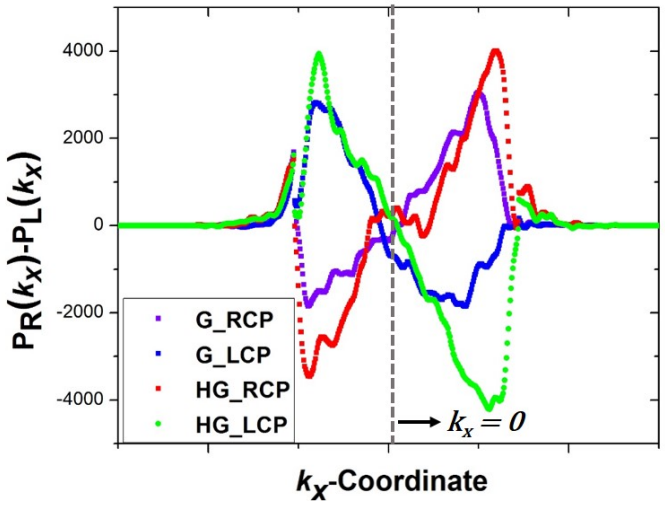

FIGURE 3.6: Optical Spin-Hall effect. Difference of power scattered perpendicular to long axis of nanowire, $P_{+}(k_x)$ - $P_{-}(k_x)$. Plots shown in the figure are the experimental results for Hermite-Gaussian (HG_LCP (green) and HG_RCP (red)) and Gaussian beams (G_LCP (blue) and G_RCP (violet) illumination.

3.6.2 Numerical simulations

Figure 3.7 shows the simulation configuration and near-field total Poynting vector in yz-plane at x = 0.1 μm for LCP HG-beam, where black arrows represent the total Poynting vector flow in the plane. Poynting vector gives the measure of energy/momentum flow in optical fields. As explained in chapter 1, total momentum flow can be decomposed into 'spin momentum flow' and 'orbital momentum flow' for paraxial fields [83] as well as for nonparaxial fields [84]. For a LCP HG_{10} beam, the calculated spin momentum flow ($\nabla \times \mathrm{Im}(\vec{E}^* \times \vec{E})$) is shown in Figure 7(a). It clearly shows two azimuthally asymmetric spin momentum flow vortices having center coinciding with maximum intensity points ($\pm 0.5\mu$m) of two lobes of HG_{10} beam. The spin momentum flow is proportional to the transverse gradient of the intensity. Therefore, we chose a yz-plane at x=0.1μm (near maximum spin momentum flow) to demonstrate the effect of spin momentum flow in near- and far-field shown in simulation configuration (Figure 7). Because of net circulating spin momentum flow in the direction of scattered power along -k_y wavevectors, the total energy flow (shown by black arrows in near field in yz plane at x=0.1μm) makes an angle with respect to normal (z-axis) to wire which is possibly giving rise to net energy flow in the -k_y direction in the scattered far-field. Total energy flow will be reversed for yz plane at x= -0.1μm because of opposite spin momentum flow. Hence in the far-field we found a net energy flow (preferential scattering power) in +k_y (-k_y) direction for $k_x < 0$ ($k_x > 0$) as shown by black arrows in Figure 7(b). Similar explanation holds for RCP HG_{10} beam and the corresponding figures are shown Figure 7(e)-(f). For linearly polarized (perpendicular to the wire) HG_{10} beam there will not be any spin momentum flow, therefore far-field is symmetric with respect to k_x-axis without any preferential scattering.

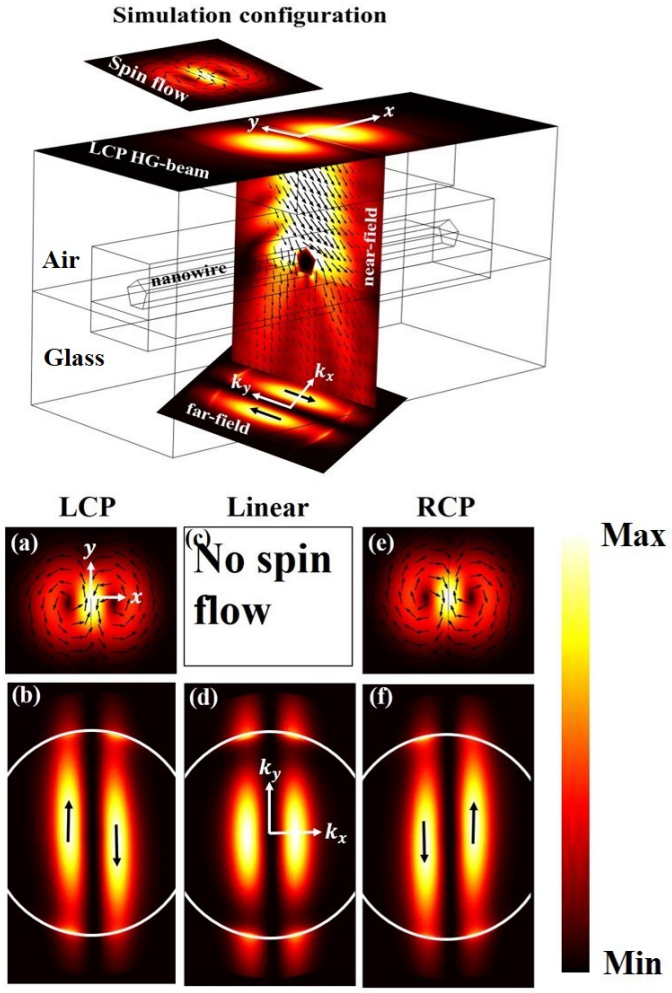

FIGURE 3.7: Simulation configuration (Details about different parameters used in simulations are given in section 3.3) and results for HG_{10} beam. (a) and (e) are the spin momentum flow for the LCP and RCP HG_{10} beams. Zoomed in view of center of figure (e) shows zero spin momentum flow along the nodal line. Arrows show the local spin momentum flow directions and the background is its magnitude. (b) and (f) are the corresponding scattered far-field respectively. (d) Scattered far-field of HG-beam linearly polarized. Black arrows and white circles in far-field shows the preferential scattering direction and NA value of 1 respectively.

In contrast to HG-beam, scattered far-field of Gaussian beam has only one intensity lobe instead of two in FP image [86], because of absence of intensity minimum due to no nodal line at center of the beam. Spin momentum flow for LCP and RCP Gaussian beam is given in Figure 3.8 (a) and (e) respectively. Spin momentum flow vortex has a singularity at the center of Gaussian beam with azimuthally symmetric spin momentum flow, unlike HG beam. Following the similar line of thought as before, spin momentum flows and corresponding scattered far-field of LCP, linear and RCP Gaussian beams are

shown in Figure 3.8. Because of vortex spin momentum flow, intensity lobe (along k_y axis) in FP image gets weakly rotated in the direction of the handedness of spin flow. Similar kind of energy shift is theoretically reported in the diffraction of circularly polarized Gaussian beam [73]. In addition, directional scattering of circularly polarized light from plasmonic and dielectric scatterers is also reported in [87–89].

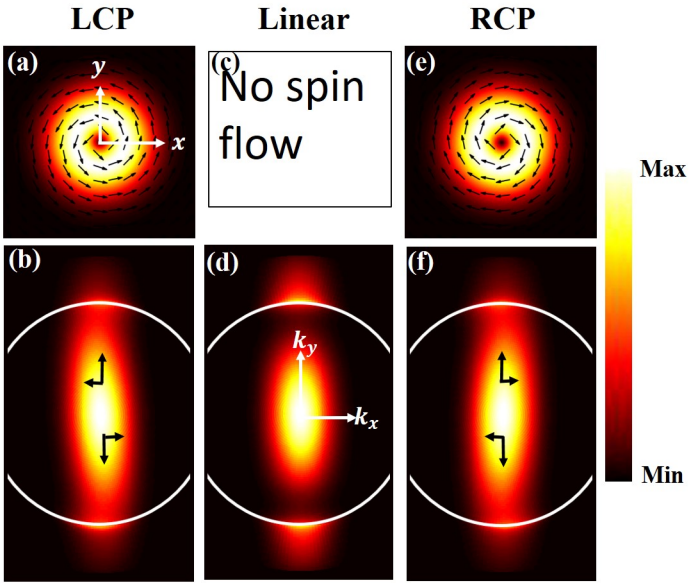

FIGURE 3.8: Simulation results for Gaussian beam. (a), (c) and (e) are the spin momentum flow for the LCP, linear and RCP HG-beams, (b), (d) and (f) are the corresponding scattered far-field respectively. Black arrows in far-fields represent the total energy flow components. Remaining details are same as in Figure 7.

Finally, a plot (Figure 3.9) of difference of total power scattered ($P_+(k_x)$ - $P_-(k_x)$) perpendicular to the nanowire (as calculated above for experimental data) is extracted from the simulated results. This plot shows the contribution of spin flow on the scattered power from the nanowire. We can see that the maximum preferential scattered power for HG-beam is nearly double as compared to Gaussian beam, proves the enhancement of Spin-Hall signal. This enhancement in far-field scattering of HG-beam because of spin flow component perpendicular to the nanowire is significantly higher than along the nanowire. Whereas for the case of Gaussian beam, spin flow has equal components perpendicular and along the nanowire. Along the nanowire component results in the Spin-Hall shift that is seen as the weak rotation in $\pm k_x$. It is worth noting that, enhancement in the scattered power due to Spin-Hall effect is because of the spin flow component perpendicular to the nanowire. Whereas, Spin-Hall shift arises due to spin flow component along the nanowire.

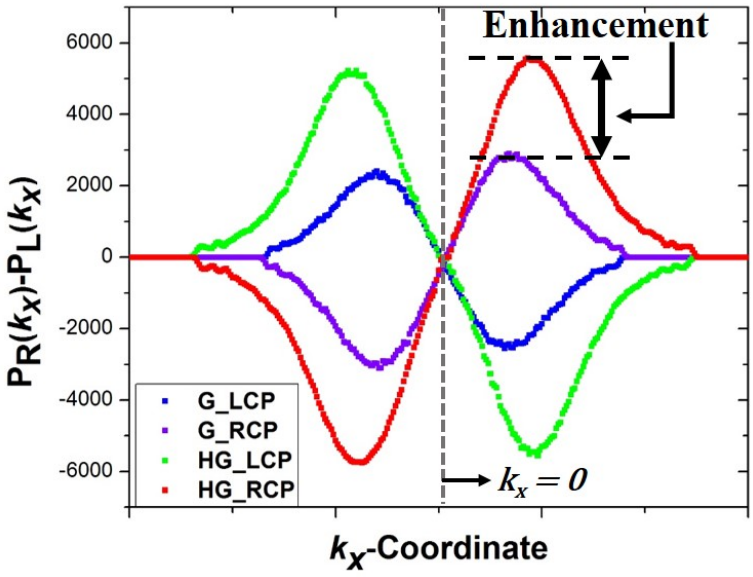

FIGURE 3.9: Enhancement of Spin-Hall effect. The difference of power scattered perpendicular to the long axis of the nanowire, P_+ (k_x) - P_- (k_x). Plots shown in the figure are the simulated results for Hermite-Gaussian (HG_LCP (green) and HG_RCP (red)) and Gaussian beams (G_LCP (blue) and G_RCP (violet) illuminations.

3.7 Conclusion

In summary, the chapter discusses experimental observation of Spin-Hall effect in the scattering from a plasmonic nanowire. Spin-Hall effect is quantified by taking the difference of scattered powers perpendicular to the long axis of wire and explained on the basis of spin flow component of the Poynting vector associated with circular polarization. Simulation results reveal that scattered power difference is nearly double for HG-beam than for Gaussian beam. With the advent of nanofabrication, Spin-Hall effect has immense potential for spin-controlled nanophotonic devices [64, 90, 91]. This study may find direct application in enhancement of Valley-Hall effect [92] and secondary emission [76].

Chapter 4

Discrimination of orbital angular momentum states of vortex beam using scattering from a silver nanowire

This chapter is an adapted version of the research article "ACS Photonics, 6, 1, 148-153 (2019)". Article discusses optical orbital angular momentum read-out using elastic scattering of vortex beams from a self-assembled silver nanowire. The method is based on recognition of far-field patterns captured using Fourier plane imaging of forward elastic scattering from nanowire.

4.1 Introduction

Orbital angular momentum (OAM) is a result of the azimuthal phase gradient in vortex beams and can have infinite many orthogonal states depending on spatial phase structure. Laguerre-Gaussian beams carrying OAM are widely used optical vortex beams. The beams are termed as LG_m^l beams, where l represents the azimuthal index (topological charge/mode number of OAM) and m represents the radial index. Topological charge l also means that vortex beam carries $l\hbar$ OAM per photon [93]. An azimuthally varying phase term $e^{il\phi}$ (where ϕ is the azimuthal coordinate) in vortex beam makes the wavefront of these beams to trace a helical path with a phase singularity at its center. Conventionally, vortex beams have been extensively studied in the context of optical communication [94–96]. They also find applications in stellar vortex coronagraphy [97, 98], sensing [99] etc. Use of these beams are not limited to macroscale; they have been harnessed at micron and sub-micron scale for quantum memory device [100], optical tweezers [16, 101, 102], nonlinear optics [103–105], and many more.

Accessibility to infinite orthogonal states of OAM makes vortex beam an unparalleled optical carrier for large information transfer. It has been observed that multiplexing of OAM can enhance information transfer by many folds [94]. But this capability leads

to the challenge of reading different OAM modes at the detection end, especially at scales comparable to wavelength of light. Identification of different OAM modes has been studied and realized at larger scales using conventional interferometric [106, 107] and diffraction [17] measurements or using transformation optics [108, 109]. Recent development in the nanofabrication has made the detection of OAM possible at even much smaller scale [36–38, 110]. But complicated structure and large size of these devices may constrain their integration in a compact nanophotonic circuit. At nanoscale, plasmonic structures with large optical scattering cross-section exhibit unique way to read OAM modes and recent efforts have shown great promise [111, 112]. Until now, the reported methods utilize complex plasmonic architectures, which are challenging to fabricate on large scale, and require clean room facility. There is an imperative for research on simple plasmonic nanostructures that can read the OAM modes unambiguously. More so, if the said nanostructures can be prepared by bottom-up nanofabrication techniques using chemical synthesis, then they can be functionalized, manipulated and integrated using processes such as self-assembly.

Motivated by these issues, we have utilized Fourier plane (FP) imaging of elastic scattering of vortex beams from a single silver nanowire for the read-out of different states of OAM. Plasmonic nanowire made of sliver and gold has been realized as subwavelength waveguide optical antenna [113–116], sensor [117], nonlinear optical antennas [118, 119] and as a platform to study spin-orbit coupling in light scattering [120]. They are yet to be harnessed as OAM sensor and to this end, we have utilized elastic scattering of light from individual sliver nanowire for the detection of OAM. Importantly, we discriminate the magnitude and sign of the OAM by directly reading scattered patterns in the far-field.

4.2 Architecture for OAM detection

Chemically synthesized Ag nanowires (NWs) [121] are dropcasted on a glass coverslip. Measurements are performed on a sample containing wires with width ranging from 300 nm to 400 nm to confirm the reproducibility of the experiment. But all measurements presented here are from single NW with diameter equal to $\sim$360 nm. Figure 4.1 (a) shows a schematic of FP imaging of forward scattered light from a single Ag NW. Inset (Figure 4.1 (a)) shows real plane bright field optical image of representative NW illuminated with LG beam. NW is oriented along the x-axis as indicated in bright field optical image of NW. Figure 4.1 (b) shows a FP image of the transmitted LG_0^1 beam having no NW in the focus of the beam. Figure 4.1 (c) shows the farfield scattering pattern of the LG_0^1 beam in the presence of NW in focal regime of the beam. Presence

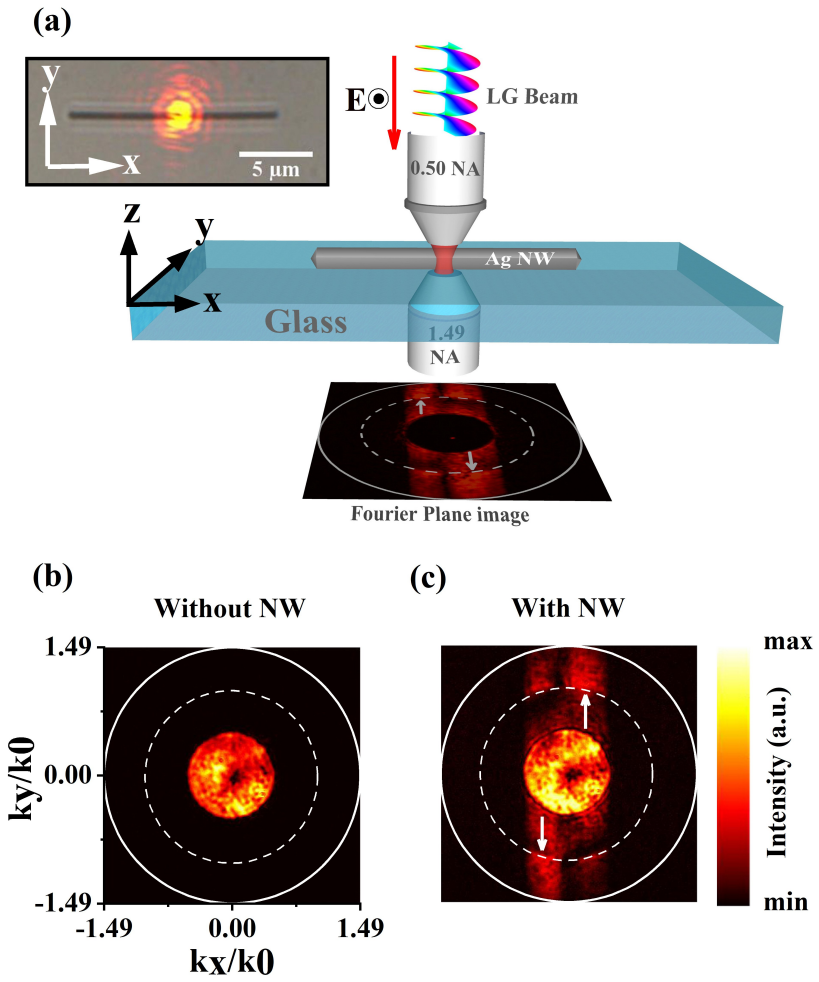

FIGURE 4.1: (a) Schematic describing Fourier plane (FP) imaging of forward scattering of Laguerre-Gaussian (LG) beam from Ag nanowire (NW) placed on a glass coverslip. Back focal plane of the collection objective lens is captured for the analysis of far-field. The inset shows real plan bright field optical image of NW illuminated with LG beam. FP images (b) without and (c) with NW in the focal region for LG_0^1 beam illumination. Inner dotted circle in FP images represents critical angle of air-glass interface. k_0 is free space wavevector. White arrows in FP image show preferential scattering.

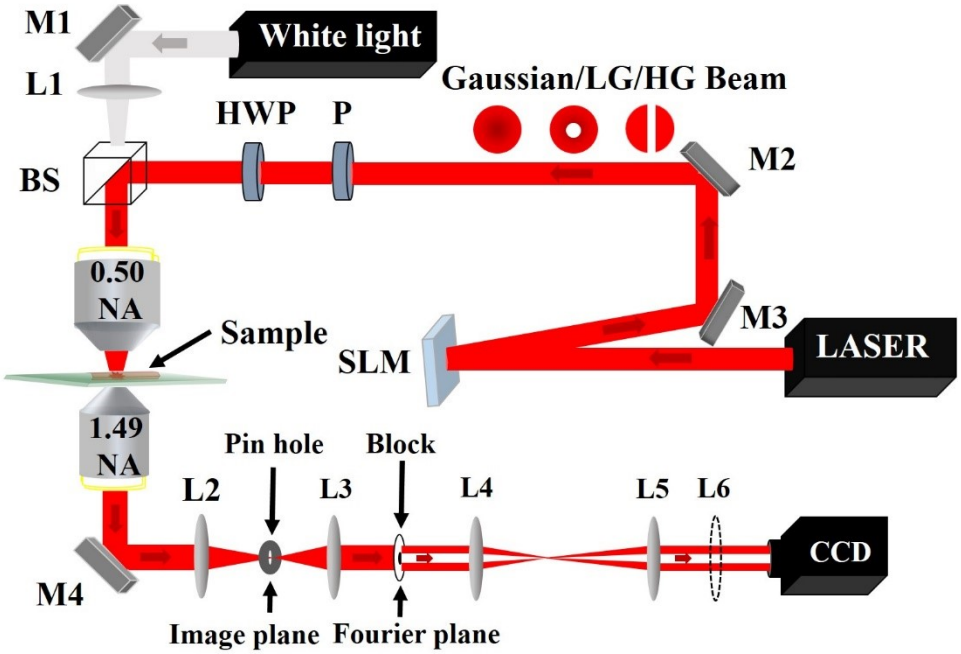

FIGURE 4.2: Detailed experimental setup. M1-M4: Mirrors, L1-L5: Lenses, L6: Flip lens, BS: Beam splitter, HWP: Half Wave plate, P: Polarizer, SLM: Spatial light modulator and CCD: Charge Coupled Device. Illumination objective lens (0.50 NA, 50x) focuses Gaussian, Laguerre-Gaussian (LG) or Hermite Gaussian (HG) beam generated by SLM using the Gaussian output of the He-Ne laser (633 nm wavelength). Forward scattered light is collected by a high numerical aperture objective lens (1.49 NA). Back focal plane of collection objective lens (1.49 NA, 100x) was imaged at CCD using lenses L2- L5 to measure Fourier plane (FP) image. A Flip lens L6 was used to get the real plane image of the sample.

of OAM in the beam is represented by a unique scattering pattern in the FP image and hence makes the NW a good platform to characterize OAM. A detailed experimental setup is shown in Figure 4.2. We have used spatial light modulator (SLM) with off-axis blazed holograms to generate LG and HG beams [122]. SLM modulates the phase of the incident Gaussian beam (633 nm wavelength) from He-Ne laser to convert it into LG or HG beam. First diffracted order from SLM is filtered through an aperture and sent to microscopic objective (0.50 NA, 50x) as Gaussian, LG or HG beam for the illumination of individual NW. Forward scattered light was captured with high numerical aperture objective lens (1.49 NA, 100x). Fourier plane (FP) image of the forward scattered light is captured by imaging back focal plane of the collection objective lens on to the charge coupled device (CCD). A pinhole was introduced at the image plane to collect signal only from excitation position on NW and hence to avoid scattering from other parts of the sample. Unscattered light was blocked using a block at the conjugate back focal plane in the collection path.

In what follows, we show how the scattering pattern of LG beam differs from other kind of beams and also utilize the patterns to discriminate the magnitude and sign of the topological charge of OAM carrying beams.

4.3 OAM induced preferential scattering in far-field

First we compare how nanowire scattering pattern of LG beam differs from conventional Gaussian beam. Figure 4.3 (a) shows scattered FP image of Gaussian beam with input polarization aligned along y-axis, transverse to the long axis of NW. The direct illumination near $k_x/k_0 = k_y/k_0 = 0$ is blocked and appears as black disk corresponding to a region of NA of illumination objective lens (0.50 NA) in the FP image. Scattered light spreads along k_y/k_0 wave vectors with small distribution along k_x/k_0 axis. Scattering along k_x/k_0 is dependent on focusing of incident beam, and its spread increases with increase in NA of illumination objective.
Figure 4.3 (b) shows FP image of forward scattering for transversely polarized LG_0^{-1} beam. We get preferential radiation direction (preferential scattering) indicated by white arrows in FP image. Biased scattering can be attributed to OAM in the LG beam [123]. Due to the presence of OAM in LG beams, Poynting vector circulates around intensity null. This makes Poynting vector directions to be opposite for two interaction positions on both sides of the singularity of the beam on wire. Thus the far-field scattering pattern is biased as per the OAM characteristics of the beam as shown in Figure 4.3 (b). Signature of the OAM in scattered far-field does not change as a beam moves along the length of the NW as shown in Figure 4.4. Hence the method is rendered to be robust with respect to positioning. But length of the NW should be greater than the spot size to avoid scattering from ends of the NW

Next, we compare the scattering patterns due to LG beam and Hermite-Guassian (HG) beam that has singularity but no angular momentum. These beams have a nodal line at the center as evident in the image above Figure 4.3 (c). The scattering pattern is symmetric in FP image for transversely polarized HG_{10} beam (Figure 4.3 (c)). The absence of intensity at wave vectors along k_y/k_0 axis near $k_x/k_0 = 0$ is a consequence of singularity and nodal line at the center of LG and HG beams respectively.

The experimental observations in Figure 4.3 (a-c) were corroborated by full-wave 3D finite element method (FEM) simulations using COMSOL Multiphysics (version 5.1) commercial software. Ag NW is modeled with a geometry having a pentagonal

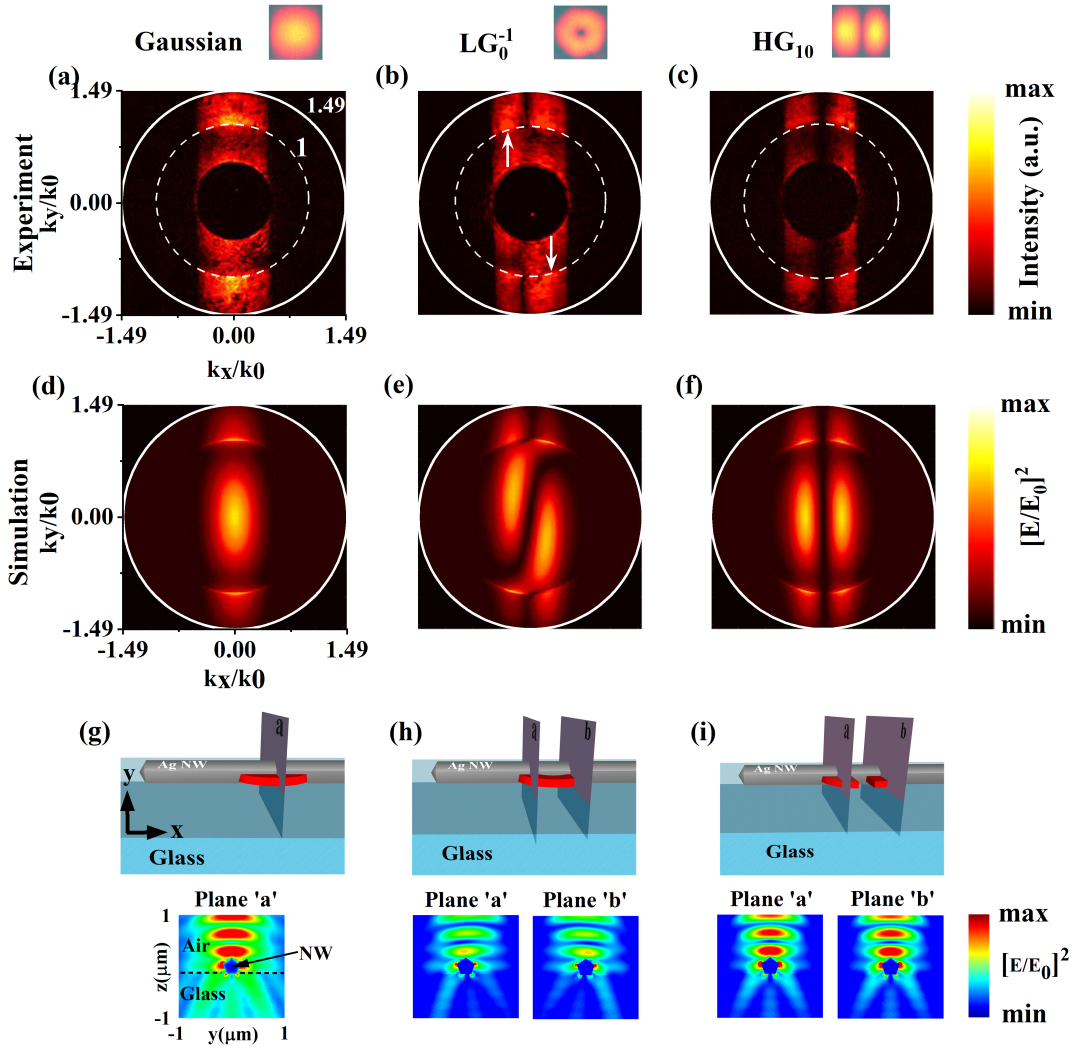

FIGURE 4.3: Fourier plane (FP) images highlighting orbital angular momentum (OAM) induced preferential scattering (indicated by white arrows) from NW for incident LG beam in comparison to symmetric scattering for Gaussian and HG beams. Top insets show beams after the SLM. Experimentally measured FP images showing farfield scattering from NW (aligned along the x-axis) for transversely polarized incident (a) Gaussian beam, (b) LG_0^{-1} beam, and (c) HG_{10} beam. (d)-(f) are corresponding simulated FP images corroborating experimental observations of scattering from different beams. Input powers used at the back aperture of illumination objective lens were 70 nW (Gaussian Beam), 68 nW (LG_0^{-1} beam) and 60 nW (HG_{10} beam). Simulated scattered near-field electric field (SNFEF) distributions are shown for (g) Gaussian beam, (h) LG_0^{-1} beam and (i) HG_{10} beam. Schematics in these figures show positions of cross-sectional planes (y-z planes) of SNFEF distribution across NW for different beam illuminations. SNFEF has asymmetric distribution for LG_0^{-1} beam in comparison to symmetric distributions for Gaussian and HG_{10} beams across NW.

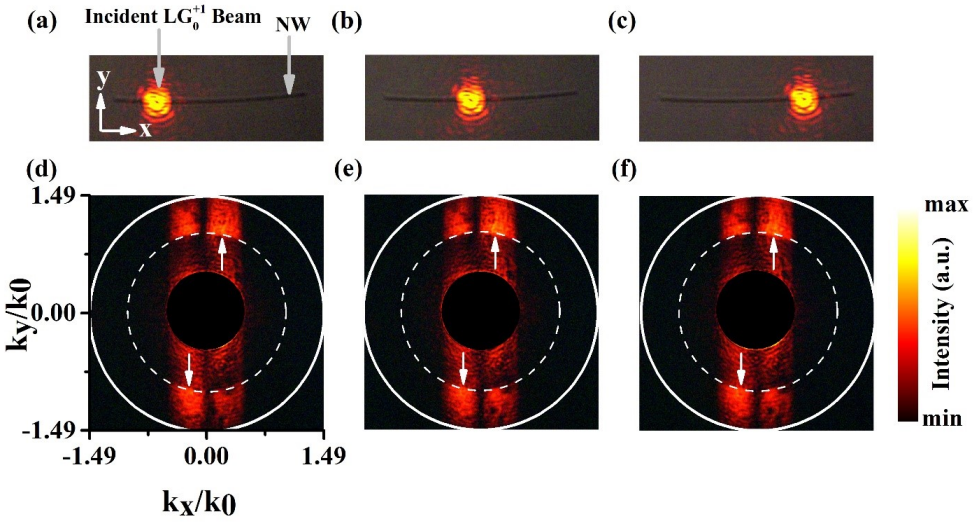

FIGURE 4.4: (a)-(c) Illumination of NW with LG_0^{+1} beam at three different positions along the length of the NW. (d)-(f) Corresponding FP images for different illuminations shown in (a)-(c) respectively showing similar scattering patterns.

cross section with diameter 350 nm and length 5μm, placed on a glass substrate. Wavelength dependent refractive index of Ag is taken from[124]. The system is meshed with the free tetrahedral mesh of size 20 nm to ensure accuracy. A single NW on glass is illuminated with beam (Gaussian, LG, and HG) of wavelength 633 nm with beam waist (633 nm) maintained at NW-glass interface to introduce similar focusing conditions as of experiment. The local electric field is calculated, and the near-field to far-field transformation is performed using reciprocity arguments [125]. Simulated FP images of forward scattering shown in figure 4.3 (d-f) are in good agreement with experimentally observed scattered far-field for different beam illuminations. To further understand the effect of OAM on scattering we have analyzed the simulated scattered electric field distribution near NW for illumination with different beams. OAM present in LG beam results in asymmetric spatial distribution of scattered near field in comparison to symmetric distribution for Gaussian and HG beam illuminations as shown in Figure 4.3 (g-i). Near field electric field calculations also show localized plasmon generation at the excitation position. It should be noted that there is no propagating plasmon mode being excited as interaction of free space photons at the center of NW does not possess enough momentum for the generation of surface plasmon polaritons in NW.

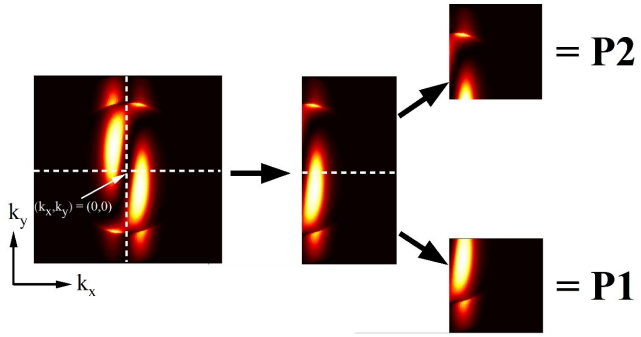

FIGURE 4.5: Schematic for directionality measurements

4.3.1 Effect of different parameters of beam and NW on OAM induced preferential scattering in farfield

We explored different parameters of beam and NW to check the robustness of the technique using FEM simulations. A quantitive parameter 'directionality value' for preferential scattering was calculated to compare scattering patterns as a function of change in different parameters of beam or NW.

Definition of directionality value

Figure 4.5 shows method of directionality calculation of preferential scattering in FP image. We have taken one lobe from the scattering pattern of the LG_0^{-1} beam for measurements as the other lobe is exactly flipped image of this one. Now power scattered in upper half (along $+k_y$ wave vectors) is defined as P2 = $\Sigma_{(k_x>0),(k_y>0)}P(k_x, k_y)$ and power scattered in lower half (along $-k_y$ wave vector) as P1 = $\Sigma_{(k_x>0),(k_y<0)}P(k_x, k_y)$. Directionality value 'D' in percentage is defined as D = (P1-P2)/(P1+P2). Here, D = 0 and 1 mean minimum and maximum preferential scatterings respectively.

Scattering from NW with different materials

We performed scattering simulations to explore the effect of the material of NW on scattering by changing the material to a dielectric (Zinc sulphide (ZnS)) and by making the NW as perfect electric conductor (PEC) and keeping other properties constant at 633 nm wavelength as shown in Figure 4.6. We found method to be robust for working with different materials. Directionality values (D) for preferential scattering of LG_0^{-1} beam calculated according to the procedure shown in Figure 4.5 are found to be 0.35 for ZnS and 0.40 for PEC NWs which are near to 0.38 for Ag NW.

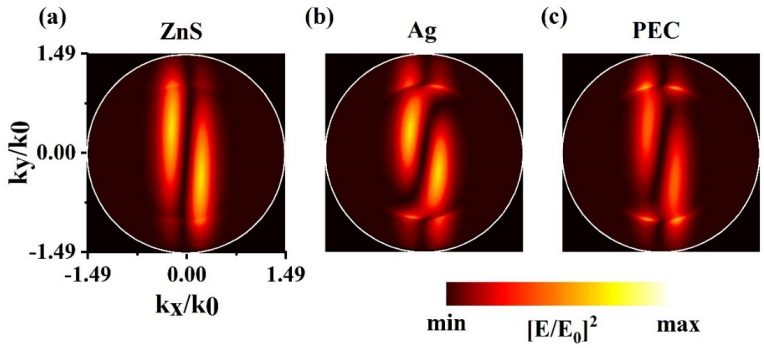

FIGURE 4.6: Simulated scattered Fourier plane images from NWs of different materials i.e., (a) Zinc sulphide (ZnS), (b) Ag and (c) perfect electric conductor (PEC) for LG_0^{-1} beam illumination (633 nm wavelength).

Thickness dependent scattering from NW

We tried to maximize the directionality value by changing the diameter of the NW. Figure 4.7 shows FP images for scattering with NWs ranging from 100nm to 500 nm in diameter. We calculated directionality value (D) for NWs with different diameter and found D = 0.29 (diameter = 100 nm), 0.30 (200 nm), 0.31 (300 nm), 0.38 (350 nm), 0.45 (400 nm) and 0.46 (500 nm) keeping other parameters constant. Directionality value increases with increase in diameter which can be attributed to the increase in the scattering cross-section with increase in NW diameter.

Effect of beam position relative to the short axis (y) of NW on far-field scattering pattern

Preferential scattering is sensitive to displacement of NW along its short axis and have maximum directionality value for parking of NW at the center of beam focus. Figure 4.8 shows scattering FP images for Ag NW movement in focus spot along its short axis (y-axis). Calculated directionality value (D) changes as D = 0.21 (y = -200 nm), 0.35 (y = -100 nm), 0.38 (y = 0), 0.32 (y = 100 nm) and 0.18 (y = 200 nm) for different NW positions.

Scattering from NW with different cross sections

We have performed simulation with NWs having circular, triangular and square cross sections with same diameter (350 nm) as of pentagonal NW used in this study and

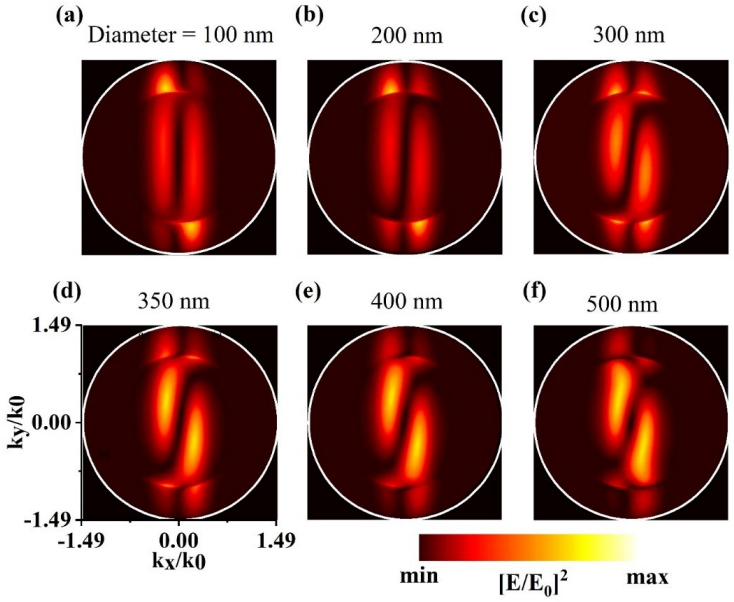

FIGURE 4.7: (a)-(f) show scattered FP images of LG_0^{-1} beam for NWs with different diameters ranging from 100 nm to 500 nm.

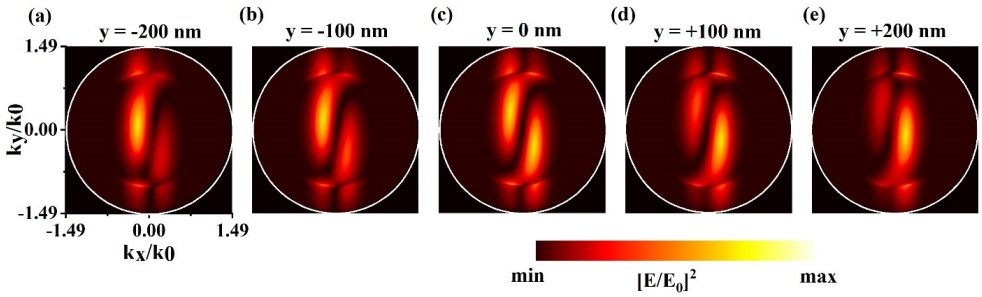

FIGURE 4.8: (a)-(e) FP images showing variations in the scattered farfield patterns of LG_0^{-1} beam as a function of movement along short axis (y) of NW relative to beam position. Here NW is at the center of beam for y = 0.

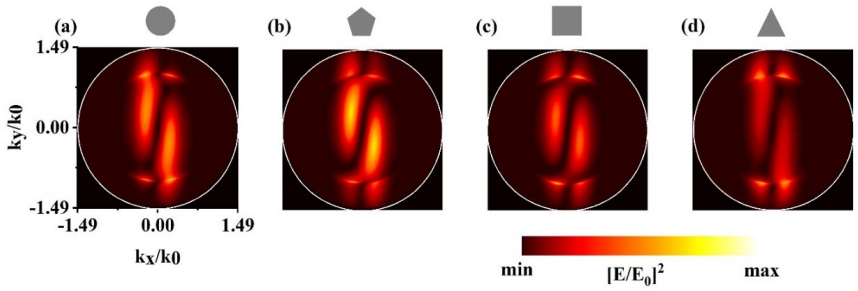

FIGURE 4.9: Fourier plane images showing scattering of LG_0^{-1} beam (633 nm wavelength) from plasmonic NW of 350 nm diameter with cross sections as (a) circular, (b) pentagonal, (c) square and (d) triangle.

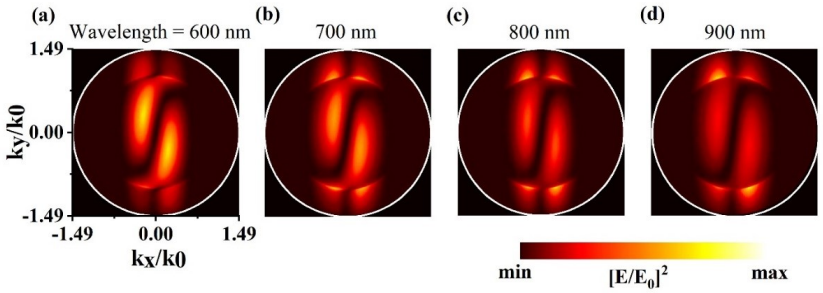

FIGURE 4.10: OAM induced preferential scattering in scattered farfield as a function of operational wavelength. (a)-(d) Fourier planes images showing scattering of LG_0^{-1} beam of wavelength 600 nm to 900 nm at an interval of 100 nm.

found that method works for all shapes as shown in Figure 4.9. Calculated directionality values are as follows D = 0.46(circular cross section), 0.38(pentagonal cross section), 0.26(square cross section) and 0.36(triangular cross section). Presence of OAM induced preferential scattering in scattered farfield from NWs with different cross sections makes the present method robust to be used for any one dimensional component of a photonic circuit irrespective of its shape.

Effect of operational wavelength on scattering from Ag NW

We simulated the scattering from an individual nanowire illuminated with different wavelengths (600 nm – 900 nm). The scattering FP images are shown in Figure 4.10. One can clearly see that FP patterns are very similar, qualitatively, to that of the experimental one (633 nm) and hence giving the information about OAM induced directionality. It should be noted that spot size and intensities for different wavelengths are not same and hence FP images give only qualitative idea about OAM induced preferential scattering.

4.4 Pattern recognition based OAM detection

4.4.1 Scattering patterns are sensitive to the mode number

Figure 4.11 (a-c) shows experimentally measured scattering FP images of LG_m^l beams as a function of varying mode number, l. Scattering FP image for l = -1 has two lobes (indicated by white dots) on both sides of k_y/k_0 axis with preferential scattering indicated by white arrows (Figure 4.11 (a)). The number of lobes increases with increment in the number of l in FP images. Figures 4.11 (b and c) shows that l = -2 and l = -3 have three and four lobes, respectively. This suggests number of lobes in FP image is equals to l+1 for a given OAM mode number l. It should be noted that preferential scattering direction for l = -2, -3 remains same as of l = -1 indicated by white arrows in respective figures. Increase in number of lobes with increase in mode number l can be understood from the fact that higher order vortex beams are unstable and split into l number of vortices as shown in insets of figure 4.11 (a-c) [126].

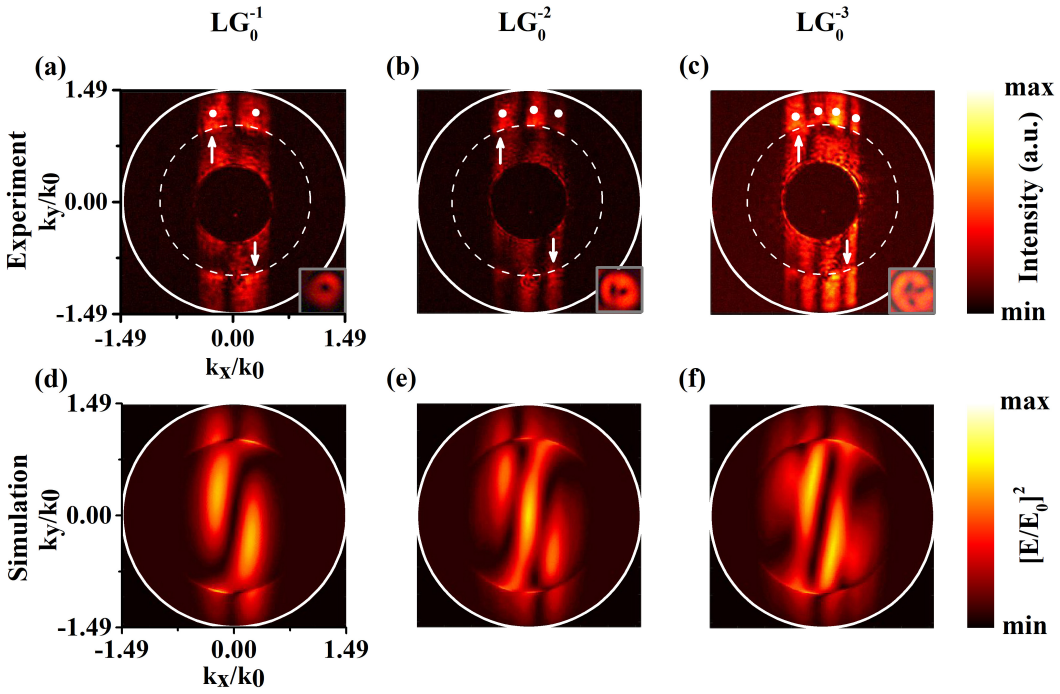

FIGURE 4.11: Fourier plane (FP) images showing dependence of scattering on the mangitude of OAM. Experimentally measured FP images show unique scattering pattern for (a) l = -1, (b) l = -2 and (c) l = -3. Number of lobes in the scattering pattern along k_y/k_0 axis increases with increase in OAM mode number l. Number of lobes is indicated by white dots. Insets in figures (a)-(c) show splitting of vortex in l number of vortices in real plane image with no NW in the focal regime. (d) - (f) Simulated FP images corroborating experimental results.

As explained in Figure 4.3, single dark region (singularity) at the center of beam causes absence of wave vectors along k_y/k_0 axis near $k_x/k_0 = 0$ resulting into two lobes in FP image. The cases of l = -2 and -3 modes will contain two and three dark regions inside the beam, respectively. This means vortex with l = -2 mode interacts with nanowire with three bright points (points with nonzero intensity) and hence scattering from these three points results in three lobes in FP image. Similar explanation holds for l = -3 mode and l = +1, +2, +3 modes (data not shown). It should be noted that the input power for different modes are not the same. As the mode number increases, the power density of the scattered light decreases. Input power for the scattering of different modes of OAM shown in Figure 4.11 are 8 nW (LG_0^{-1}), 66 nW (LG_0^{-2}) and 780 nW (LG_0^{-3}). Numerically simulated FP images (Figures 4.11 (d-f)) show similar pattern for l = -1 (Figure 4.11 (d)), l = -2 (Figure 4.11 (e)) and l = -3 (Figure 4.11 (f)) and hence corroborate experimental findings. Increase in width of the scattered pattern along k_x/k_0 for higher mode numbers can be accounted for increase in divergence of higher order vortex [127]. This procedure becomes more useful for higher order modes of OAM as splitting of vortex at focus plane is not distinguishable as shown in magnified real plane images in Figure 4.12. In this case far-field scattering pattern provides clear distinction in the higher OAM modes as shown for l =-4 to -7 in Figure 4.13.

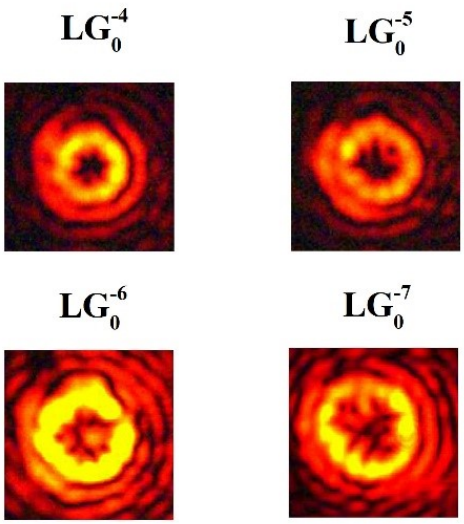

FIGURE 4.12: Magnified images of higher order vortex beams at the glass substrate without wire in the focal spot

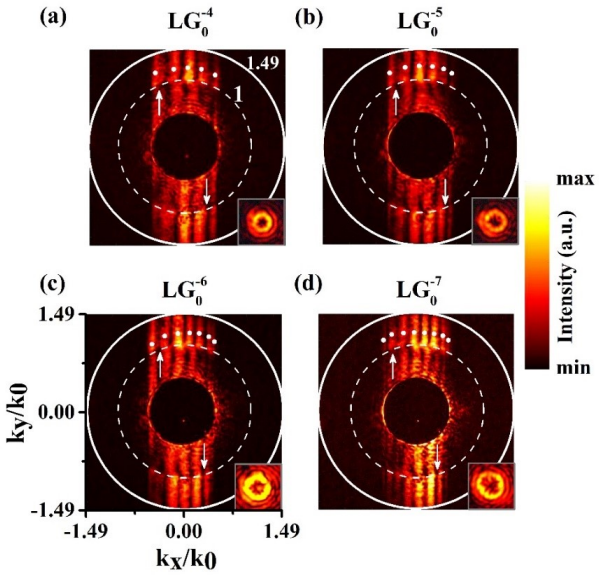

FIGURE 4.13: (a) – (d) show FP images for illumination of wire with LG beams having topological charge -4, -5, -6 and -7 respectively.

4.4.2 Scattering patterns are sensitive to sign of the topological charge

Vortex beams have positive or negative value of OAM. So it is crucial to identify the sign of particular mode number of OAM along with its magnitude. Figure 4.14 (a and b) show FP images of scattering for LG beam with $l = +1$ and $l = -1$ with same illumination power (8 nW). As indicated by white arrows in experimentally measured FP images, it is evident that preferential scattering inverts its direction as sign of OAM changes from $l = +1$ to -1. This is consistent with higher order OAM modes also (See Figure 4.15). Change in the direction of preferential scattering can be understood from the fact that as sign of OAM changes, the Poynting vector direction inverts which guides scattering wave vectors accordingly [123]. Asymmetric distribution in scattering FP image for different signs of a particular OAM mode is well corroborated by numerical simulations (Figure 4.14 (c-d)).

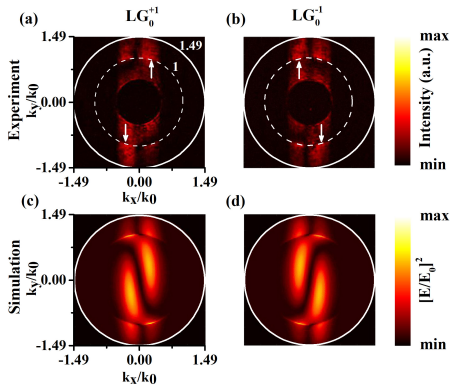

FIGURE 4.14: Discriminating the sign of topological charge. Scattering FP images of LG Beam (a) l = +1 and (b) l = -1 from plasmonic nanowire discriminating between sign of OAM mode l = |1|. (c) - (d) Simulated scattering FP images corroborating experimental results.

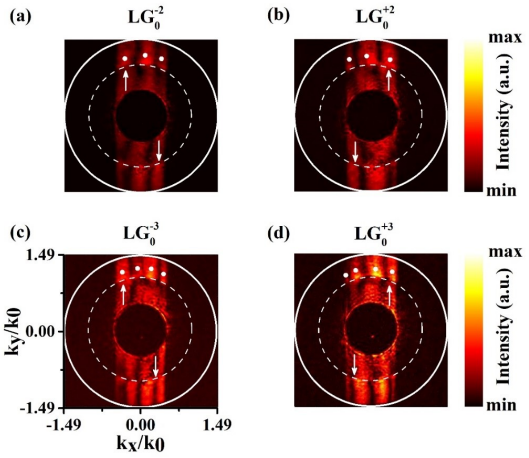

FIGURE 4.15: Scattering FP images of LG Beam (a) l = -2, (b) l = +2, (c) l = -3, and (d) l = +3 from plasmonic nanowire discriminating between sign of OAM mode l = |2| and |3|.

4.5 Conclusion

To conclude, we have experimentally shown that coherent light scattering pattern from a chemically prepared plasmonic nanowire, self-assembled on a glass substrate can be utilized to read-out the magnitude and sign of the topological charge of an optical vortex beam. A clear distinction between vortex beam scattering patterns and other beams that do not carry orbital angular momentum was established, which was further corroborated by three dimensional numerical simulations. Our work introduces a platform for OAM characteristics read-out at the chip-scale. By further combining techniques based on pattern recognition and machine learning, one can possibly automate the read-out procedure without human intervention. Such methodologies are of high interest in

optical communication channels, and the fact that we use a simple, chemically synthesized plasmonic nanowire structures may bring down the cost of such devices for future developments.

Chapter 5

Transverse orbital momentum flow controlled surface plasmon polaritons generation in a plasmonic nanowire

The chapter explores the effect of transverse orbital momentum flow on surface plasmon generation in a silver nanowire. We have experimentally shown how the sign and magnitude of the topological charge of orbital angular momentum carrying beams affect surface plasmon polaritons (SPP) generation in an individual plasmonic NW. We further corroborate experimental results with numerical simulations.

5.1 Introduction

Plasmonic nanostructures provide sub-wavelength confinement and guiding of light [39]. These effects are possible because of the presence of sea of free electrons in metals and large surface to volume ratio for nanostructures, which ensure maximum interaction of free electrons with a incident light beam on the nanostructure. When a light beam interacts with a plasmonic nanostructure having dimensions comparable to its wavelength, such as a nanoparticle, it creates localized oscillations of free electrons on the surface of the nanostructure. Quantum of these oscillations is called localized surface plasmon polariton. If a plasmonic nanostructure is extended in one or two dimensions such as nanowire (NW) or film, electromagnetic waves coupled with free electrons on the surface propagates along the extended dimension. These waves at the metal-dielectric interface are known as propagating surface plasmon polaritons (SPP).

Enhanced near field electric field in the vicinity of a nanostructure has been utilized to enhance weak molecular signals such as Raman scattering [128], local heat generation [129] and more. On the other hand, SPP in extended nanostructures have made waveguiding of light possible at the sub-diffraction scale, which can further be utilized in chip-based plasmonic circuits [130].

Silver nanowires are one of such plasmonic geometries that confines light in one dimension and propagates it in another dimension in the form of SPP [131, 132]. As described in chapter 1, SPP have momentum larger than free-space photons. Hence launching SPP in a nanostructure is possible only in circumstances where missing momentum is provided to the incident light beam. The momentum matching condition for SPP generation can be expressed using the following expression

$$\vec{k}_{SPP} = \vec{k}_{photon} + \vec{G} \tag{5.1}$$

Where, $\vec{k}_{SPP}$ is wavevector of SPP and $\vec{k}_{photon}$ is wavevector of the incident beam. $\vec{G}$ is extra momentum required for SPP generation. In the case of a plasmonic NW, SPP can be generated by exciting NW at its one of the extremities where symmetry breaking provides extra momentum for SPP generation. It is known that the efficiency of the generation of SPP in NW can be controlled using different parameters such as wavelength and polarization of light beam, the numerical aperture of the focusing lens, and morphology of the NW [132].

In this chapter, we discuss the effect of transverse orbital momentum flow on the efficiency of SPP generation in a silver NW. As discussed in chapter 1, beams with helical phase fronts carry orbital angular momentum (OAM), which can have both positive and negative signs as well as variable magnitude depending on the spatial phase profile of the beam. Helical phase front of OAM carrying beams results in a linear momentum component in the transverse plane along azimuthal coordinate. As discussed in chapter 1, the magnitude and sign of the azimuthal component of linear momentum (transverse orbital energy/momentum flow) are proportional to the topological charge of the OAM carrying beam.

We have utilized the transverse orbital momentum flow to control the efficiency of SPP generation in a silver NW. We experimentally show either change in sign of topological charge or change in position of NW's extremity on two sides of the singularity of the vortex beam enhances or reduces SPP generation depending on the direction of transverse orbital momentum flow. Change in the magnitude of the topological charge systematically changes the efficiency of OAM generation in the NW. We further demonstrate OAM controlled SPP generation in systems like NW coupled to the nanoparticle (NP), and how kink NW can behave like an optical switch. We provide finite element based simulations to qualitatively understand the effect of transverse orbital momentum flow on SPP generation.

5.2 Hypothesis

As discussed in chapter 1, Laguerre Gaussian (LG) beams have transverse orbital momentum flow. We hypothesize that this transverse orbital momentum flow should have implications on SPP coupling in the NW, as explained in figure 5.1. For NW placed in the focus of LG beam at 'position 1', orbital momentum flow should favor the SPP coupling for topological charge values with a positive sign ($+l$) and should oppose for the topological charge values with a negative sign ($-l$). The effect will reverse for the placement of NW at 'position 2'. Essentially momentum matching condition given by equation 5.1 for SPP should be changed to

$$\vec{k}_{SPP} = \vec{k}_{photon} + \vec{G}' \tag{5.2}$$

with $\vec{G}' = \vec{G} \pm \vec{P}_\phi$. Where, $\vec{P}_\phi$ is linear momentum component along azimuthal direction representing transverse orbital momentum flow. Signs $\pm$ is decided by the placement of NW at different positions in the focus of the LG beam as well as sign of the topological charge. For example, for $+l$ values and NW placed at 'position 1' the sign will be $+$ (favoring coupling) and will be $-$ (Opposing coupling) for $-l$ values for the same position. Situation will reverse for 'position 2'. For the case, where the transverse orbital momentum flow is opposing the SPP generation and $\vec{P}_\phi$ is equal to $\vec{G}$, there should not be any coupling of light to the NW even with satisfying other requirements such as polarization and high NA focusing.

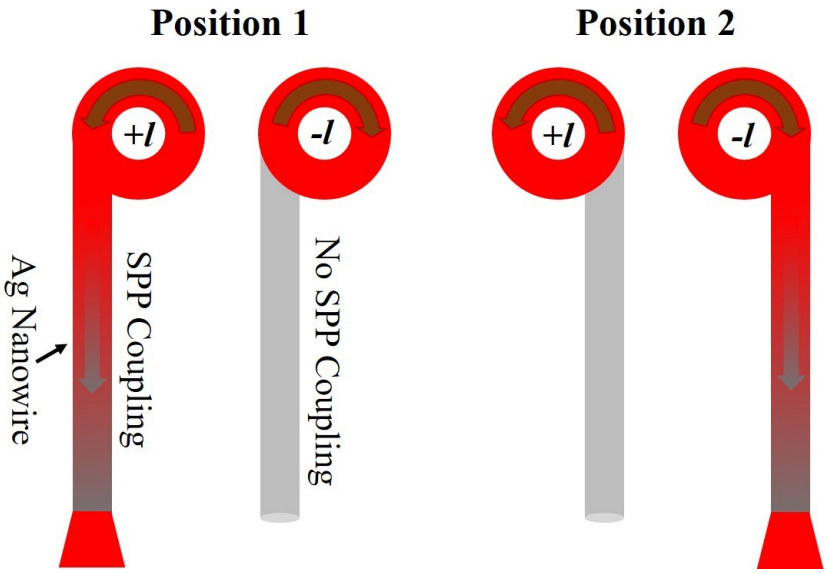

FIGURE 5.1: Schematic depicting hypothesis for the effect of transverse orbital momentum flow on SPP generation in plasmonic NW. NW is placed in two configurations as indicated by position 1 and position 2 for varying sign of topological charge.

5.3 Experimental observations

Ethanol solution containing Ag NWs was drop casted on to a glass substrate and was left to dry. We selectively excited one of such NWs with linear polarized (polarized along NW's long axis) LG beam (633 nm wavelength) with varying topological charge (l) using a high numerical aperture lens (1.49 NA, 100X). LG beams were prepared using a spatial light modulator operating in off-axis hologram configuration, as discussed in chapter 2. The extremity of the NW was scanned across the LG beam focus and SPP coupling in the NW was analyzed in backscattering geometry (a complete experimental setup is shown in figure 2.8, chapter 2) for two positions mentioned as 'position 1' and 'position 2' in figure 5.1. Figure 5.2 (a) shows a bright-field optical image of an Ag NW with a diameter $\sim$350 nm used for measurements of the effect of transverse orbital momentum flow on SPP coupling. The NW is excited by an LG beam with $l = \pm 7$. Figure 5.2 (b) shows that SPP coupling is maximum for $l = +7$ and is less for $l = -7$ for the placement of NW at 'position 1'. The situation is reversed for 'position 2'. Results are in agreement with our hypothesis, and hence, it shows that transverse orbital momentum flow affects the SPP coupling in the NW. To confirm it again, we perform topological charge dependence of SPP coupling in following section.

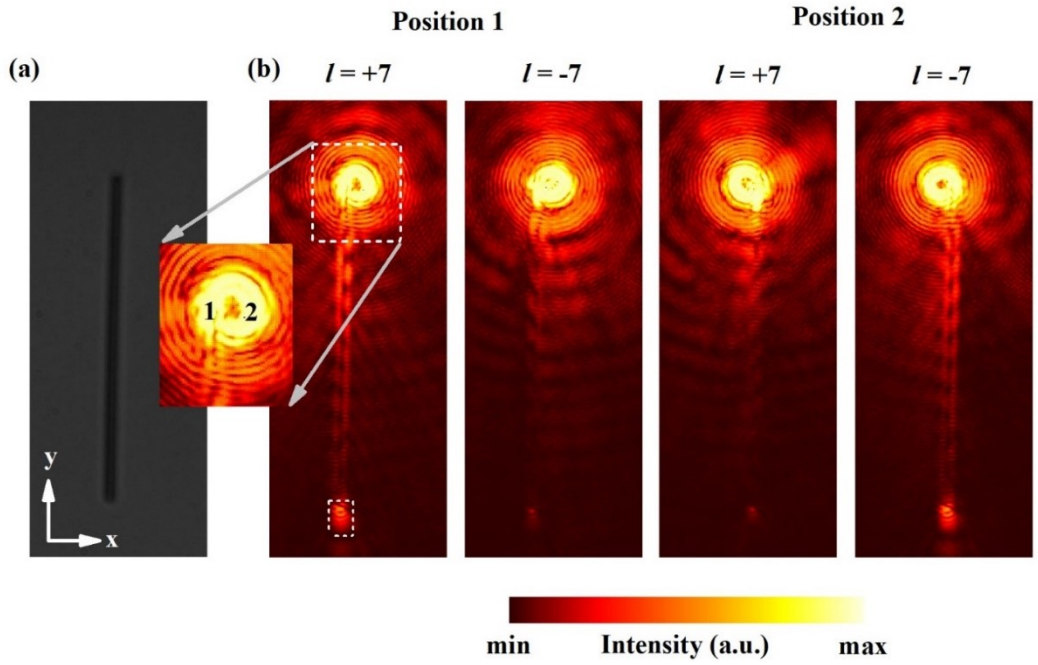

FIGURE 5.2: (a) Bright field optical image of the Ag NW utilized for understanding of the effect of transverse orbital momentum flow on the SPP generation in the NW. (b) and (c) Experimental observations of SPP coupling for varying position of NW in the focus and sign of topological charge for LG beam excitation with $l = \pm 7$.

Systematic control of SPP coupling using the magnitude of topological charge: Azimuthal component of linear momentum (P_ϕ) of LG beam is proportional to its topological charge, and hence the magnitude of transverse orbital momentum flow increases with an increase in the magnitude of topological charge [15]. To again confirm our hypothesis expressed in equation 5.2, we performed SPP coupling measurements with the varying magnitude of topological charge (l). According to the hypothesis, for $+$ sign in equation 5.2, the coupling of SPP should increase with the increase in the magnitude of l, and the effect should be reversed for $-$ sign in equation 5.2. Figure 5.3 shows experimental observations for SPP coupling for LG beam excitation with (a) $l = +1$, (b) $l = +4$ and (c) $l = +7$. It is clear from images that the difference between the intensities of light out-coupled at the distal end of the NW for 'position 1' and 'position 2' increases for an increase in the magnitude of l value. It should be noted that input power at the back aperture of the excitation objective lens was approximately the same for beams with different l values. Hence power density is not same for all beams at the focus because focus size increases with an increase in the magnitude of l.

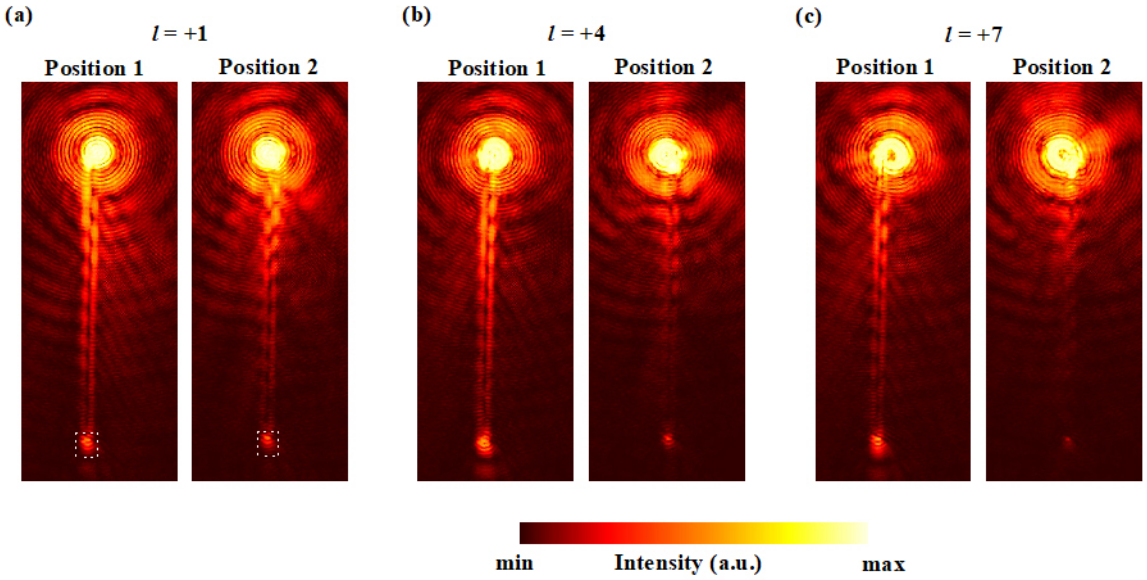

FIGURE 5.3: (a) Bright field optical image of the Ag NW utilized for understanding of the effect of transverse orbital momentum flow on the SPP generation in the NW. (b) and (c) Experimental observations of SPP coupling for varying position of NW in the focus and sign of topological charge for LG beam excitation with $l = \pm 7$.

Hence to have a quantitative understating of the effect of transverse orbital flow on SPP coupling as a function of the magnitude of topological charge, we have measured the ratio of out coupled light at the distal end for two positions of the NW for every l value. The ratio can be defined as

$$R = \frac{Out\ coupled\ light\ intensity\ counts\ at\ distal\ end\ for\ 'position\ 1'\ excitation}{Out\ coupled\ light\ intensity\ counts\ at\ distal\ end\ for\ 'position\ 2'\ excitation} \tag{5.3}$$

Intensity counts were measured in the area denoted by white box at the distal end of the NW for different positions to calculate the ratio, R. As expected from hypothesis, we found R to be in increasing order with an increase in the magnitude of l value. Measured ratios, R are 1.51, 3.82 and 6.67 for $l = +1$, $l = +4$ and $l = +7$ respectively for the observations shown in figure 5.3. Similar measurements performed on number of nanowires yielded similar trends in the value of R as l value was changed. The magnitude of R is also sensitive to error in positioning of the NW.

As explained in equation 1.5, chapter 1, the azimuthal component of linear momentum, $P_\phi \propto \frac{l}{r}$. We have calculated P_ϕ at the focus by measuring the radius of the vortex beam (r) (distance between the vortex center and nanowire axis) in the experimentally captured images. We have got P_ϕ value as 0.1, 0.27 and 0.37 units for $l = +1$, $l = +4$

and $l = +7$ respectively. This again supports that an increase in topological charge (l) increases P_ϕ and hence the R values. But we should note that we have used a high numerical aperture lens to focus the beam at the extremity of the nanowire where fields differ drastically from beam propagating in the free space. Hence dependency of P_ϕ on $\frac{l}{r}$ ratio may not be the same in tight focusing conditions as of free space. For a better understanding of this, we plan to perform rigorous simulations.

5.4 Simulation results

We performed finite element based simulations to qualitatively understand the effect of transverse orbital momentum flow on SPP generation in a plasmonic NW. A pentagonal cross-section Ag NW with 350 nm in diameter and 5 μm in length was placed on a glass substrate. Refractive index of the Ag was taken from [124]. One of the extremities of the NW was excited with the LG beam (633 nm wavelength, $l = \pm 4$) through the glass substrate. Beam waist (= wavelength (633 nm)) of the beam was maintained at the glass-air interface to focus the beam that provides a focus of $\sim$1270 nm (twice of the beam waist).

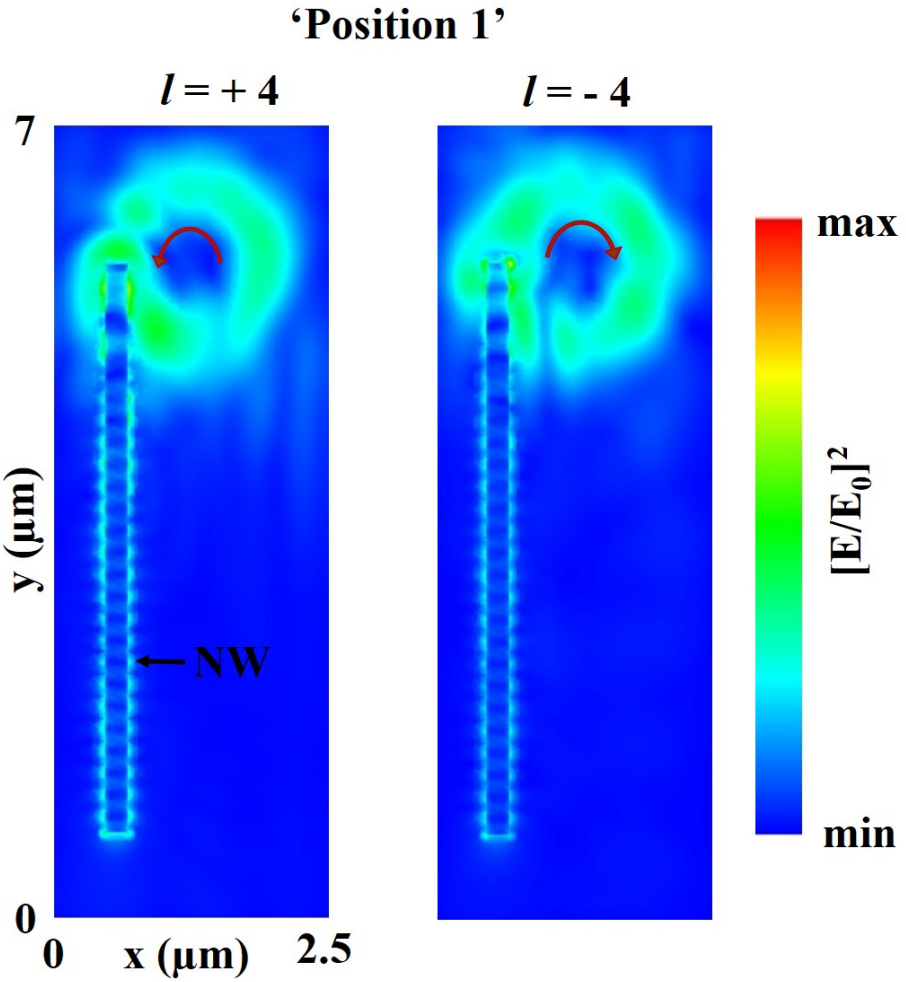

FIGURE 5.4: Simulated images showing the effect of transverse orbital momentum flow on the efficiency of SPP coupling in silver NW for 'position 1' with LG beam excitation ($l = \pm 4$). Red arrows show transverse orbital momentum flow direction.

Now NW end is placed under the beam focus at 'position 1' according to experimental observations. Figure 5.4 shows the coupling of SPP for the NW placed at 'position 1' with the LG beam excitation. The figure shows that the coupling efficiency of SPP in NW is less for LG beam with $l = -4$ compared to $l = +4$ for 'position 1' and hence showing similar trend as of experiments. Simulations are performed in weak focusing, and hence the efficiency of SPP coupling to NW is also small, which further makes the difference between the SPP coupling for $l = -4$ and $+4$ excitations small. These simulations provide only a qualitative understanding of transverse orbital momentum flow controlled SPPs. Simulations to exactly mimic the tight focusing conditions of experimental observations are under study. In that case, we will introduce lens specification to have tight focusing and a quantitative analysis of SPP coupling in NW as a function of the magnitude of topological charge should be possible.

5.5 OAM controlled optical switch

Control of light propagation on a photonic circuit is one of the important challenges in nanophotonics based devices. Different parameters, such as the polarization of input light [133], the position of a scatterer [134] have been utilized to control the propagation direction of light on a photonic circuit. The transverse orbital flow of OAM carrying beams can also serve the purpose of directing light in a particular direction [38]. Here, we show that OAM can control the direction of SPP in systems such as nanowire-nanoparticle (NP) junction and kinked nanowires. Figure 5.5 shows FESEM images of Au NP attached to Ag NW and kinked Ag NW systems. Ag NW-Au NP system was created by the self-assembly process. We drop casted Ag NWs on a glass substrate and after drying of the sample, Au NPs were drop casted on the same glass substrate. This process resulted in the NW-NP junction shown in figure 5.5 (a) based on capillary action [135]. On the other hand, kink NWs were formed by sonication of NWs solution for a few seconds.

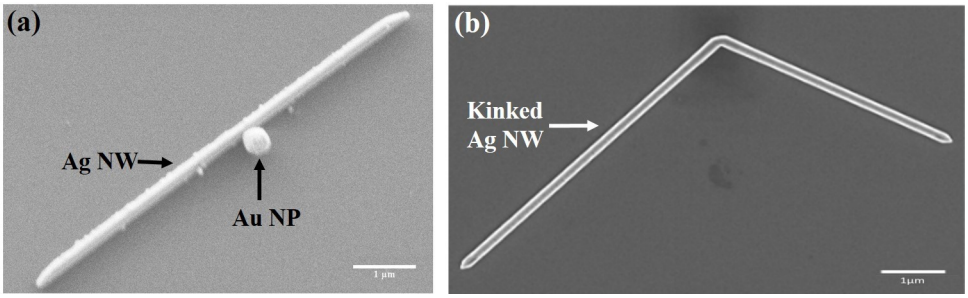

FIGURE 5.5: FESEM images of (a) Au NP coupled with Ag NW (b) kink Ag NW.

In these systems, excitation of the NW-NP junction or junction of two arms of the kink NW can launch SPP in two directions. These directions are towards two ends of the NW for NP coupled with the NW system and ends of two arms of the kink NW for other system. Our motivation is to selectively couple SPP in one particular direction with the help of transverse orbital momentum flow of LG beams. We place junction in the focus of the LG beam as shown in the bright-field optical image in figure 5.5 (a) for kink NW and in figure 5.5 (b) for NW-NP coupled system.

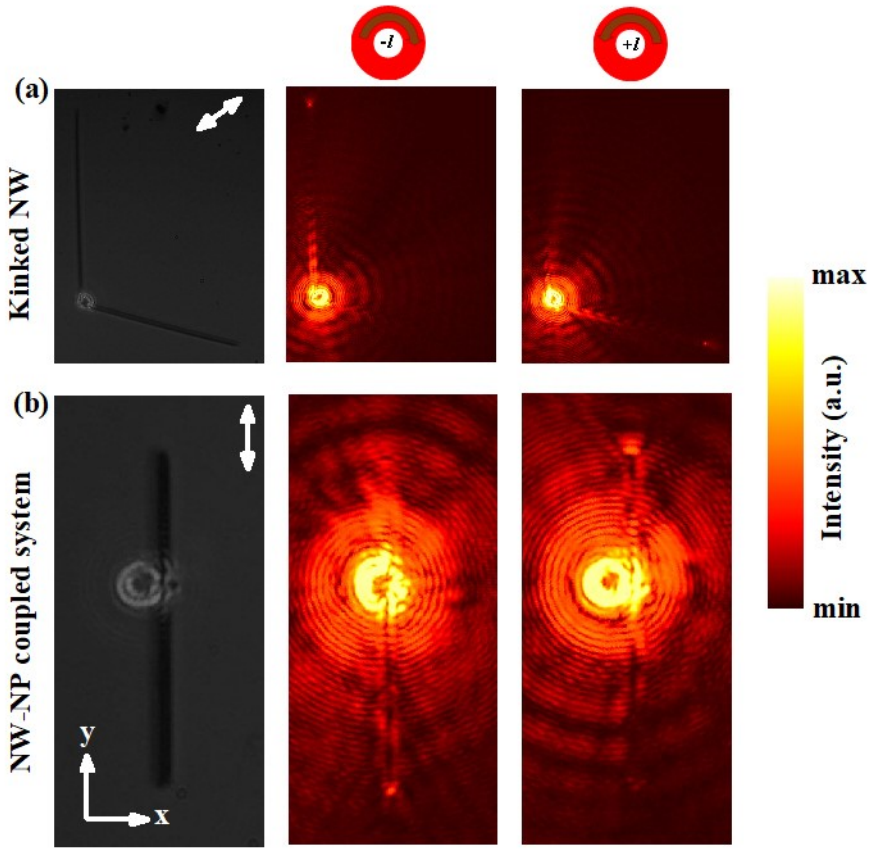

FIGURE 5.6: Selective excitation of SPP in different directions in (a) kink NW and (b) NW-NP coupled system using transverse orbital momentum flow in LG beams excitation with $l = \pm 7$.

For kink NW (figure 5.6 (a)), LG beam with $l = -7$ directs maximum light in the NW arm aligned along y axis and $l = +7$ light directs maximum light in other arm of the kink NW system. Coupling in different arms is favored because of the different direction of transverse orbital flow for two signs of the topological charge at the junction. For $l = -7$, transverse orbital flow direction supports SPP generation in arm aligned along the y-axis and suppresses the generation in other arm. The effect is reversed upon the change in sign of the topological charge. Figure 5.6 (b) shows the selective generation of SPPs in the different directions in the NW-NP coupled system using transverse orbital momentum flow. Polarization of the input light was kept such that it does not create bias in SPP generation in different directions. In this way, these systems, excited with OAM carrying beams, can behave like an optical switch.

5.6 Conclusion

We have experimentally shown that transverse orbital momentum flow of LG beams has implications on SPP generation in the plasmonic NW and hence should be considered in momentum matching condition for SPP generation. SPP coupling to the NW can be controlled by changing the magnitude and sign of the topological charge of the beam or placement of the NW in focus. Systems such as plasmonic kink NWs and plasmonic NW coupled with plasmonic NP can act as an optical switch when excited with OAM carrying beams. We have shown that change in the sign of the topological charge can direct light in different channels of these systems and hence will find application in plasmonic circuits. Numerical simulations also qualitatively corroborate experimental observations.

Chapter 6

Conclusions and Future Directions

In conclusion, the thesis focuses on understanding different aspects of the interaction of angular momentum (AM) carrying beams with a plasmonic nanowire (NW). We have explored the effect of spin momentum flow on the scattering of the light beam from a plasmonic NW. Far-field elastic scattering from a NW was utilized to detect different states of the orbital angular momentum (OAM) at the subwavelength scale. We have shown that the generation efficiency of surface plasmon polaritons (SPP) in plasmonic NW can be controlled using transverse orbital momentum flow of OAM carrying light beams. To realize the above phenomena experimentally, we have utilized a home-built dual-channel microscopy system. The microscopy system consists of Fourier plane imaging and spectroscopy capabilities and also includes spatial light modulator based generation of structured light beams. We have also utilized the microscopy setup to study the second-harmonic generation and two photon excited flourescence from organic mesowires. In this work, we study the excitation position-controlled directionality of the second harmonic generation from different facets of the mesowire.

Our study provides a fundamental understanding of the interaction of optical AM with one-dimensional plasmonic nanostructures and can potentially find application in chip-based plasmonic circuits in terms of detection of AM and controlling light propagation directions at diffraction limited scales. The developed home-built setup can be further integrated with high power AM carrying light beams and can be utilized to understand the effects of optical AM on nonlinear processes with the help of existing detection capabilities such as dispersion imaging and energy-momentum spectroscopy.

In the following, I summarize the different topics covered in the thesis and discuss future directions.

Spin momentum flow controlled far-field scattering of structured light from a plasmonic nanowire: Optical Spin-Hall effect

In chapter 3, we have explored the effect of spin momentum flow on the scattering of Gaussian and Hermite-Gaussian (HG) beams from an Ag NW. Captured far-field images of elastic scattering using the Fourier microscopy technique had circular polarization handedness dependent preferential/biased scattering. The preferential scattering was found to be more for the HG beam than for Gaussian beams. We understand the biasing in the scattering as an effect of spin momentum flow present in circularly polarized beams. Finite element based simulations also show spin momentum flow controlled biasing in the scattering and an enhancement factor of two for HG beams in comparison to the Gaussian beam.

Future direction:

In the present work, we study the scattering of circularly polarized light from 1D plasmonic nanostructure. It will be interesting to do polarimetry of the scattering of linearly polarized light from the NW. Analyzed scattered far-field patterns as a function of circular polarization may show accumulation of intensity with different handedness in opposite directions in the Fourier plane image. Another direction we intend to work is on the scattering of circularly polarized Laguerre Gaussian beams from NW, where we will have both SAM and OAM. These two AM can favor or oppose the scattering depending on their transverse momentum flow direction.

Discrimination of OAM states at subwavelength scale using a single NW:

In chapter 4, we have presented a far-field pattern recognition based method for discrimination of OAM states at the subwavelength scale. We have utilized Fourier plane imaging to capture far-field patterns in forward scattering configuration for Laguerre-Gaussian (LG) beam illumination of a single Ag NW. Change in the sign and magnitude of the topological charge of the LG beam produces a unique scattering pattern in the far-field. The method is found to be robust for the different parameters of light beams and NW, such as illumination wavelength, diameter of the NW, material of the NW, and

cross-section of the NW. We also provide finite element based simulation to support our detection method qualitatively.

Future direction:

There are two immediate directions to explore along similar lines. One of them would be to understand the phase structure of the scattered light. We would like to understand whether or not the scattered light has the signature of the phase structure associated with different states of the LG. Phase structure can be realized by interfering the scattered light with a reference beam introduced in the collection path of the microscope. Another direction is to explore the effect of OAM on the far-field scattering above the critical angle. In a Fourier plane image, light mapping to supercritical angles is a manifestation of the near field confined near the nanostructure. Hence studying the scattering at above-critical angle will provide information about the effect of OAM on localized plasmon generated on the NW. For this study, one needs to work at plasmon resonance of the NW along with its thickness for enhanced effects.

Transverse orbital momentum flow controlled surface plasmon generation in a plasmonic NW:

In chapter 5, we have discussed the effect of transverse orbital momentum flow on the efficiency of surface plasmon polaritons (SPP) generation in a plasmonic NW. SPP coupling in an Ag NW was measured for its placement on the two sides of the singularly of tightly-focused LG beam. We have shown that SPP coupling efficiency is either enhanced or reduced depending on whether the transverse orbital momentum flow is favoring or opposing the SPP momentum. Hence we propose for the modification in momentum matching condition for SPP generation in a NW. In the case of LG beam excitation, the azimuthal component of linear momentum resulted from the helical phase of the LG beams should be considered in the momentum matching condition for SPP generation. We have presented a detailed experimental study of the effect of magnitude and sign of transverse orbital momentum flow, and NW position in the focus on the efficiency of SPP generation in the NW. We discussed that the OAM beam generation of SPP in coupled NW-nanoparticle and kink NW plasmonic systems can behave as optical switches. We believe OAM can provide greater control on light propagation in a plasmonic-based circuit.

Future direction:

In the present study, we have provided finite element based simulation in weak focusing regime to qualitatively prove our hypothesis. But to quantitatively understand the effect of magnitude and exact placement of the NW in the focus on efficiency of SPP generation, we plan to tightly focus LG beam by introducing objective lens specification in simulations. Also in the present work, our focus was on the efficiency of SPP coupling. But the placement of the NW at different places of transverse orbital momentum flow should have implications on the SPP mode profile in the NW. We intend to study the effect of transverse orbital momentum flow on the mode profile of SPP in NW using Fourier plane imaging.

Appendix A

Directional second-harmonic generation controlled by sub-wavelength facets of an organic mesowire

In this appendix, we show how sub-wavelength facets of an organic molecular mesowire crystal can be utilized to systematically vary the directionality of second harmonic generation (SHG) in the forward scattering geometry. In addition to directional SHG from the mesowire, we experimentally observe optical waveguiding of the nonlinear two-photon excited fluorescence (TPEF). The appendix is an adaptation of the research article "Appl. Opt. 57, 5914-5922 (2018)"

A.1 Introduction

Localized manipulation and directional, linear and nonlinear emission of light at sub-wavelength scale is one of the important goals of nanophotonics. To this end, a variety of nanostructures made of plasmonic[119, 136–147] and dielectric objects[148–155] have been realized, thanks to advancement in nanofabrication methods including top-down and bottom-up approaches.

In recent times, nanophotonic operations of dielectric and semiconducting nanostructures have emerged as an exciting prospect in photonics[150, 156–159]. Given that ohmic loses in dielectric nanostructures[149, 152] are mitigated compared to plasmonic metals, they can be utilized in applications where Joule heating is detrimental. Certain dielectric and semiconducting nanostructures with high permittivity also facilitate multipolar Mie resonances [151, 156] that can be harnessed for developing nano-optical biosensing[157, 160], novel optical antennas[151, 161], and optimizing nonlinear frequency conversion[157, 162]. As inherent losses are minimized in such nanostructures,

they can sustain greater excitation powers, and hence provide an excellent opportunity to improve nonlinear optical processes such as second harmonic generation (SHG), third harmonic generation (THG), ultrafast optical switching, and many more [149, 150, 163–165].

An emerging prospect[149–152] in dielectric nanophotonics is to combine the unique properties of optical antennas with nonlinear optics. In this direction, interesting developments have occurred recently, such as: the observation of directional SHG and THG emission from silicon nanostructures [162, 166, 167]; efficient THG from germanium nano-disc [153]; nonlinear vector beam generation[168], SHG radiation pattern engineering [169], and polarization control[170] in Aluminum Gallium Arsenide (AlGaAs) nanoantenna; metal-dielectric hybrid nonlinear nano-antennas[171–177] and metasurfaces [178] with a specific directional emission.

A majority of the studies on dielectric nonlinear nanophotonics have utilized inorganic nanostructures such as silicon, germanium and AlGaAs. The general approach to prepare such structures is based on top-down nanofabrication either using high-power ultrafast lasers [148, 179] or electron beam lithography[168, 178]. Such top-down approaches generally result in polycrystalline nanomaterials, which can affect the yield of nonlinear optical processes. As a complementary approach, organic nanostructures can be prepared in single crystalline form using vapour phase methods, and can be potentially utilized for nonlinear optical antenna applications. Furthermore, organic molecular nanostructures have some advantages [180–184] such as low cost processing, flexibility of deposition on desired substrate, ultrafast and large nonlinear response, broadband spectral tunability by tailoring the structure of molecules and their arrangement in crystals.

In the context of nonlinear optical antennas based on dielectric nanostructures, there are two important aspects that have to be considered[169]: first is the efficiency of nonlinear optical frequency conversion, and the second is the directionality of the nonlinear radiation generated by the dielectric nanostructures. Over the years, a variety of organic crystals have been harnessed for efficient nonlinear optical frequency conversion, and crystalline organic nanostructures have been explored in the context of their nonlinear microscopy [185–187]. However a relatively unexplored aspect of organic nanostructure is their utility as nonlinear optical antennas, especially their directional nonlinear emission characteristics.

In this chapter, we show, how sub-wavelength facets of an organic molecular mesowire crystal made of diaminoanthraquinone (DAAQ) can be harnessed to actively control forward scattered SHG pattern. We test the ability of the mesowires with two and three facets to direct and vary the SHG signal, and find that the directionality of SHG can

be varied and switched over 130 degrees. This ability is mainly facilitated by the single crystalline nature of the utilized mesowire, and is a clear advantage over polycrystalline nanostructures made of inorganic dielectric materials. In addition to directional SHG emission, we show selective nonlinear waveguiding capability of our geometry. Specifically we show how for the same pump excitation, the SHG signal is directional and confined at a location in the mesowire, whereas the two-photon excited fluorescence (TPEF) emission is isotropic and delocalized. This observation has direct consequence on spatial engineering of two different kinds of nonlinear emission on a single mesowire.

A.2 Methods

A.2.1 Sample preparation

1, 5 diaminoanthraquinone (DAAQ) mesowires were prepared through physical vapour transport method. The detail procedure to synthesize these molecular waveguide can be found in previous reports[188]. In brief, DAAQ molecular powder (5mg, Sigma Aldrich, 85% pure) was dissolved in ethanol (60ml, Sigma Aldrich, 99% pure) in single neck round bottom (RB) flask. RB flask was then placed inside a heater cum rotor bath for depositing DAAQ molecular film around the RB wall. Continuous rotation at constant temperature (40°C) ensures the uniformity of molecular thin film around wall of the flask. Afterwards, a cleaned glass coverslip was suspended inside the flask through a glass bar attached on the top of flask. Subsequently, the whole arrangement was then placed inside the silicon oil bath and increased the temperature of the system up to 160°C-180°C for different growth durations. As the temperature of the flask elevates, the molecules evaporate from the wall and start condensing on the glass coverslip. These condensed molecules act as preferred nuclei sites for new incoming molecules. Subsequently, these molecules get self-aggregated (J-aggregation takes place for our system[188], confirmed in our previous study) and resulted as extended one dimensional nanostructures (Figure A.3(a)). The length and diameter of molecular waveguide can be easily controlled according to the growth duration and temperature. Deposition of wires was done on marked glass cover slip for the correlation between optical microscope image and field emission scanning electron microscope (FESEM) image of the wire to be studied. The optical absorption maxima of the grown mesowires was found to be around 520 nm (Figure A.1).

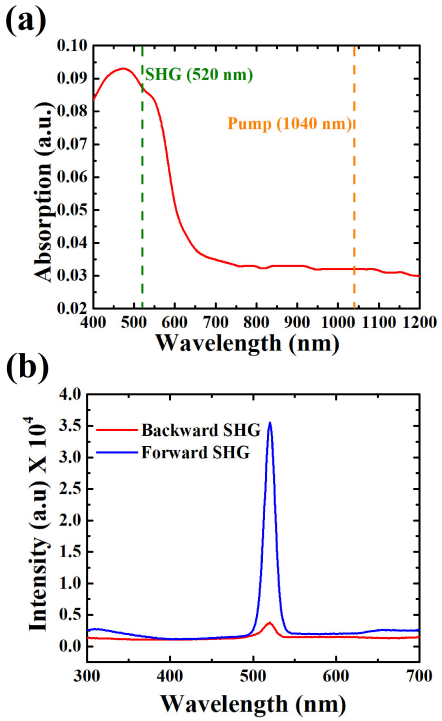

FIGURE A.1: Schematic of Experimental setup for Fourier plane imaging and spectroscopy measurement of SHG. L1, L2, L3, L4, L5 and L6 are lenses where L2 is tube lens, L3 is Bertrand lens and lens L4 is used to form a real plane image. M1 and M2 are mirrors. FM is flip mirror. HWP, LP and SPF represent half wave plate, linear polarizer and short pass filter respectively. BS is beam splitter. SPF was used to block the pump. In case of Fourier plane imaging of SHG and TPEF, extra short pass filter and edge filter were used, respectively.

A.2.2 SHG microscopy coupled with Fourier plane imaging

In a SHG microscope, the captured SHG intensity can be expressed as[186]:

$$I_{SHG} = |N \int_V \int_\Omega \int_{NA} E_{SHG}(r, \Omega, k) f(\Omega) dr d\Omega dk|^2 \tag{A.1}$$

where E_{SHG} is the electric field due of SHG signal, V is the focal volume from where the SHG is collected, Ω is the orientation of the molecules within the focal volume, k is the wavevector of the SHG signal, r is the spatial coordinate of the nonlinear dipole, $f(\Omega)$ is the orientation factor, and NA is the numerical aperture of the collecting objective lens. In our measurement, we collect the signal in the Fourier-plane of the objective lens, such that we do not integrate the signal over the whole NA, but retain the information of the in-plane k vector distribution. This k vector distribution can be represented by two polar angles (θ, ϕ), where θ represents the radial angle subtended

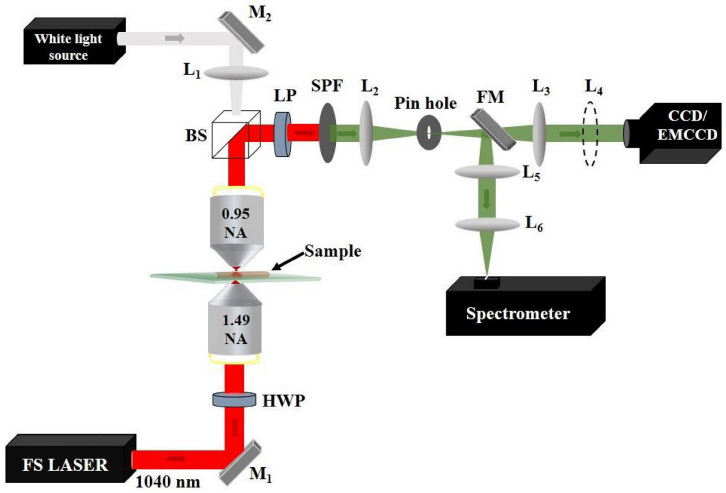

FIGURE A.2: Schematic of Experimental setup for Fourier plane imaging and spectroscopy measurement of SHG. L1, L2, L3, L4, L5 and L6 are lenses where L2 is tube lens, L3 is Bertrand lens and lens L4 is used to form a real plane image. M1 and M2 are mirrors. FM is flip mirror. HWP, LP and SPF represent half wave plate, linear polarizer and short pass filter respectively. BS is beam splitter. SPF was used to block the pump. In case of Fourier plane imaging of SHG and TPEF, extra short pass filter and edge filter were used, respectively.

by the numerical aperture of the lens, and ϕ represents the azimuthal angle. Figure A.2 shows the optical microscope used to study the optical nonlinear response of the DAAQ mesowires. The lower objective lens (high numerical objective lens, 1.49 NA, 100x) was used to excite the mesowire through the glass substrate using a Ti- sapphire laser (140 fs, 80 Hz, Chameleon from Coherent) operating at 1040 nm wavelength.

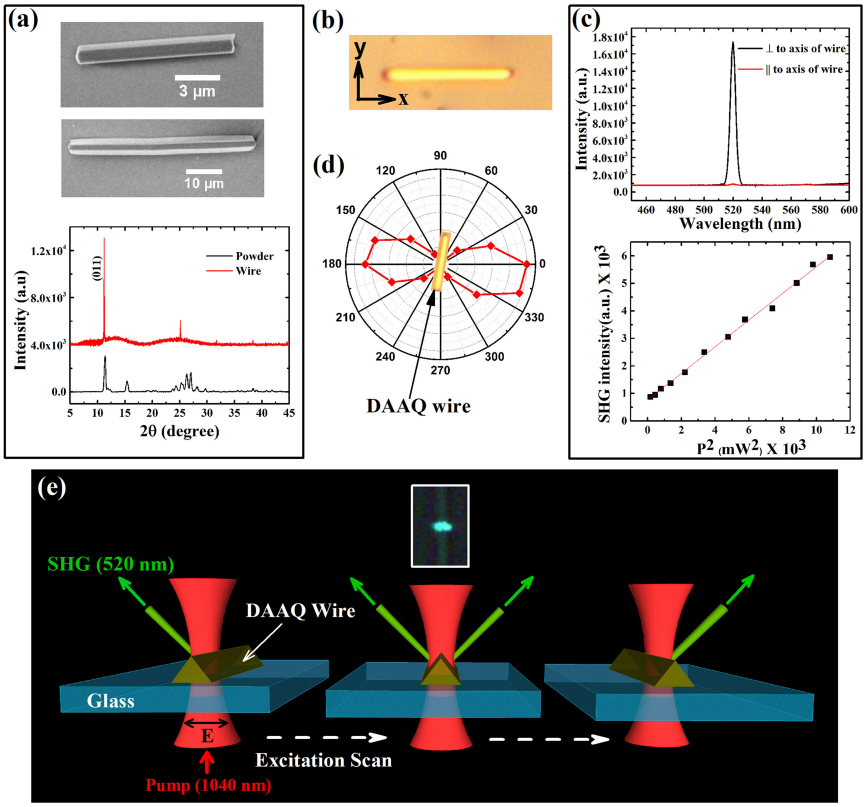

FIGURE A.3: (a) Representative FE-SEM images of faceted DAAQ mesowires. PXRD pattern for 1, 5 diaminoanthraquinone (DAAQ) mesowre on glass coverslip (red) and DAAQ powder(black). (b) Bright-field optical image of faceted DAAQ mesowire. The typical length is around 17 μm and width is 1.38 μm. (c) Forward-scattered SHG spectra from a DAAQ mesowire for excitation with pump polarization perpendicular and parallel to the long axis of wire (longitudinal). Pump excitation is 1040 nm (140 fs, 80 MHz). Power dependence of SHG signal: Peak intensity of the signal at 520 nm was measured as a function of pump power. (d) Variation of SHG as a function of angle of pump polarization. Maximum emission intensity is when excitation polarization is perpendicular to long axis of the mesowire. (e) Schematic of forward-scattered SHG wavevector variation as a function of position of 1040 nm focused pump beam across the width of the DAAQ mesowire. The inset shows a real plane image of SHG emission at 520 nm from DAAQ mesowire when excitation beam is parked at the center of the wire.

The focused spot size was measured to be $\sim$ 670 nm. Measurements are done at 17 mW average power (at the entrance of microscope objective lens). We observed that exposing the wire with 58 mW or more power, burns the structure. Piezo Nanopositioning Stage (P-733.3CD, Physik Instrumente (PI) GmbH & Co. KG) was used to scan the mesowire nm. Forward scattered signal was captured by the upper objective lens (0.95 NA, 100x). A pinhole was introduced in the real plane to spatially filter the signal from the point of excitation. For the Fourier plane imaging of the forward scattered optical

nonlinear signals, back focal plane (BFP) of the upper objective lens was imaged to an electron-magnified charge-coupled device (iXon Ultra, Andor) using the tube lens (L2) and a Bertrand lens (L3). The pump (1040 nm) was blocked by a Short pass filter in the collection path. For Fourier plane imaging of SH and TPEF signals, we introduced additional short-pass and edge filters. The pump polarization was varied using a half wave plate (HWP) in the excitation path. A linear polarizer (LP) was used to study the output polarization dependence of the SH signal. For different excitation position, the BFP image was captured at a step of 100 nm. A flip lens (L4) was used to capture the emission in real plane for each BFP image. For spectroscopic properties, the signal was sent to the transverse to its long axis over a diffraction limited excitation spot in the steps of 100 slit of the spectrometer using a flip mirror and was focused to spectrometer slit using lenses L5 and L6.

A.2.3 Numerical calculations

3D Finite Difference Time Domain (FDTD) simulations were performed at the pump wavelength (1040nm) by considering a triangular DAAQ waveguide resting on the glass substrate. Refractive indices (real and imaginary part) of DAAQ and glass were taken from [188] and [189] respectively. The DAAQ wire was approximated as an irregular triangular waveguide of length 10 μm with one of the angles as 40° and base length as 1.3 μm (see Figure A.4(a)). This was done to mimic the structure under study, as the wire clearly shows two facets in the top view (see SEM images in Figure A.4 (b)). The wire was illuminated using a Gaussian beam of wavelength 1040 nm through the glass substrate. The Gaussian beam was focussed at the glass-wire interface using a thin lens of NA 1.49.

The simulation area was meshed using the non-uniform conformal variant mesh of size 5nm to ensure accuracy and was terminated using Perfectly Matched Layers (PMLs) to reduce spurious reflections from boundaries. Near field electric field was calculated by positioning the Gaussian source at different positions along the axis perpendicular to the length of the wire.

A.3 Results and discussion

A.3.1 DAAQ mesowires exhibit multiple facets

Figure A.3 (a) shows field-emission scanning electron microscopy (FE-SEM) images of typical DAAQ mesowires used in this study. These mesowires are grown by vapour deposition method[188, 190, 191] on a glass coverslip, and results in crystalline meso

or nanowire [192]. The width of the wire can be controlled from meso- to nano-scale by varying the deposition time [192].

In order confirm crystallinity of the grown structure, we performed x-ray diffraction (XRD) on DAAQ mesowires deposited on a glass substrate (see XRD data in Figure A.3 (a)). The growth direction of mesowire was along [011] axis of the DAAQ crystal.

The elongated crystals exhibit monoclinic lattice with parameters a = 3.78 Å, b = 9.73 Å, c = 15.01 Å, β = 82.4° [192] and centrosymmetric space group $P2_1/C$ (no. 14)[193]. From the top-view (Figure A.3 (a)), most of the wires exhibit either two or three exposed facets. One of the main objectives of our work is to determine if the sub-wavelength facets of DAAQ mesowire can control the SHG radiation pattern.

A.3.2 SHG characteristics of DAAQ mesowires

A typical optical bright field image of a faceted DAAQ mesowire resting on a glass substrate is shown in Figure A.3 (b). Since the width of the wires are typically less than 2 microns, the facets cannot be resolved in optical microscopy images (Figure A.3 (b)). First, we studied the polarization resolved SHG spectra of DAAQ mesowires. By employing a forward-scattering nonlinear optical microscope (see methods section for details), we focused a 1040 nm femtosecond-laser pump beam at the center of the mesowire, and captured the SHG signal at 520 nm (after filtering out the TPEF signal) in the forward scattering geometry. In Figure A.3 (c), we resolve the SHG spectra with respect to polarization of the excitation laser beam. The nonlinear process is confirmed to be second order by measuring emission intensity as a function of input power (see Figure A.3 (c)). When the polarization of pump beam is perpendicular to the long axis of the mesowire, the SHG signal is maximum, whereas for the parallel configuration, the signal is minimum. In Figure A.3 (d), we show the pump-polarization dependent SHG emission from the DAAQ mesowire. Going by the arguments of Brasselet et al. [186], two inferences that we can draw from this observation are: a) the molecular dipoles of the mesowires are aligned perpendicular to the long axis of the wire; b) the distribution in orientation of the dipoles is narrow. We anticipated no contribution towards emission from the bulk of mesowire as DAAQ crystals used in this work have a center of symmetry. One of the important aspect of DAAQ mesowire is that maximum SHG is emitted in forward direction. Figure A.1 (b) shows SHG collected in forward (towards air) and backward (towards substrate) directions for a typical DAAQ mesowire. We have calculated the conversion efficiency (I_{SHG} / I_{Pump}, where I: Intensity) of SHG in forward direction and found it to be of the order of 10^{-9} for 20 mW pump power. Spectrometer is calibrated for pump power (1040 nm) by reducing the LASER power and sending it directly to the spectrometer. Efficiency is calculated by

taking the ratio of the counts of SHG in the spectrometer and counts corresponding to the pump power (20 mW) measured at the entrance of objective lens. We have corrected for the response of the spectrometer at SHG and pump wavelengths. It should be noted that calculations for efficiency do not correct for losses due to optical components.

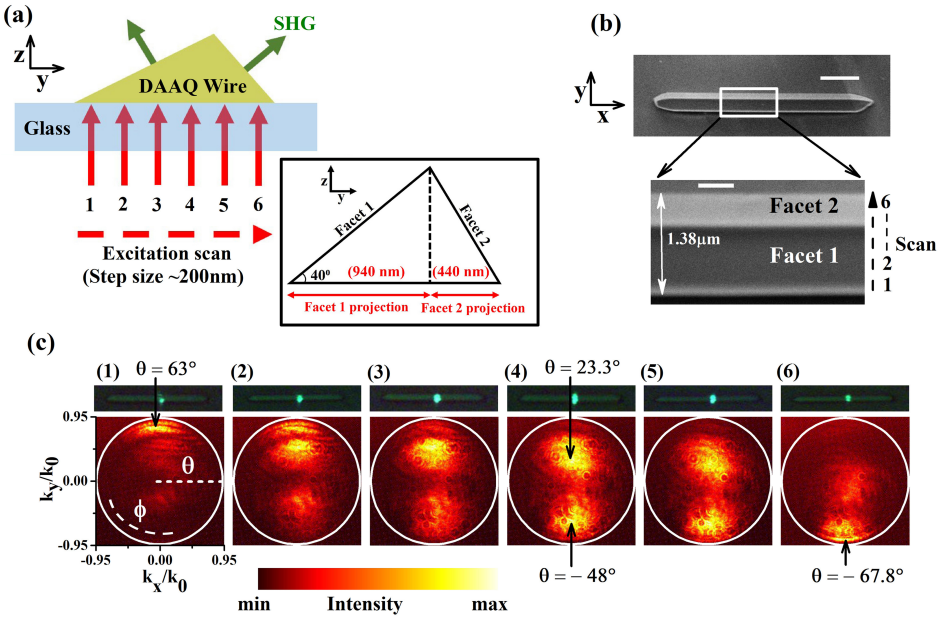

FIGURE A.4: (a) Schematic of the experiment in which the focused excitation position is varied across the width of a DAAQ mesowire with two facets facing the air superstrate. Tip of the red arrows 1 to 6 indicate the excitation spot. Green arrows indicate SH emission from facets of the wire. Inset shows that projections of facets on base have different widths which further indicate that one of the angles is less than 60°. This angle is assumed to be 40° for numerical calculations. (b) FESEM images of DAAQ mesowire of ∼16.5 μm length at two different magnifications. Scale bars are of length 3 μm (full-scale image) and 500 nm (zoomed in image) (c) SHG emission (real plane images) and corresponding wave vector distributions (Fourier-plane images) for excitation positions 1 to 6 shown in Figs. (a) and (b). θ is half angle of captured cone and has maximum value of 71.8° defined by numerical aperture (0.95) of objective lens. ϕ is azimuthal angle. Wavevector axes of Fourier-plane image are defined as $k_x/k_0=\sin\theta\cos\phi$ and $k_y/k_0=\sin\theta\sin\phi$.

A.3.3 Hypothesis and scheme of the experiment

Given that the mesowire have subwavelength facets, how do they influence the directionality of the forward SHG emission? This is the central question we ask, and Figure A.3 (e) shows the schematic of our experiments to address this question. Our hypothesis is that when we precisely scan the pump excitation (in steps of around 100 nm) across the width of the mesowire, we should be able to see a drastic change in the forward

SHG radiation pattern. This expectation is due to the presence of the facets on the crystal, which should influence the emission directionality. Importantly, we are interested to know if we can switch the directionality of the SHG emission when the pump beam was moved from one edge of the mesowire to another (see schematic in Figure A.3 (e)). In the inset of Figure A.3 (e), we show a typical real colour image of the SHG emission at 520 nm when the pump beam is focussed at the center of the mesowire. When the beam is laterally scanned across the width of the mesowire, we do observe spatial modulation of SHG emission as shown in real plane images of Figure A.4 (c). Having observed this modulation, our next goal is to quantify the angular intensity profile and correlate it to the morphology of the mesowire.

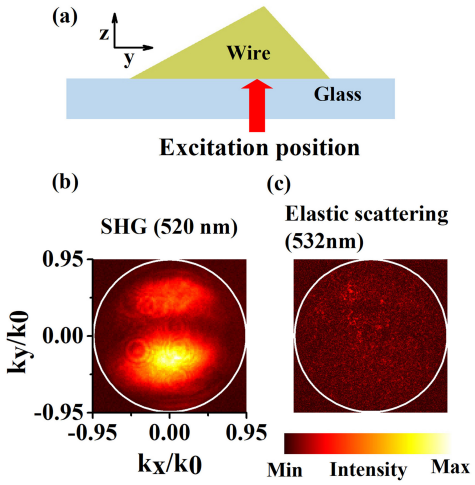

FIGURE A.5: Comparison of angular intensity distribution of SHG scattering (520 nm) and elastic scattering (532 nm) from the same DAAQ mesowire. (a) Schematic showing position of the pump beam (1040 nm for SHG scattering and 532 nm for elastic scattering) at the center of the mesowire. Fourier plane images captured for (b) SHG scattering and (c) elastic scattering reveals the difference in angular intensity distribution.

A.3.4 Variation of SHG wavevector from a DAAQ mesowire with two-facets

First, we begin by discussing the effect of varying the excitation position on the angular emission of the second-harmonic generated at the DAAQ mesowire. Figure A.4 (a) shows the schematic of the experiment performed, in which the SHG signal is captured by positioning the pump-beam at various locations across the width of the DAAQ mesowire. Positions 1 to 6 indicate the different locations of the focused pump beam (step size$\sim$200 nm). The SHG emission pattern is angularly resolved by a transmission mode Fourier microscope (see methods for the details on instrumentation). The DAAQ

mesowire that we used for the experiment is visualized by FE-SEM imaging at two different magnifications (Figure A.4 (b)).

In Figure A.4 (c) (top) we show a series of real-plane SHG images recorded from the mesowire for the six different locations of the laser spot. The numbers indicate various positions ($\sim$ 200 nm step size) of the excitation beam that result in SHG scattering. Figure A.4 (d) (bottom) represents the corresponding Fourier-plane image showing the angular distribution of SHG signal. Following are inferences that can be drawn from the experiment:

- By changing the position of excitation, the directionality of the SHG scattering wavevector can be varied. Figure A.4 (d) shows an angle of maximum intensity at θ = 63° for the excitation focus at one of the lateral edges of wire (position 1, Figure A.4 (b)). When the focus is moved to the other end of the lateral edge of the mesowire (position 6, Figure A.4 (a)) the angle of maximum intensity is at θ = -67.8°. This indicates a change of 130.8° in the SHG emission angle. We note that the maximum angle (71.8°) captured in our experiment is limited by the numerical aperture of the collection objective (0.95 in this case). This means there can be SHG emission beyond 71.8° which is not recorded in our measurements. At position 4, when the excitation is at the center of the mesowire, maximum SHG emission occurs at angles θ = 23° and θ = -48°.

- The directionality of the SHG scattering depends upon the inclination of the facets with respect to the excitation beam.

- For certain excitation positions (number 2 in Figure A.4 (c)), we observed interference fringes in the Fourier-plane image. This may be due to coherent superposition of the SHG waves emanating from dipoles at two different positions on the mesowire.

- Added to this, the grown mesowires have strong absorption at the wavelength of SHG emission (520 nm in this case). As a result, the angular distribution of the surface SHG scattered light (520 nm) drastically differs from elastic scattered light (532 nm) (Figure A.5). Interestingly, the wire behaves as an opaque object (width $\sim 3\lambda$) at 532 nm excitation close to the absorption maximum of DAAQ mesowire. Figure A.5 (b) shows minimally transmitted light (background speckles) through the wire. In contrast, the SHG scattered light at 520 nm shows facet-sensitive directional emission (Figure A.5 (a)). It should be noted that elastic scattering at 532 nm wavelength was performed using a line filter (for 532 nm wavelength) in the collection path of the microscope to filter out any secondary emission.

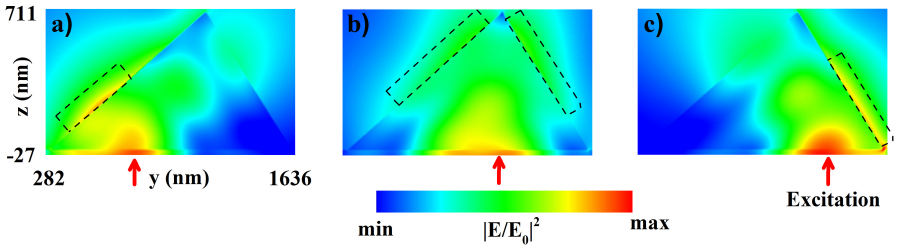

FIGURE A.6: FDTD simulations showing electric near-field distribution at excitation wavelength (1040nm) for various positions (a-c) along the cross-section of a two-facet mesowire geometry. The arrows indicate the position of Gaussian beam excitation. The dotted boxes indicate the region of maximum intensity at the facets of the mesowire

Also, we performed angle resolved forward SHG experiment on a DAAQ mesowire with three facets, and found systematic variation of SHG as we move the excitation beam across the width of the mesowire (Data not shown).

A.3.5 Parameters influencing the SHG wavevector

Having experimentally observed variation in the SHG radiation pattern as a function of excitation location, we are interested in understanding the relevant parameters that can be connected to our observations. From a theoretical basis on nonlinear microscopy, the SHG radiation patterns from a molecular assembly can be studied from at least two approaches. One is the phased dipole array approach [194–197] and the other is the Green′s tensor approach [198]. We adapt the former approach to understand basic elements of our results. In a SHG microscope, the far-field power per differential solid angle is given by:[194]

$$P_{2\omega}(\theta,\varphi) = \frac{1}{2} n_{2\omega}\epsilon_0 c r^2 |E_{2\omega}(\theta,\varphi)|^2; \tag{A.2}$$

where $n_{2\omega}$ is the refractive index of the mesowire at the SHG frequency, r is distance between the nonlinear dipole and the detector, $E_{2\omega}(\theta,\varphi)$ is the electric field of the SHG. This field can be further expressed as:[194]

$$E_{2\omega}(\theta,\varphi) = E^{(0)}_{2\omega}(\theta,\varphi)\cdot N \cdot A(\theta,\varphi). \tag{A.3}$$

The $E^{(0)}_{2\omega}(\theta,\varphi)$ represents the dipolar electric field emission at the focal center of the illumination, N represents the total number of molecules in the focal volume contributing to the SHG signal i.e. molecules present on the facet of the wire, and $A(\theta,\varphi)$ is a scalar function representing the angular modulation, and is dependent on the waist of

the excitation beam and the Gouy phase shift at the point of excitation [194]. Equation (3) suggests that far field distribution depends on the dipole orientation. Also when we move our focused excitation along the base of the mesowire, both N and A (dependent on the geometry of the structure) vary, which leads to variation in the detected SHG radiation pattern. We note that apart from the general parameters discussed above, the cross-section geometry also plays a vital role in our observations. Especially, the orientation of the facets with respect to the excitation beam will influence the SHG pattern, which is discussed below.

A.3.6 Near-field excitation profile highlights the role of the facets

To further understand the change in the wave vector distribution of SH emission as a function of excitation scan, we simulate the pump field distribution for different lateral positions of excitation. Full-wave Finite Difference Time Domain (FDTD) calculations are performed to visualize pump-field distribution at the upper two facets of DAAQ mesowire (see methods section for details on simulation). The real and imaginary parts of the refractive index of the mesowire used in the simulations are extracted from past measurements [188]. The maximum value of the near-field distribution of the pump-field (1040 nm) changes as we change the position of excitations in the geometry (see dotted boxes in Figure A.6 (a to c)). Since the orientation of the facets changes as we proceed from right to left in the geometry (Figure A.6), the location of the nonlinear dipole excitation and emission will vary accordingly. What essentially is transferred to far-field is the emission from the contributing nonlinear dipole at the facets. The directionality of the light in far-field now depends on which facet dominantly contributes towards the nonlinear emission. A conclusion that we can draw from this result is that by changing the excitation position one can selectively excite specific dipoles in the geometry, which further contributes towards directional SHG signal emanating from the object. Although FESEM images (Figure A.3 (a) and Figure A.4 (b)) show a smooth surface of DAAQ mesowires, there may be some fine structural details that are not detectable at the given resolution of electron microscope. These structures can potentially influence electric near-field of pump LASER and may further affect SHG from facets of the mesowire. It is to be noted that for the simulations, we have not considered such fine structural details of the wire. The experiments and simulations indicate that by varying the position of the excitation-pump in a nonlinear microscope, one can alter the transmitted SHG wavevector. Such capability to precisely tune the directionality of SHG has direct implications on nonlinear optical antennas, where the directionality of the nonlinear scattering wavevector can be actively tuned by external optical parameters without having to alter the geometry, composition or shape of the material. We emphasize that

such spatial tunability is mainly due to the fact that self-assembled organic mesowires facilitate inclined crystallographic facets that can be harnessed to control directionality of nonlinear optical antennas.

A.3.7 A prospect for spatial engineering of nonlinear emission: SHG and TPEF from DAAQ mesowire

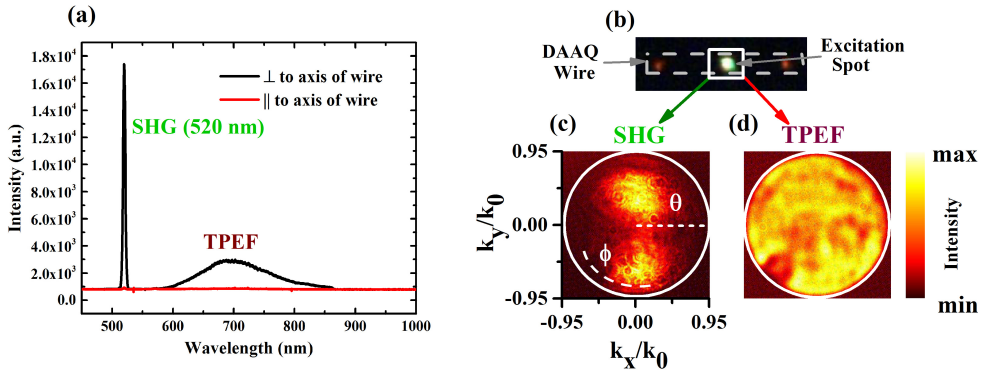

FIGURE A.7: (a) SHG and TPEF spectra from a DAAQ mesowire for pump polarizations parallel and perpendicular to the long axis of the wire. (b) Nonlinear optical image of a DAAQ mesowire excited at the center. Note there is faint TPEF emission from distal ends of the mesowire, which indicates waveguiding property of the mesowire. Fourier-plane images of the (c) SHG and (d) TPEF emission from the center of the wire indicates directional and isotropic distribution of light, respectively. These images were collected by spatial and spectral filtering techniques.

There are two aspects of organic molecular wires which we wish to emphasize. First is that they facilitate not only SHG but also two-photon-excited fluorescence (TPEF) [186]. Second is that certain organic mesowires can function as an optical waveguide of fluorescent signal [188, 199]. With this hindsight, we are interested to compare the directionality of SHG and TPEF from the same excitation on DAAQ mesowire, and observe waveguiding effect, if any. Figure A.7 (a) shows the optical spectra of the TPEF and SHG collected from the center of a DAAQ mesowire (Figure A.7 (b)) with excitation parallel and perpendicular to the mesowire. We observed that the SHG emission is typically more intense compared to TPEF for both the cases. Both emission processes reach their maximum intensity when pump polarization is oriented perpendicular to long axis of the mesowire. This again confirms the orientation of nonlinear dipole to be perpendicular to the long axis of the wire. Next, we probed the directionality of the TPEF compared to SHG signal. To this end, we captured angle-resolved

nonlinear scattering by selective spectral and spatial filtering from the region of interest and imaging it on the Fourier-plane of the collection objective lens (see method section for details). In Figure A.7 (c) and (d) we compare the angle resolved SHG and TPEF, respectively. It is clear that SHG scattering is directional compared to isotropic emission due to TPEF. This directional emission of SHG is because of the fact that SHG is a coherent emission [186] process with a specific phase defined between the nonlinear dipolar emitters, whereas TPEF is an incoherent process. Another observation is that the TPEF signal propagates along the length of the mesowire and outcouples from ends of the wire, whereas the SHG is confined mainly to the location of excitation (see the center and distal ends of the mesowire in Figure A.7 (b)). This observation of localizing the coherent signal and delocalizing the incoherent nonlinear optical emission for a common pump-excitation can be harnessed in signal processing, where the coherent source is to be out-coupled in a specific direction and incoherent signal is to be guided along the circuit.

A.4 Conclusion

In summary, controlling the directionality of nonlinear optical signal from sub-wavelength structures have direct ramification on design and development of active optical antennas and nonlinear optical circuits. Our study shows, how the crystallographic facets of an organic mesowire can be utilized to control the second harmonic generation emission pattern at sub-wavelength scales. We have demonstrated this principle on a two-facet and three-facet mesowire crystals, and have emphasized the role of selective excitation of spatially distributed dipoles as an important criterion for our observations. Numerical simulations of the prototypical geometry show spatial dependence of the near-field excitation, which further corroborate the assumptions that nonlinear dipoles distributed on the facets of the extended mesowire play a vital role in controlling the SHG directionality. Given that organic molecular mesowires can be prepared and deposited on various substrates, our observation can be adapted to various platforms including flexible plasmonic metasurfaces. An attractive aspect of organic mesostrutures is that they can be easily integrated on various optoelectronic circuits, which means the proposed optical antennas can be potentially operated under electric bias. Such biasing mechanisms can be utilized not only as active optical antennas, but also as coherent light emitting devices facilitated by Frenkel exciton-polaritons[188] in such organic nanostructures. Furthermore, our results show how SHG and TPEF can be spatially and angularly discriminated on the mesowire by utilizing the waveguiding capability of the

quasi-one dimensional structure. Such spatial and angular discrimination of two different nonlinear optical emission processes by the same excitation can provide interesting opportunities in nonlinear optical circuitry. An interesting prospect of our work is to couple organic mesowires to optical microcavities, where mode coupling between the wire and the cavity can lead to nonlinear optical interaction which can be reversibly switched from weak to strong coupling regimes.

Bibliography

[1]K. Y. Bliokh, F. J. Rodríguez-Fortuño, F. Nori, and A. V. Zayats, "Spin–orbit interactions of light", Nature Photonics **9**, 796 (2015).

[2]J. H. Poynting, "The wave motion of a revolving shaft, and a suggestion as to the angular momentum in a beam of circularly polarised light", Proceedings of the Royal Society of London. Series A, Containing Papers of a Mathematical and Physical Character **82**, 560–567 (1909).

[3]R. A. Beth, "Mechanical detection and measurement of the angular momentum of light", Physical Review **50**, 115 (1936).

[4]L. Allen, M. W. Beijersbergen, R. Spreeuw, and J. Woerdman, "Orbital angular momentum of light and the transformation of laguerre-gaussian laser modes", Physical Review A **45**, 8185 (1992).

[5]A. M. Yao and M. J. Padgett, "Orbital angular momentum: origins, behavior and applications", Advances in Optics and Photonics **3**, 161–204 (2011).

[6]A. Bekshaev, K. Y. Bliokh, and M. Soskin, "Internal flows and energy circulation in light beams", Journal of Optics **13**, 053001 (2011).

[7]H. Rubinsztein-Dunlop, A. Forbes, M. V. Berry, M. R. Dennis, D. L. Andrews, M. Mansuripur, C. Denz, C. Alpmann, P. Banzer, T. Bauer, et al., "Roadmap on structured light", Journal of Optics **19**, 013001 (2016).

[8]D. L. Andrews and M. Babiker, *The angular momentum of light* (Cambridge University Press, 2012).

[9]L Allen, M. Padgett, and M Babiker, "Iv the orbital angular momentum of light", in *Progress in optics*, Vol. 39 (Elsevier, 1999), pp. 291–372.

[10]Y. Shen, X. Wang, Z. Xie, C. Min, X. Fu, Q. Liu, M. Gong, and X. Yuan, "Optical vortices 30 years on: oam manipulation from topological charge to multiple singularities", Light: Science & Applications **8**, 1–29 (2019).

[11]A. Bekshaev, K. Y. Bliokh, and M. Soskin, "Internal flows and energy circulation in light beams", Journal of Optics **13**, 053001 (2011).

[12]A. Y. Bekshaev and M. Soskin, "Transverse energy flows in vectorial fields of paraxial beams with singularities", Optics communications **271**, 332–348 (2007).

[13]M. V. Berry, "Optical currents", Journal of Optics A: Pure and Applied Optics **11**, 094001 (2009).

[14]O. Angelsky, A. Y. Bekshaev, P. Maksimyak, A. Maksimyak, I. Mokhun, S. G. Hanson, C. Y. Zenkova, and A. Tyurin, "Circular motion of particles suspended in a gaussian beam with circular polarization validates the spin part of the internal energy flow", Optics Express **20**, 11351–11356 (2012).

[15]L Allen and M. Padgett, "The poynting vector in laguerre–gaussian beams and the interpretation of their angular momentum density", Optics Communications **184**, 67–71 (2000).

[16]Z. Yan and N. F. Scherer, "Optical vortex induced rotation of silver nanowires", The Journal of Physical Chemistry Letters **4**, 2937–2942 (2013).

[17]D. P. Ghai, P Senthilkumaran, and R. Sirohi, "Single-slit diffraction of an optical beam with phase singularity", Optics and Lasers in Engineering **47**, 123–126 (2009).

[18]J. Hirsch, "Spin hall effect", Physical Review Letters **83**, 1834 (1999).

[19]M. Onoda, S. Murakami, and N. Nagaosa, "Hall effect of light", Physical review letters **93**, 083901 (2004).

[20]K. Y. Bliokh, A. Niv, V. Kleiner, and E. Hasman, "Geometrodynamics of spinning light", Nature Photonics **2**, 748 (2008).

[21]O. Hosten and P. Kwiat, "Observation of the spin hall effect of light via weak measurements", Science **319**, 787–790 (2008).

[22]K. Y. Bliokh and Y. P. Bliokh, "Conservation of angular momentum, transverse shift, and spin hall effect in reflection and refraction of an electromagnetic wave packet", Physical review letters **96**, 073903 (2006).

[23]K. Y. Bliokh and Y. P. Bliokh, "Polarization, transverse shifts, and angular momentum conservation laws in partial reflection and refraction of an electromagnetic wave packet", Physical Review E **75**, 066609 (2007).

[24]J. Korger, A. Aiello, V. Chille, P. Banzer, C. Wittmann, N. Lindlein, C. Marquardt, and G. Leuchs, "Observation of the geometric spin hall effect of light", Physical review letters **112**, 113902 (2014).

[25]Y. Gorodetski, K. Bliokh, B Stein, C Genet, N Shitrit, V. Kleiner, E. Hasman, and T. Ebbesen, "Weak measurements of light chirality with a plasmonic slit", Physical review letters **109**, 013901 (2012).

[26]N. Shitrit, I. Bretner, Y. Gorodetski, V. Kleiner, and E. Hasman, "Optical spin hall effects in plasmonic chains", Nano letters **11**, 2038–2042 (2011).

[27]J. Lin, J. B. Mueller, Q. Wang, G. Yuan, N. Antoniou, X.-C. Yuan, and F. Capasso, "Polarization-controlled tunable directional coupling of surface plasmon polaritons", Science **340**, 331–334 (2013).

[28]N. Shitrit, I. Yulevich, E. Maguid, D. Ozeri, D. Veksler, V. Kleiner, and E. Hasman, "Spin-optical metamaterial route to spin-controlled photonics", Science **340**, 724–726 (2013).

[29]X. Ling, X. Zhou, K. Huang, Y. Liu, C.-W. Qiu, H. Luo, and S. Wen, "Recent advances in the spin hall effect of light", Reports on Progress in Physics **80**, 066401 (2017).

[30]X. Zhou, X. Ling, H. Luo, and S. Wen, "Identifying graphene layers via spin hall effect of light", Applied Physics Letters **101**, 251602 (2012).

[31]Y Gorodetski, A Niv, V Kleiner, and E Hasman, "Observation of the spin-based plasmonic effect in nanoscale structures", Physical review letters **101**, 043903 (2008).

[32]M. Neugebauer, S. Nechayev, M. Vorndran, G. Leuchs, and P. Banzer, "Weak measurement enhanced spin hall effect of light for particle displacement sensing", Nano letters **19**, 422–425 (2018).

[33]M. V. Berry, "Quantal phase factors accompanying adiabatic changes", Proceedings of the Royal Society of London. A. Mathematical and Physical Sciences **392**, 45–57 (1984).

[34]M Padgett, J Arlt, N Simpson, and L Allen, "An experiment to observe the intensity and phase structure of laguerre–gaussian laser modes", American Journal of Physics **64**, 77–82 (1996).

[35]D. Wei, Y. Wang, D. Liu, Y. Zhu, W. Zhong, X. Fang, Y. Zhang, and M. Xiao, "Simple and nondestructive on-chip detection of optical orbital angular momentum through a single plasmonic nanohole", ACS Photonics **4**, 996–1002 (2017).

[36]P. Genevet, J. Lin, M. A. Kats, and F. Capasso, "Holographic detection of the orbital angular momentum of light with plasmonic photodiodes", Nature communications **3**, 1278 (2012).

[37]S. Mei, K. Huang, H. Liu, F. Qin, M. Q. Mehmood, Z. Xu, M. Hong, D. Zhang, J. Teng, A. Danner, et al., "On-chip discrimination of orbital angular momentum of light with plasmonic nanoslits", Nanoscale **8**, 2227–2233 (2016).

[38]J. Chen, X. Chen, T. Li, and S. Zhu, "On-chip detection of orbital angular momentum beam by plasmonic nanogratings", Laser & Photonics Reviews, 1700331.

[39]W. L. Barnes, A. Dereux, and T. W. Ebbesen, "Surface plasmon subwavelength optics", nature **424**, 824 (2003).

[40]J. Sambles, G. Bradbery, and F. Yang, "Optical excitation of surface plasmons: an introduction", Contemporary physics **32**, 173–183 (1991).

[41]L. Novotny and B. Hecht, *Principles of nano-optics* (Cambridge university press, 2012).

[42]M Harris, C. Hill, and J. Vaughan, "Optical helices and spiral interference fringes", Optics communications **106**, 161–166 (1994).

[43]C. Tamm and C. Weiss, "Bistability and optical switching of spatial patterns in a laser", JOSA B **7**, 1034–1038 (1990).

[44]M. Beijersbergen, R. Coerwinkel, M Kristensen, and J. Woerdman, "Helical-wavefront laser beams produced with a spiral phaseplate", Optics communications **112**, 321–327 (1994).

[45]N. Heckenberg, R McDuff, C. Smith, H Rubinsztein-Dunlop, and M. Wegener, "Laser beams with phase singularities", Optical and Quantum Electronics **24**, S951–S962 (1992).

[46]N. Heckenberg, R McDuff, C. Smith, and A. White, "Generation of optical phase singularities by computer-generated holograms", Optics letters **17**, 221–223 (1992).

[47]J Arlt, K Dholakia, L Allen, and M. Padgett, "The production of multiringed laguerre–gaussian modes by computer-generated holograms", Journal of modern optics **45**, 1231–1237 (1998).

[48]V. Y. Bazhenov, M. Vasnetsov, and M. Soskin, "Laser beams with screw dislocations in their wavefronts", Jetp Lett **52**, 429–431 (1990).

[49]B. E. Saleh and M. C. Teich, *Fundamentals of photonics* (John Wiley & Sons, 2019).

[50]S. Shatalin, R Juškaitis, J. Tan, and T Wilson, "Reflection conoscopy and micro-ellipsometry of isotropic thin film structures", Journal of Microscopy **179**, 241–252 (1995).

[51]F. E. Wright, "Transmission of light through transparent inactive crystal plates, with special reference to observations in convergent polarized light", American Journal of Science, 157–211 (1911).

[52]A. B. Vasista, D. K. Sharma, and G. P. Kumar, "Fourier plane optical microscopy and spectroscopy", digital Encyclopedia of Applied Physics, 1–14 (2018).

[53]A. Agreda, D. K. Sharma, S. Viarbitskaya, R. Hernandez, B. Cluzel, O. Demichel, J.-C. Weeber, G. Colas Des Francs, G. P. Kumar, and A. Bouhelier, "Spatial distribution of the nonlinear photoluminescence in au nanowires", ACS Photonics (2019).

[54]A. B. Vasista, H. Jog, T. Heilpern, M. E. Sykes, S. Tiwari, D. K. Sharma, S. K. Chaubey, G. P. Wiederrecht, S. K. Gray, and G. P. Kumar, "Differential wavevector distribution of surface-enhanced raman scattering and fluorescence in a film-coupled plasmonic nanowire cavity", Nano letters **18**, 650–655 (2017).

[55]Y. Zhao, J. S. Edgar, G. D. Jeffries, D. McGloin, and D. T. Chiu, "Spin-to-orbital angular momentum conversion in a strongly focused optical beam", Physical Review Letters **99**, 073901 (2007).

[56]E. Hasman, G. Biener, A. Niv, and V. Kleiner, "Space-variant polarization manipulation", Progess in Optics **47**, 215–289 (2005).

[57]L. Marrucci, C Manzo, and D Paparo, "Optical spin-to-orbital angular momentum conversion in inhomogeneous anisotropic media", Physical review letters **96**, 163905 (2006).

[58]A. Dooghin, N. Kundikova, V. Liberman, and B. Y. Zel'dovich, "Optical magnus effect", Physical Review A **45**, 8204 (1992).

[59]V. Fedoseyev, "Transformation of the orbital angular momentum at the reflection and transmission of a light beam on a plane interface", Journal of Physics A: Mathematical and Theoretical **41**, 505202 (2008).

[60]K. Y. Bliokh and A. Aiello, "Goos–hänchen and imbert–fedorov beam shifts: an overview", Journal of Optics **15**, 014001 (2013).

[61]K. Y. Bliokh, A. Niv, V. Kleiner, and E. Hasman, "Geometrodynamics of spinning light", Nature Photonics **2**, 748 (2008).

[62]V. Liberman and B. Y. Zel'dovich, "Spin-orbit interaction of a photon in an inhomogeneous medium", Physical Review A **46**, 5199 (1992).

[63]C. Samlan, D. N. Naik, and N. K. Viswanathan, "Isogyres–manifestation of spin-orbit interaction in uniaxial crystal: a closed-fringe fourier analysis of conoscopic interference", Scientific reports **6**, 33141 (2016).

[64]Y. Liu, Y. Ke, H. Luo, and S. Wen, "Photonic spin hall effect in metasurfaces: a brief review", Nanophotonics **6**, 51 (2017).

[65]O. G. Rodríguez-Herrera, D. Lara, K. Y. Bliokh, E. A. Ostrovskaya, and C. Dainty, "Optical nanoprobing via spin-orbit interaction of light", Physical review letters **104**, 253601 (2010).

[66]V. Garbin, G. Volpe, E. Ferrari, M. Versluis, D. Cojoc, and D. Petrov, "Mie scattering distinguishes the topological charge of an optical vortex: a homage to gustav mie", New Journal of Physics **11**, 013046 (2009).

[67]E. Maguid, M. Yannai, A. Faerman, I. Yulevich, V. Kleiner, and E. Hasman, "Disorder-induced optical transition from spin hall to random rashba effect", Science **358**, 1411–1415 (2017).

[68]F. Cardano and L. Marrucci, "Spin–orbit photonics", Nature Photonics **9**, 776 (2015).

[69]C. Schwartz and A. Dogariu, "Conservation of angular momentum of light in single scattering", Optics express **14**, 8425–8433 (2006).

[70]O. G. Rodríguez-Herrera, D. Lara, and C. Dainty, "Far-field polarization-based sensitivity to sub-resolution displacements of a sub-resolution scatterer in tightly focused fields", Optics express **18**, 5609–5628 (2010).

[71]K. Y. Bliokh, E. A. Ostrovskaya, M. A. Alonso, O. G. Rodríguez-Herrera, D. Lara, and C. Dainty, "Spin-to-orbital angular momentum conversion in focusing, scattering, and imaging systems", Optics express **19**, 26132–26149 (2011).

[72]Y. Gorodetski, K. Bliokh, B Stein, C Genet, N Shitrit, V. Kleiner, E. Hasman, and T. Ebbesen, "Weak measurements of light chirality with a plasmonic slit", Physical review letters **109**, 013901 (2012).

[73]A. Y. Bekshaev, "Spin–orbit interaction of light and diffraction of polarized beams", Journal of Optics **19**, 085602 (2017).

[74]X. Ling, X. Zhou, X. Yi, W. Shu, Y. Liu, S. Chen, H. Luo, S. Wen, and D. Fan, "Giant photonic spin hall effect in momentum space in a structured metamaterial with spatially varying birefringence", Light: Science & Applications **4**, e290 (2015).

[75]Z. Qin, Q. Liu, C. Liu, C. Yue, and Y. Lang, "Enhanced in-plane and out-of-plane photonic spin hall effect via surface plasmon resonance", Physics of Plasmas **25**, 022121 (2018).

[76]G. S. Agarwal and S.-A. Biehs, "Highly nonparaxial spin hall effect and its enhancement by plasmonic structures", Optics letters **38**, 4421–4424 (2013).

[77]S.-A. Biehs and G. S. Agarwal, "Large enhancement of förster resonance energy transfer on graphene platforms", Applied Physics Letters **103**, 243112 (2013).

[78]Y. Sun, Y. Yin, B. T. Mayers, T. Herricks, and Y. Xia, "Uniform silver nanowires synthesis by reducing agno3 with ethylene glycol in the presence of seeds and poly (vinyl pyrrolidone)", Chemistry of Materials **14**, 4736–4745 (2002).

[79]R. Chikkaraddy, D. Singh, and G. Pavan Kumar, "Plasmon assisted light propagation and raman scattering hot-spot in end-to-end coupled silver nanowire pairs", Applied Physics Letters **100**, 043108 (2012).

[80]A. Forbes, A. Dudley, and M. McLaren, "Creation and detection of optical modes with spatial light modulators", Advances in Optics and Photonics **8**, 200–227 (2016).

[81]J. Yang, J.-P. Hugonin, and P. Lalanne, "Near-to-far field transformations for radiative and guided waves", ACS photonics **3**, 395–402 (2016).

[82]P. B. Johnson and R.-W. Christy, "Optical constants of the noble metals", Physical review B **6**, 4370 (1972).

[83]A. Y. Bekshaev and M. Soskin, "Transverse energy flows in vectorial fields of paraxial beams with singularities", Optics communications **271**, 332–348 (2007).

[84]M. V. Berry, "Optical currents", Journal of Optics A: Pure and Applied Optics **11**, 094001 (2009).

[85]L. Novotny and B. Hecht, *Principles of nano-optics* (Cambridge university press, 2012).

[86]V. D. Miljković, T. Shegai, P. Johansson, and M. Käll, "Simulating light scattering from supported plasmonic nanowires", Optics express **20**, 10816–10826 (2012).

[87]F. J. Rodríguez-Fortuño, G. Marino, P. Ginzburg, D. O'Connor, A. Martínez, G. A. Wurtz, and A. V. Zayats, "Near-field interference for the unidirectional excitation of electromagnetic guided modes", Science **340**, 328–330 (2013).

[88]J. Petersen, J. Volz, and A. Rauschenbeutel, "Chiral nanophotonic waveguide interface based on spin-orbit interaction of light", Science **346**, 67–71 (2014).

[89]D. O'connor, P. Ginzburg, F. J. Rodríguez-Fortuño, G. A. Wurtz, and A. V. Zayats, "Spin–orbit coupling in surface plasmon scattering by nanostructures", Nature communications **5**, 5327 (2014).

[90]X. Ling, X. Zhou, K. Huang, Y. Liu, C.-W. Qiu, H. Luo, and S. Wen, "Recent advances in the spin hall effect of light", Reports on Progress in Physics **80**, 066401 (2017).

[91]P. Lodahl, S. Mahmoodian, S. Stobbe, A. Rauschenbeutel, P. Schneeweiss, J. Volz, H. Pichler, and P. Zoller, "Chiral quantum optics", Nature **541**, 473 (2017).

[92]S.-H. Gong, F. Alpeggiani, B. Sciacca, E. C. Garnett, and L Kuipers, "Nanoscale chiral valley-photon interface through optical spin-orbit coupling", Science **359**, 443–447 (2018).

[93]L. Allen, M. W. Beijersbergen, R. Spreeuw, and J. Woerdman, "Orbital angular momentum of light and the transformation of laguerre-gaussian laser modes", Physical Review A **45**, 8185 (1992).

[94]J. Wang, J.-Y. Yang, I. M. Fazal, N. Ahmed, Y. Yan, H. Huang, Y. Ren, Y. Yue, S. Dolinar, M. Tur, et al., "Terabit free-space data transmission employing orbital angular momentum multiplexing", Nature photonics **6**, 488 (2012).

[95]M. Krenn, J. Handsteiner, M. Fink, R. Fickler, R. Ursin, M. Malik, and A. Zeilinger, "Twisted light transmission over 143 km", Proceedings of the National Academy of Sciences **113**, 13648–13653 (2016).

[96]N. Bozinovic, Y. Yue, Y. Ren, M. Tur, P. Kristensen, H. Huang, A. E. Willner, and S. Ramachandran, "Terabit-scale orbital angular momentum mode division multiplexing in fibers", science **340**, 1545–1548 (2013).

[97]G. Foo, D. M. Palacios, and G. A. Swartzlander, "Optical vortex coronagraph", Optics letters **30**, 3308–3310 (2005).

[98]E Serabyn, D Mawet, and R Burruss, "An image of an exoplanet separated by two diffraction beamwidths from a star", Nature **464**, 1018 (2010).

[99]N. Cvijetic, G. Milione, E. Ip, and T. Wang, "Detecting lateral motion using light's orbital angular momentum", Scientific reports **5**, 15422 (2015).

[100]A Nicolas, L Veissier, L Giner, E Giacobino, D Maxein, and J Laurat, "A quantum memory for orbital angular momentum photonic qubits", Nature Photonics **8**, 234 (2014).

[101]L Paterson, M. MacDonald, J. Arlt, W. Sibbett, P. Bryant, and K. Dholakia, "Controlled rotation of optically trapped microscopic particles", Science **292**, 912–914 (2001).

[102]J. E. Curtis and D. G. Grier, "Structure of optical vortices", Physical review letters **90**, 133901 (2003).

[103]Y. Wang, D. Wei, Y. Zhu, X. Huang, X. Fang, W. Zhong, Q. Wang, Y. Zhang, and M. Xiao, "Conversion of the optical orbital angular momentum in a plasmon-assisted second-harmonic generation", Applied Physics Letters **109**, 081105 (2016).

[104]G. Bautista and M. Kauranen, "Vector-field nonlinear microscopy of nanostructures", ACS Photonics **3**, 1351–1370 (2016).

[105]D.-S. Ding, Z.-Y. Zhou, B.-S. Shi, X.-B. Zou, and G.-C. Guo, "Linear up-conversion of orbital angular momentum", Optics letters **37**, 3270–3272 (2012).

[106]M Padgett, J Arlt, N Simpson, and L Allen, "An experiment to observe the intensity and phase structure of laguerre–gaussian laser modes", American Journal of Physics **64**, 77–82 (1996).

[107]J. Leach, M. J. Padgett, S. M. Barnett, S. Franke-Arnold, and J. Courtial, "Measuring the orbital angular momentum of a single photon", Physical review letters **88**, 257901 (2002).

[108]G. C. Berkhout, M. P. Lavery, J. Courtial, M. W. Beijersbergen, and M. J. Padgett, "Efficient sorting of orbital angular momentum states of light", Physical review letters **105**, 153601 (2010).

[109]S. Lightman, G. Hurvitz, R. Gvishi, and A. Arie, "Miniature wide-spectrum mode sorter for vortex beams produced by 3d laser printing", Optica **4**, 605–610 (2017).

[110]G. Ruffato, M. Massari, and F. Romanato, "Compact sorting of optical vortices by means of diffractive transformation optics", Optics letters **42**, 551–554 (2017).

[111]D. Wei, Y. Wang, D. Liu, Y. Zhu, W. Zhong, X. Fang, Y. Zhang, and M. Xiao, "Simple and nondestructive on-chip detection of optical orbital angular momentum through a single plasmonic nanohole", ACS Photonics **4**, 996–1002 (2017).

[112]R. M. Kerber, J. M. Fitzgerald, D. E. Reiter, S. S. Oh, and O. Hess, "Reading the orbital angular momentum of light using plasmonic nanoantennas", ACS Photonics **4**, 891–896 (2017).

[113]T. Shegai, V. D. Miljkovic, K. Bao, H. Xu, P. Nordlander, P. Johansson, and M. Kall, "Unidirectional broadband light emission from supported plasmonic nanowires", Nano letters **11**, 706–711 (2011).

[114]S. Lal, J. H. Hafner, N. J. Halas, S. Link, and P. Nordlander, "Noble metal nanowires: from plasmon waveguides to passive and active devices", Accounts of Chemical Research **45**, 1887–1895 (2012).

[115]A. B. Vasista, H. Jog, T. Heilpern, M. E. Sykes, S. Tiwari, D. K. Sharma, S. K. Chaubey, G. P. Wiederrecht, S. K. Gray, and G. V. P. Kumar, "Differential wavevector distribution of surface-enhanced raman scattering and fluorescence in a film-coupled plasmonic nanowire cavity", Nano Letters **18**, 650–655 (2018).

[116]D. Zhang, Y. Xiang, J. Chen, J. Cheng, L. Zhu, R. Wang, G. Zou, P. Wang, H. Ming, M. Rosenfeld, R. Badugu, and J. R. Lakowicz, "Extending the propagation distance of a silver nanowire plasmonic waveguide with a dielectric multilayer substrate", Nano Letters **18**, 1152–1158 (2018).

[117]F. Gu, H. Zeng, L. Tong, and S. Zhuang, "Metal single-nanowire plasmonic sensors", Optics letters **38**, 1826–1828 (2013).

[118]Y. Li, M. Kang, J. Shi, K. Wu, S. Zhang, and H. Xu, "Transversely divergent second harmonic generation by surface plasmon polaritons on single metallic nanowires", Nano letters **17**, 7803–7808 (2017).

[119]S. Viarbitskaya, O. Demichel, B. Cluzel, G. C. des Francs, and A. Bouhelier, "Delocalization of nonlinear optical responses in plasmonic nanoantennas", Physical review letters **115**, 197401 (2015).

[120]D. K. Sharma, V. Kumar, A. B. Vasista, S. K. Chaubey, and G. P. Kumar, "Spin-hall effect in the scattering of structured light from plasmonic nanowire", Optics letters **43**, 2474–2477 (2018).

[121]Y. Sun, B. Mayers, T. Herricks, and Y. Xia, "Polyol synthesis of uniform silver nanowires: a plausible growth mechanism and the supporting evidence", Nano letters **3**, 955–960 (2003).

[122]A. Forbes, A. Dudley, and M. McLaren, "Creation and detection of optical modes with spatial light modulators", Advances in Optics and Photonics **8**, 200–227 (2016).

[123]A. Bekshaev, K. Y. Bliokh, and M. Soskin, "Internal flows and energy circulation in light beams", Journal of Optics **13**, 053001 (2011).

[124]P. B. Johnson and R.-W. Christy, "Optical constants of the noble metals", Physical review B **6**, 4370 (1972).

[125]J. Yang, J.-P. Hugonin, and P. Lalanne, "Near-to-far field transformations for radiative and guided waves", ACS photonics **3**, 395–402 (2016).

[126]F Ricci, W Löffler, and M. van Exter, "Instability of higher-order optical vortices analyzed with a multi-pinhole interferometer", Optics express **20**, 22961–22975 (2012).

[127]M. J. Padgett, F. M. Miatto, M. P. Lavery, A. Zeilinger, and R. W. Boyd, "Divergence of an orbital-angular-momentum-carrying beam upon propagation", New Journal of Physics **17**, 023011 (2015).

[128]J. Langer, D. Jimenez de Aberasturi, J. Aizpurua, R. A. Alvarez-Puebla, B. Auguié, J. J. Baumberg, G. C. Bazan, S. E. Bell, A. Boisen, A. G. Brolo, et al., "Present and future of surface-enhanced raman scattering", ACS nano (2019).

[129]G. Baffou and R. Quidant, "Thermo-plasmonics: using metallic nanostructures as nano-sources of heat", Laser & Photonics Reviews **7**, 171–187 (2013).

[130]X. Guo, Y. Ma, Y. Wang, and L. Tong, "Nanowire plasmonic waveguides, circuits and devices", Laser & Photonics Reviews **7**, 855–881 (2013).

[131]T. Shegai, V. D. Miljkovic, K. Bao, H. Xu, P. Nordlander, P. Johansson, and M. Kall, "Unidirectional broadband light emission from supported plasmonic nanowires", Nano letters **11**, 706–711 (2011).

[132]H. Wei, D. Pan, S. Zhang, Z. Li, Q. Li, N. Liu, W. Wang, and H. Xu, "Plasmon waveguiding in nanowires", Chemical reviews **118**, 2882–2926 (2018).

[133]E. Krauss, G. Razinskas, D. Köck, S. Grossmann, and B. Hecht, "Reversible mapping and sorting the spin of photons on the nanoscale: a spin-optical nano device", Nano letters (2019).

[134]A. Bag, M. Neugebauer, U. Mick, S. Christiansen, S. A. Schulz, and P. Banzer, "Towards fully integrated photonic displacement sensors", arXiv preprint arXiv:1909.04478 (2019).

[135]P. Li, X. Yan, F. Zhou, X. Tang, L. Yang, and J. Liu, "A capillary force-induced au nanoparticle–ag nanowire single hot spot platform for sers analysis", Journal of Materials Chemistry C **5**, 3229–3237 (2017).

[136]P Mühlschlegel, H.-J. Eisler, O. Martin, B Hecht, and D. Pohl, "Resonant optical antennas", Science **308**, 1607–1609 (2005).

[137]V. Giannini, A. I. Fernández-Domínguez, S. C. Heck, and S. A. Maier, "Plasmonic nanoantennas: fundamentals and their use in controlling the radiative properties of nanoemitters", Chemical Reviews **111**, 3888–3912 (2011).

[138]L. Novotny and N. Van Hulst, "Antennas for light", Nature photonics **5**, 83 (2011).

[139]J. A. Schuller, E. S. Barnard, W. Cai, Y. C. Jun, J. S. White, and M. L. Brongersma, "Plasmonics for extreme light concentration and manipulation", Nature materials **9**, 193 (2010).

[140]H. Harutyunyan, G. Volpe, and L Novotny, in *Optical antennas* (Cambridge Univ. Press, 2012) Chap. Nonlinear optical antennas.

[141]M. Kauranen and A. V. Zayats, "Nonlinear plasmonics", Nature photonics **6**, 737 (2012).

[142]J. Y. Suh and T. W. Odom, "Nonlinear properties of nanoscale antennas", Nano Today **8**, 469–479 (2013).

[143]J. Butet, P.-F. Brevet, and O. J. Martin, "Optical second harmonic generation in plasmonic nanostructures: from fundamental principles to advanced applications", ACS Nano **9**, 10545–10562 (2015).

[144]K. Thyagarajan, C. Santschi, P. Langlet, and O. J. Martin, "Highly improved fabrication of ag and al nanostructures for uv and nonlinear plasmonics", Advanced Optical Materials **4**, 871–876 (2016).

[145]Y. Ogata and C. Guo, "Nonlinear optics on nano/micro-hierarchical structures on metals: focus on symmetric and plasmonic effects", Nano Reviews & Experiments **8**, 1339545 (2017).

[146]Y. Ogata and G. Mizutani, "Absolute second order nonlinear susceptibility of pt nanowire arrays on mgo faceted substrates with various cross-sectional shapes", Applied Physics Letters **103**, 093107 (2013).

[147]Y. Ogata, "Optical second harmonic generation from nanostructure-covered microcubes on nickel", Opt. Mater. Express **6**, 1520–1529 (2016).

[148]A. Kuznetsov, A. Miroshnichenko, Y. Fu, J Zhang, and B Luk'yanchuk, "Magnetic light.", Scientific reports **2**, 492 (2012).

[149]A. I. Kuznetsov, A. E. Miroshnichenko, M. L. Brongersma, Y. S. Kivshar, and B. Luk'yanchuk, "Optically resonant dielectric nanostructures", Science **354**, aag2472 (2016).

[150]Y. Kivshar and A. Miroshnichenko, "Meta-optics with mie resonances", Optics and Photonics News **28**, 24–31 (2017).

[151]D. Smirnova and Y. S. Kivshar, "Multipolar nonlinear nanophotonics", Optica **3**, 1241–1255 (2016).

[152]M. Decker and I. Staude, "Resonant dielectric nanostructures: a low-loss platform for functional nanophotonics", Journal of Optics **18**, 103001 (2016).

[153]G. Grinblat, Y. Li, M. P. Nielsen, R. F. Oulton, and S. A. Maier, "Enhanced third harmonic generation in single germanium nanodisks excited at the anapole mode", Nano letters **16**, 4635–4640 (2016).

[154]Y. Yang, O. D. Miller, T. Christensen, J. D. Joannopoulos, and M. Soljacic, "Low-loss plasmonic dielectric nanoresonators", Nano Letters **17**, 3238–3245 (2017).

[155]S Mokkapati and C Jagadish, "Review on photonic properties of nanowires for photovoltaics [invited]", Optics Express **24**, 17345–17358 (2016).

[156]X. Zambrana-Puyalto and N. Bonod, "Tailoring the chirality of light emission with spherical si-based antennas", Nanoscale **8**, 10441–10452 (2016).

[157]R. Regmi, J. Berthelot, P. M. Winkler, M. Mivelle, J. Proust, F. Bedu, I. Ozerov, T. Begou, J. Lumeau, H. Rigneault, et al., "All-dielectric silicon nanogap antennas to enhance the fluorescence of single molecules", Nano letters **16**, 5143–5151 (2016).

[158]M.-L. Ren, R. Agarwal, W. Liu, and R. Agarwal, "Crystallographic characterization of ii–vi semiconducting nanostructures via optical second harmonic generation", Nano letters **15**, 7341–7346 (2015).

[159]S. S. Kruk, R. Camacho-Morales, L. Xu, M. Rahmani, D. A. Smirnova, L. Wang, H. H. Tan, C. Jagadish, D. N. Neshev, and Y. S. Kivshar, "Nonlinear optical magnetism revealed by second-harmonic generation in nanoantennas", Nano Letters **17**, 3914–3918 (2017).

[160]N. Bontempi, K. E. Chong, H. W. Orton, I. Staude, D.-Y. Choi, I. Alessandri, Y. S. Kivshar, and D. N. Neshev, "Highly sensitive biosensors based on all-dielectric nanoresonators", Nanoscale **9**, 4972–4980 (2017).

[161]S. S. Kruk, R. Camacho-Morales, L. Xu, M. Rahmani, D. A. Smirnova, L. Wang, H. H. Tan, C. Jagadish, D. N. Neshev, and Y. S. Kivshar, "Nonlinear optical magnetism revealed by second-harmonic generation in nanoantennas", Nano Letters **17**, 3914–3918 (2017).

[162]S. V. Makarov, M. I. Petrov, U. Zywietz, V. Milichko, D. Zuev, N. Lopanitsyna, A. Kuksin, I. Mukhin, G. Zograf, E. Ubyivovk, et al., "Efficient second-harmonic generation in nanocrystalline silicon nanoparticles", Nano Letters **17**, 3047–3053 (2017).

[163]J. I. Dadap, "Optical second-harmonic scattering from cylindrical particles", Phys. Rev. B **78**, 205322 (2008).

[164]R. M. Osgood, N. C. Panoiu, J. I. Dadap, X. Liu, X. Chen, I.-W. Hsieh, E. Dulkeith, W. M. Green, and Y. A. Vlasov, "Engineering nonlinearities in nanoscale optical systems: physics and applications in dispersion-engineered silicon nanophotonic wires", Adv. Opt. Photon. **1**, 162–235 (2009).

[165]J. I. Dadap, H. B. de Aguiar, and S. Roke, "Nonlinear light scattering from clusters and single particles", The Journal of Chemical Physics **130**, 214710 (2009).

[166]L. Wang, S. Kruk, L. Xu, M. Rahmani, D. Smirnova, A. Solntsev, I. Kravchenko, D. Neshev, and Y. Kivshar, "Shaping the third-harmonic radiation from silicon nanodimers", Nanoscale **9**, 2201–2206 (2017).

[167]Y. Yang, A. E. Miroshnichenko, S. V. Kostinski, M. Odit, P. Kapitanova, M. Qiu, and Y. S. Kivshar, "Multimode directionality in all-dielectric metasurfaces", Phys. Rev. B **95**, 165426 (2017).

[168]R. Camacho-Morales, M. Rahmani, S. Kruk, L. Wang, L. Xu, D. A. Smirnova, A. S. Solntsev, A. Miroshnichenko, H. H. Tan, F. Karouta, S. Naureen, K. Vora, L. Carletti, C. De Angelis, C. Jagadish, Y. S. Kivshar, and D. N. Neshev, "Nonlinear generation of vector beams from algaas nanoantennas", Nano Letters **16**, 7191–7197 (2016).

[169]L. Carletti, A. Locatelli, D. Neshev, and C. De Angelis, "Shaping the radiation pattern of second-harmonic generation from algaas dielectric nanoantennas", ACS Photonics **3**, 1500–1507 (2016).

[170]L. Ghirardini, L. Carletti, V. Gili, G. Pellegrini, L. Duò, M. Finazzi, D. Rocco, A. Locatelli, C. D. Angelis, I. Favero, M. Ravaro, G. Leo, A. Lemaître, and M. Celebrano, "Polarization properties of second-harmonic generation in algaas optical nanoantennas.", Optics letters **42**, 559 (2017).

[171]H. Aouani, M. Rahmani, M. Navarro-Cía, and S. A. Maier, "Third-harmonic-upconversion enhancement from a single semiconductor nanoparticle coupled to a plasmonic antenna", Nature nanotechnology **9**, 290 (2014).

[172]M. Hentschel, B. Metzger, B. Knabe, K. Buse, and H. Giessen, "Linear and nonlinear optical properties of hybrid metallic–dielectric plasmonic nanoantennas", Beilstein journal of nanotechnology **7**, 111–120 (2016).

[173]T Utikal, M Hentschel, and H Giessen, "Nonlinear photonics with metallic nanostructures on top of dielectrics and waveguides", Applied Physics B: Lasers and Optics **105**, 51–65 (2011).

[174]B. Metzger, M. Hentschel, and H. Giessen, "Probing the near-field of second-harmonic light around plasmonic nanoantennas", Nano Letters **17**, 1931–1937 (2017).

[175]H. Linnenbank, Y. Grynko, J. Förstner, and S. Linden, "Second harmonic generation spectroscopy on hybrid plasmonic/dielectric nanoantennas", Light: Science and Applications **5**, e16013 (2016).

[176]X. Y. Xiong, L. J. Jiang, E. Wei, Y. H. Lo, and W. C. Chew, "Compact nonlinear yagi-uda nanoantennas", Scientific reports **6**, 18872 (2016).

[177]M.-L. Ren, W. Liu, C. O. Aspetti, L. Sun, and R. Agarwal, "Enhanced second-harmonic generation from metal-integrated semiconductor nanowires via highly confined whispering gallery modes", Nature communications **5**, 5432 (2014).

[178]F. Wang, A. B. Martinson, and H. Harutyunyan, "Efficient nonlinear metasurface based on nonplanar plasmonic nanocavities", ACS Photonics **4**, 1188–1194 (2017).

[179]U. Zywietz, A. B. Evlyukhin, C. Reinhardt, and B. N. Chichkov, "Laser printing of silicon nanoparticles with resonant optical electric and magnetic responses", Nature communications **5**, 3402 (2014).

[180]J. Clark and G. Lanzani, "Organic photonics for communications", Nature photonics **4**, 438 (2010).

[181]Y. Yan and Y. S. Zhao, "Organic nanophotonics: from controllable assembly of functional molecules to low-dimensional materials with desired photonic properties", Chemical Society Reviews **43**, 4325–4340 (2014).

[182]Y. S. Zhao, *Organic nanophotonics: fundamentals and applications* (Springer, 2014).

[183]R. Chandrasekar, "Organic photonics: prospective nano/micro scale passive organic optical waveguides obtained from π-conjugated ligand molecules", Physical Chemistry Chemical Physics **16**, 7173–7183 (2014).

[184]D. Venkatakrishnarao and R. Chandrasekar, "Engineering the self-assembly of dcm dyes into whispering-gallery-mode μ-hemispheres and fabry–pèrot-type μ-rods for visible–nir (600–875 nm) range optical microcavities", Advanced Optical Materials **4**, 112–119 (2016).

[185]S. Brasselet, V. Le Floch, F. Treussart, J.-F. Roch, J. Zyss, E. Botzung-Appert, and A. Ibanez, "In situ diagnostics of the crystalline nature of single organic nanocrystals by nonlinear microscopy", Physical review letters **92**, 207401 (2004).

[186]S. Brasselet, "Polarization-resolved nonlinear microscopy: application to structural molecular and biological imaging", Advances in Optics and Photonics **3**, 205 (2011).

[187]D. Venkatakrishnarao, Y. S. L. V. Narayana, M. A. Mohaiddon, E. A. Mamonov, N. Mitetelo, I. A. Kolmychek, A. I. Maydykovskiy, V. B. Novikov, T. V. Murzina, and R. Chandrasekar, "Two-photon luminescence and second-harmonic generation in organic nonlinear surface comprised of self-assembled frustum shaped organic microlasers", Advanced Materials **29**, 1605260, 1605260–n/a (2017).

[188]R. P. Tripathi, A. Dasgupta, R. Chikkaraddy, P. P. Patra, A. B. Vasista, and G. V. P. Kumar, "Optics of an individual organic molecular mesowire waveguide: directional light emission and anomalous refractive index", Journal of Optics **18**, 065002 (2016).

[189]E. D. Palik, *Handbook of optical constants of solids*, Vol. 3 (Academic press, 1998).

[190]Y. S. Zhao, P. Zhan, J. Kim, C. Sun, and J. Huang, "Patterned growth of vertically aligned organic nanowire waveguide arrays", ACS nano **4**, 1630–1636 (2010).

[191]R. Chikkaraddy, A. Dasgupta, S Dutta Gupta, and G. Pavan Kumar, "Microsphere-coupled organic waveguides: preparation, remote excitation of whispering gallery modes and waveguiding property", Applied Physics Letters **103**, 031112 (2013).

[192]Y. S. Zhao, J. Wu, and J. Huang, "Vertical organic nanowire arrays: controlled synthesis and chemical sensors", Journal of the American Chemical Society **131**, 3158–3159 (2009).

[193]"Construction of an organic crystal structural model based on combined electron and powder x-ray diffraction data and the charge flipping algorithm", Ultramicroscopy **111**, 812 –816 (2011).

[194]L Moreaux, O Sandre, and J Mertz, "Mem ne imaging by second-harmonic generation microscopy", JOSA B **17**, 1685–1694 (2000).

[195]L. Moreaux, O. Sandre, M. Blanchard-Desce, and J. Mertz, "Membrane imaging by simultaneous second-harmonic generation and two-photon microscopy", Opt. Lett. **25**, 320–322 (2000).

[196]L. Moreaux, O. Sandre, S. Charpak, M. Blanchard-Desce, and J. Mertz, "Coherent scattering in multi-harmonic light microscopy", Biophysical Journal **80**, 1568–1574 (2001).

[197]J Mertz and L Moreaux, "Second-harmonic generation by focused excitation of inhomogeneously distributed scatterers", Optics Communications **196**, 325–330 (2001).

[198]E. Y. S. Yew and C. J. R. Sheppard, "Effects of axial field components on second harmonic generation microscopy", Opt. Express **14**, 1167–1174 (2006).

[199]K. Takazawa, J.-i. Inoue, K. Mitsuishi, and T. Takamasu, "Fraction of a millimeter propagation of exciton polaritons in photoexcited nanofibers of organic dye", Physical review letters **105**, 067401 (2010).